Quantitative Measurement Techniques for Wind Turbine Blade Aerodynamic Performance

by

Tyler Gallant

A thesis
presented to the University of Waterloo
in fulfillment of the
thesis requirement for the degree of
Master of Applied Science
in
Mechanical and Mechatronics Engineering

Waterloo, Ontario, Canada, 2017

I hereby declare that I am the sole author of this thesis. This is a true copy of the thesis, including any required final revisions, as accepted by my examiners.

I understand that my thesis may be made electronically available to the public.

Abstract

The installed capacity of wind turbines has been growing rapidly in recent years, creating an increased need for accurate measurements and models of wind turbine performance to further their development. There is a need in the literature for experimental data to validate theoretical models and guide turbine blade design. Two related projects were completed to develop measurement techniques and provide such data: the use of a five-hole probe and in-blade data acquisition system to measure the wind turbine blade angle of attack, and the use of tuft flow visualization and a digital image processing algorithm to quantitatively assess the flow direction and behaviour of a wind turbine blade.

Experiments were completed at the University of Waterloo Wind Generation Research Facility using a 3.3 m diameter test turbine. Wind speed, rotational speed, shaft torque and angular position were controlled or monitored throughout all experiments. A 3D printed test blade was equipped with a five-hole pressure probe and data acquisition system to measure the flow angles at various radial locations. For tuft flow visualization testing, a separate rotor consisting of three aerodynamic blades was installed, and tufts and a camera were mounted to the surface of one of the blades. Extensive software was developed for controlling instruments and collecting experimental data.

The angle of attack and span-wise flow angles were successfully measured as a function of the tip speed ratio, yaw-offset position, radial location and azimuthal position. Variations in the angle of attack with these variables were consistent with wind turbine aerodynamics theory, and results were in close agreement with results calculated using two separate models from the literature. Angle of attack values typically ranged from 7° to 25° throughout the tests, with fluctuations as high as 7° when the wind turbine was yawed. Uncertainty values in the measurements were typically found to be within ±0.2°, which shows great potential for the method.

Tuft flow visualization measurements were processed by logging the orientation of each individual tuft, calculating their average orientations and interpolating to develop a contour map of flow direction over the wind turbine blade as a function of tip speed ratio, yaw-position and azimuthal position. Throughout testing, the fraction of tufts indicating stall ranged from 25% to as high as 60% as the tip speed ratio was decreased. Contour maps showed that separation typically formed first on the trailing edge of the blade near the root, and expanded towards the leading edge and tip. This pattern is in agreement with trends found for similar blades in the literature.

Acknowledgements

I would like to express my utmost appreciation for the support of the following people in getting me to this point. I have a lot of people to thank, and I could not have completed this project without their help and guidance.

First of all, I thank my supervisor Professor David Johnson. His experience and expertise in both wind energy and research in general were significant resources for me, and this project would not have been possible without him. The opportunities that he provided me with are sincerely appreciated.

Secondly, massive thanks to my fellow graduate students and friends in the Wind Energy Group who never hesitated to help out when I asked or make me feel welcome. The following students helped support me throughout my two years: Ahmed Abdelrahman, Kobra Gharali, Faegheh Ghorbani Shohrat, Rifki Adi Nugroho, Farid Samara and Nicholas Tam. Special thanks to Andrea Moscardi and Nigel Swytink-Binnema, who both helped me in establishing the starting points of this thesis and my starting point in Waterloo.

The support of the technical staff at the University of Waterloo was indispensable in achieving the practical aspects of this project. Many thanks specifically to Andy Barber, Jason Benninger, Neil Griffett and Michael Stachowsky.

I also have to acknowledge the support of our co-op students, Ardalan Abolfazli and Michael Lenover, who both helped immensely in preparing my experiments and provided company during the duller testing hours.

Of course, I could not have made it this far without the essential support of my parents, both in getting me to UWaterloo and in completing this project. In Waterloo, my aunts, uncles and cousins were incredibly welcoming and helpful in getting me set up and involved in family activities.

Thanks to my friends from PEI and Waterloo, Klynton Crabbe, Emily Gallant, Denis Dorion, David Marczak, Dan Bujak, and the Waterloo Writers Group for making Waterloo feel like a home away from home and providing me with many laughs and fond memories over the past two years. I hope this is still the beginning.

Finally, incredible thanks to my fiancée, Emily Jewell, who supported me through it all and made every day brighter. I love you.

Dedication

This work is dedicated to my parents whose constant support made this possible.

Table of Contents

List of Tables

List of Figures

Nomenclature

A	Swept area [m^2].
a	Axial induction factor.
a_{a0}	Radially dependent azimuthally averaged induction factor for axial flow.
a'	Tangential flow induction factor.
A_{span}	Span area of airfoil [m^2].
b	Bias uncertainty.
b_1	Minimum radius of tuft ellipse.
b_2	Maximum radius of tuft ellipse.
C_D	Drag coefficient.
$K(\chi)$	Influence of skew angle on induced velocity.
C	Chord length [m].
C_L	Lift coefficient.
C_p	Power coefficient.
C_{p_p}	Pitch pressure coefficient.
$C_{p_{static}}$	Static pressure coefficient.
$C_{p_{total}}$	Total pressure coefficient.
C_{p_y}	Yaw pressure coefficient.
C_{thrust}	Thrust coefficient.
C_y	Lift and drag coefficients projected to axial direction.
e	Eccentricity of recognized tuft.
F_D	Drag Force [N].
F_L	Lift Force [N].
$F(\mu)$	Function determining radial distribution of induced velocity normal to rotor plane.
$F_{\Omega r}$	Tangential flow velocity (Burton model [2]) [m/s].

$f(r)$	Axial interference function.
F_{wind}	Upstream wind velocity (Burton model [2]) [m/s].
g	Strength of the generated vorticity parallel to the rotor disc.
$g(r)$	Span-wise interference function.
h_t	Hub height [m].
N	Mask number.
N_B	Number of blades.
n_{min}	Desired minimum number of tufts recognized in frame.
N_s	Number of tufts recognized as stalled in frame.
N_{samp}	Number of samples.
N_t	Number of tufts recognized in frame.
p	Precision uncertainty.
P_{1-5}	Pressures measured at holes 1 through 5 [Pa].
P_{atm}	Atmospheric pressure [Pa].
P_{cf}	Probe pressure due to centrifugal force [Pa].
P_{norm}	Normalized probe pressure [Pa].
P	Aerodynamic rotor power.
R	Rotor Radius [m].
r	Local radius [m].
Re	Reynolds number.
U_2	Flow speed immediately upstream of rotor [m/s].
U_3	Flow speed immediately downstream of rotor [m/s].
U_4	Flow speed far downstream of rotor [m/s].
U_∞	Upstream Wind Speed [m/s].
U_{rot}	Tangential velocity of blade [m/s].
u_{tot}	Total uncertainty.
u, v, w	Wind velocity in cartesian coordinates [m/s].
$V_{rel_{xy}}$	Relative velocity projected onto blade [m/s].
W	Resultant wind velocity [m/s].

z	Elevation [m].

α	Angle of attack [°].
$\alpha_{critical}$	Critical angle of attack [°].
α_{geom}	Geometric angle of attack [°].
α_i	Induced angle of attack [°].
α_p	Local angle of attack with respect to probe [°].
β	Blade pitch [°].
β_f	Flow pitch angle relative to probe [°].
β_p	Spanwise flow angle with respect to probe [°].
χ	Skew angle [°].
δ	Sine of the yaw angle.
μ_{dyn}	Dynamic Viscosity [kg/m s].
ϵ	Probe span-wise offset angle [°].
ϵ_r	Proportion of axial stress to total stress.
T	Blade circulation.
γ	Yaw-offset angle [°].
γ_f	Flow yaw angle relative to probe [°].
λ	Tip speed ratio.
λ_r	Local tip speed ratio.
μ	Ratio of local radius to rotor radius (r/R).
Ω	Rotational speed of rotor [rad/s].
ω	Angular velocity of downstream wake [rad/s].
ϕ	Flow angle [°].
ϕ_t	Vortex helix angle [°].
ψ	Azimuthal position [°].
ρ	Density [kg/m^3].
σ	Standard deviation.
θ	Local flow probe angle offset [°].
ζ	Stall fraction.

$2D$	Two Dimensional.
$3D$	Three Dimensional.
ADC	Analog to Digital Converter.

BEM	Blade Element Momentum.
CFD	Computational Fluid Dynamics.
DAQ	Data Acquisition.
I/O	Input/Output.
LE	Leading Edge.
LFA	Local Flow Angle.
NaN	Not a Number.
NI	National Instruments.
$NREL$	National Renewable Energy Laboratory.
PTB	Pressure Transducer Board.
rpm	Revolutions per minute.
SFA	Span-wise Flow Angle.
TE	Trailing Edge.
UAE	Unsteady Aerodynamics Experiment.
UW	University of Waterloo.
VFD	Variable Frequency Drive.
VI	Virtual instrument.
WEG	Wind Energy Group.
WT	Wind Turbine.

Chapter 1

Introduction

1.1 Brief Review of Wind Energy

The use of wind turbines as a source of electricity from renewable resources has been growing rapidly in recent years. As of December 2015, Canada has reached a total installed capacity of over 11,000 MW of wind energy, more than 16 times the installed capacity of 2005 [1]. More impressively, this growth has occurred at an average rate of 23% per year from 2011 to 2015 [1]. As the impacts of fossil fuels and greenhouse gases on climate change become more apparent, this growth in the wind energy industry becomes only more likely to continue.

The generation of electricity using energy from the wind is a relatively new concept, but wind energy has been used to produce mechanical work for at least 3000 years [2]. Wind has been used to propel ships through the use of sails, as well as to generate torque and rotation for grinding grain and pumping water. However, the first true wind turbine to generate electricity was a 12 kW turbine developed by Charles Brush in cooperation with Poul la Cour in Denmark in the late 1800s [2].

Developments in wind turbine design continued slowly from this point, primarily due to low fossil fuel prices and the intermittency of the wind. However, rising concerns about energy costs in the 1970s and climate change has lead to a boom in the wind energy industry. As the installed capacity grew, the size of wind turbines has increased as well. Wood [3] categorizes wind turbines below 50 kW in capacity as being small-scale, and any turbine above 500 kW in capacity as being large-scale. Wind turbines between the small- and large-scale definitions are considered medium-scale, and micro-scale wind turbines are those with a capacity of 1 kW or less [3]. At the time of writing, the largest installed wind turbine is the MHI Vestas V164 turbine, which has a diameter of 164 m and a rated capacity of over 8 MW [4].

The majority of installed wind turbines, including the Vestas V164 turbine, spin about a horizontal axis. This is in contrast to Vertical Axis Wind Turbines (VAWTs), which rotate about a vertical axis. While VAWTs have several advantages, including reduced noise and a more accessible generator, they are widely accepted to have less potential than the horizontal design. Similarly, the majority of Horizontal Axis Wind Turbines (HAWTs) have an "upwind" design, which is to say that the upstream wind passes through the rotor before passing the tower. The upwind design has become the standard over "downwind" wind turbines given the negative impact of the tower on the blade aerodynamics that occurs when the wind passes the tower first. In this thesis, the theory and experiments presented will be focused on the standard upwind, horizontal axis wind turbine design.

1.2 Project Motivation

As the installed capacity of wind turbines has grown, so too has the field of research dedicated to measuring and improving wind turbine performance. Countless studies have been published in the literature, presenting experimental results or models developed to better understand the flow aerodynamics over rotating wind turbine blades. However, some areas in the literature are lacking, either due to a lack of experimental data for model validation or due to limited tools for data analysis. As will be seen in the literature review presented in Chapter 2, these areas include the measurement of the flow angle at the leading edge of a rotating wind turbine blade, as well as the development of stall over the blade. The objective of this thesis is to develop and test quantitative measurement techniques to address these two interrelated research areas.

The first focus is the measurement of the flow angle at the leading edge of a rotating wind turbine blade. Generally in wind energy research and development, this flow angle is estimated using wind velocity measurements made upstream of the turbine and simple geometry based models. Several more in-depth models for calculating the flow angle in various operational conditions have been presented in the literature. However, the lack of experimental measurements of the flow angle directly at the leading edge of the blade has resulted in a lack of model validation. As will be shown in Section 2.1.1, the flow angle has a significant impact on the performance of a wind turbine blade, and the lack of validation measurements presented is a serious problem in wind turbine development. In this thesis, the use of a five-hole pressure probe to measure the variation in angle of attack, span-wise flow angle, and the upstream wind velocity will be presented. Angle of attack measurements will also be compared to theoretical models in an effort to provide validation cases for future research and development.

The second focus area is dependent on the first. As the flow angle at the leading edge of a wind turbine blade increases, flow over the blade begins to separate and stall, which can greatly decrease the efficiency of the blade (see Section 2.1.1). Aerodynamic stall can also increase the noise output of wind turbines and decrease the fatigue life of turbine blades. However, wind turbine stall is a difficult phenomena to measure and analyze. One established technique reviewed in Section 2.3.2 is tuft flow visualization, in which small tufts of fabric are attached to the surface of the blade and their movement is recorded and used to assess the flow direction and behaviour over the blade surface. Until recent developments, tuft flow visualization results were analyzed manually, which limited the amount of data that could be practically analyzed, as well as increased the probability of human error. However, the development of image processing algorithms for post-processing tuft data has made this analysis faster and more reliable. In this thesis, the expansion of an existing image processing algorithm will be presented, as well as the analysis of average stall and stall distribution over the blade as a function of several parameters.

1.3 Project Overview

There fields in wind turbine aerodynamics research which are currently lacking in experimental measurements for validation or model development. While several studies (see Section 2.2.2) have presented measurements of the flow angle at the leading edge of a blade, the limitations of the data are such that developed models are being published without experimental validation. The first portion of this thesis therefore presents the use of a directional pressure probe to measure the flow angle at the leading edge of the blade as a function of several key variables, as well as the comparison of experimental results to previously un-validated models. The second portion of this thesis then presents a series of tuft flow visualization experiments, with results analyzed using a digital image processing algorithm which combines the strengths of the methods presented by Swytink-Binnema and Johnson [36] and Vey *et al.* [39].

In the next chapter, background theory and studies related to this project will be discussed in detail. First, two and three dimensional aerodynamics theory related to wind turbine functionality will be reviewed, including a discussion of flow angle models for turbines in yaw conditions. This is followed by a review of literature relevant to the flow angle measurements and tuft flow visualization experiments, including the digital image processing algorithms used for stall analysis.

Following the background, the experimental methods used in the flow angle and stall measurements are presented. This includes an overview of the test facility and wind turbine, the test configurations, and all instrumentation. A description of the modified digital image processing algorithm is also presented here, which explains changes made to the Swytink-Binnema and Johnson [36] algorithm to adopt advantages of the Vey *et al.* [39] method.

Finally, experimental results for the flow angle measurements are presented, as well as a comparison to theoretical models. This is followed by the measured tuft flow visualization results, including demonstrations of the capabilities of the modified algorithm. Further results, software used, and a detailed description of the experimental uncertainty can be found in the appendices.

Chapter 2

Background

This chapter begins with a review of aerodynamic theory with respect to two dimensional airfoils, wind turbines, and wind turbines in steady yaw. The aerodynamic review is followed by a review of multi-hole pressure probes, including an explanation of how they are used and a review of their use in the literature. A review of tuft flow visualization is then presented, again including an explanation of the method and a review of the relevant literature. Finally, the concept of experimental uncertainty and its quantification is reviewed in Appendix B as it applies to this work. These reviews are important for understanding the technologies discussed in this thesis, as well as for interpreting the experimental results. For a more detailed explanation of wind turbine aerodynamics, see [2] and [3].

2.1 Review of Wind Turbine Aerodynamics

The review of wind turbine aerodynamics is divided into three sections: a review of two dimensional airfoils, a review of three dimensional wind turbine aerodynamics, and a discussion of the aerodynamics of a wind turbine in steady yaw conditions and corresponding theoretical models.

2.1.1 Two Dimensional Airfoils

When a body is immersed in a moving fluid, a pressure distribution is formed over its surfaces which may be integrated to calculate the forces acting on the body [7]. Generally,

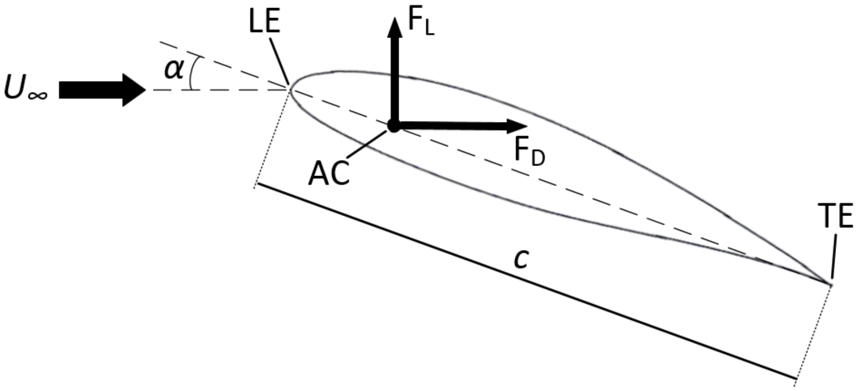

Figure 2.1: Diagram of 2D airfoil forces and geometry

these forces are resolved into a stream-wise component, called drag, and a component perpendicular to the stream, called lift. Airfoils are designed with the intention of maximizing the lift force generated in a given flow while simultaneously minimizing the drag force. A labelled diagram detailing the geometry of an airfoil, as well as the forces it may experience in a flow, is provided in Figure 2.1. Here, LE is the leading edge, TE is the trailing edge, c is the chord or distance between the leading edge and trailing edge, U_∞ is the upstream flow speed, and α is the angle of attack defined as the angle between the chord line and the flow direction. The lift force, F_L, and the drag force, F_D, act through the aerodynamic center (AC) of the airfoil, typically located a distance $c/4$ from the leading edge.

The lift and drag forces acting on a two dimensional blade per unit span can be calculated using Equations (2.1) and (2.2) [7]:

$$F_L = \frac{1}{2} C_L \rho U_\infty^2 A_{span} \tag{2.1}$$

$$F_D = \frac{1}{2} C_D \rho U_\infty^2 A_{span} \tag{2.2}$$

where C_L is the non-dimensional lift coefficient, C_D is the non-dimensional drag coefficient, ρ is the density of the fluid, and A_{span} is the planform area of the blade, defined as the chord length multiplied by the span length of the airfoil into the page. The lift and drag coefficients are generally derived either from computational fluid dynamics (CFD) models or through wind tunnel testing as they are dependent on the design of the airfoil, the angle of attack, and the Reynolds number, Re [7], defined in Equation (2.3):

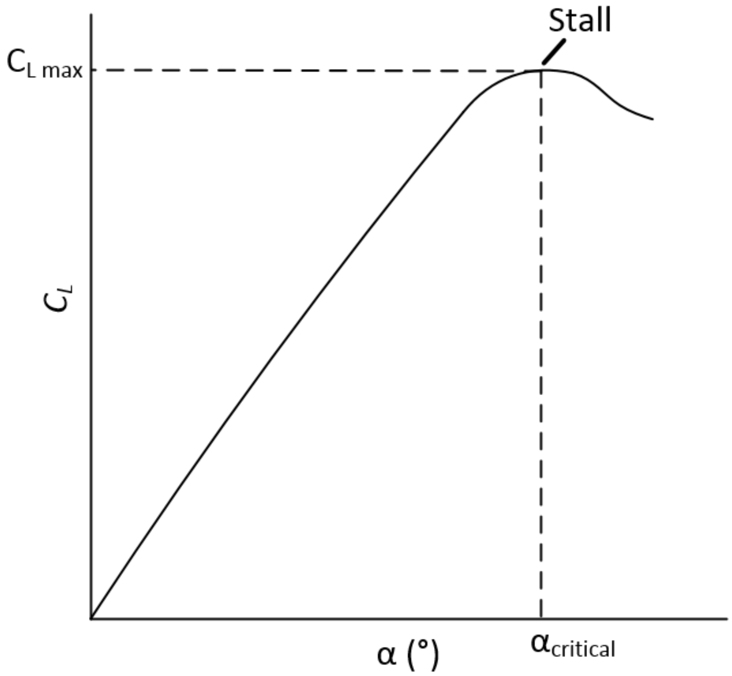

Figure 2.2: Generic lift coefficient curve plotted against the angle of attack

$$Re = \frac{\rho U_\infty c}{\mu_{dyn}} \tag{2.3}$$

where μ_{dyn} is the dynamic viscosity of the fluid.

The lift and drag coefficients of an airfoil are often defined as a function of the angle of attack. A typical plot of the lift coefficient vs. the angle of attack is provided for reference in Figure 2.2. In the figure, the lift coefficient increases linearly with the angle of attack until it tapers off to a maximum. The maximum lift coefficient occurs at the critical angle of attack, $\alpha_{critical}$, which is generally between 15° - 20° for wind turbine airfoils. As the angle of attack increases above $\alpha_{critical}$, the lift coefficient decreases significantly. In contrast, at α ¡ $\alpha_{critical}$, the drag coefficient is at a minimum, and increases significantly at higher values of α.

The reason for this sudden decrease in lift and increase in drag at α ¿ $\alpha_{critical}$ is known as stall [7]. Stall occurs when the boundary layer of the flow over the airfoil begins to separate from the surface, significantly changing the pressure distribution over the airfoil. While the pressure side of the airfoil (the bottom side in Figure 2.1) continues to experience

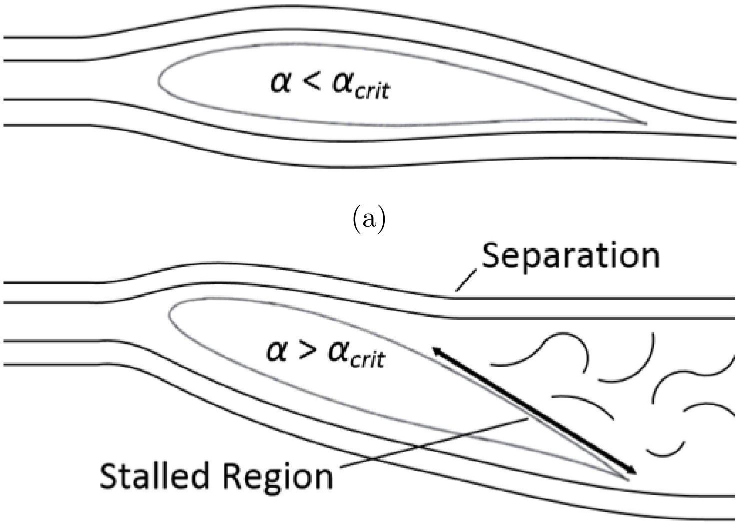

(a)

(b)

Figure 2.3: Diagram of (a) attached flow at $\alpha < \alpha_{critical}$ and (b) stalled flow at $\alpha > \alpha_{critical}$ in flow going left to right

attached flow, the suction side (the top side in Figure 2.1) experiences flow separation. The separated boundary layer causes a wake of low-pressure, highly turbulent flow to form behind the airfoil. A diagram demonstrating attached and stalled flow is provided in Figure 2.3.

2.1.2 Wind Turbine Aerodynamics

Basic aerodynamics of operating wind turbines is primarily based on the expansion of the two dimensional airfoil theory to a three dimensional blade, while also accounting for the rotational speed of the wind turbine rotor. Before discussing the air flow over the rotating blades, it is important to review the components of a wind turbine and the associated terminology so that the flow descriptions are clear. Labelled diagrams of a typical wind turbine from the front and side views are provided in Figure 2.4. Here, U_∞ is the upstream wind velocity, h_t is the hub height, R is the rotor radius, and Ω is the rotational speed of the rotor. The pitch of the blade, β, is defined as the angle between the chord line of the airfoil and the rotational plane; the yaw-offset angle, γ, is the angle between the wind direction and the rotor axis; and the azimuthal position of the blade, ψ is defined as the blade orientation defined from a 0° value at the 6 o'clock position, where clockwise rotation

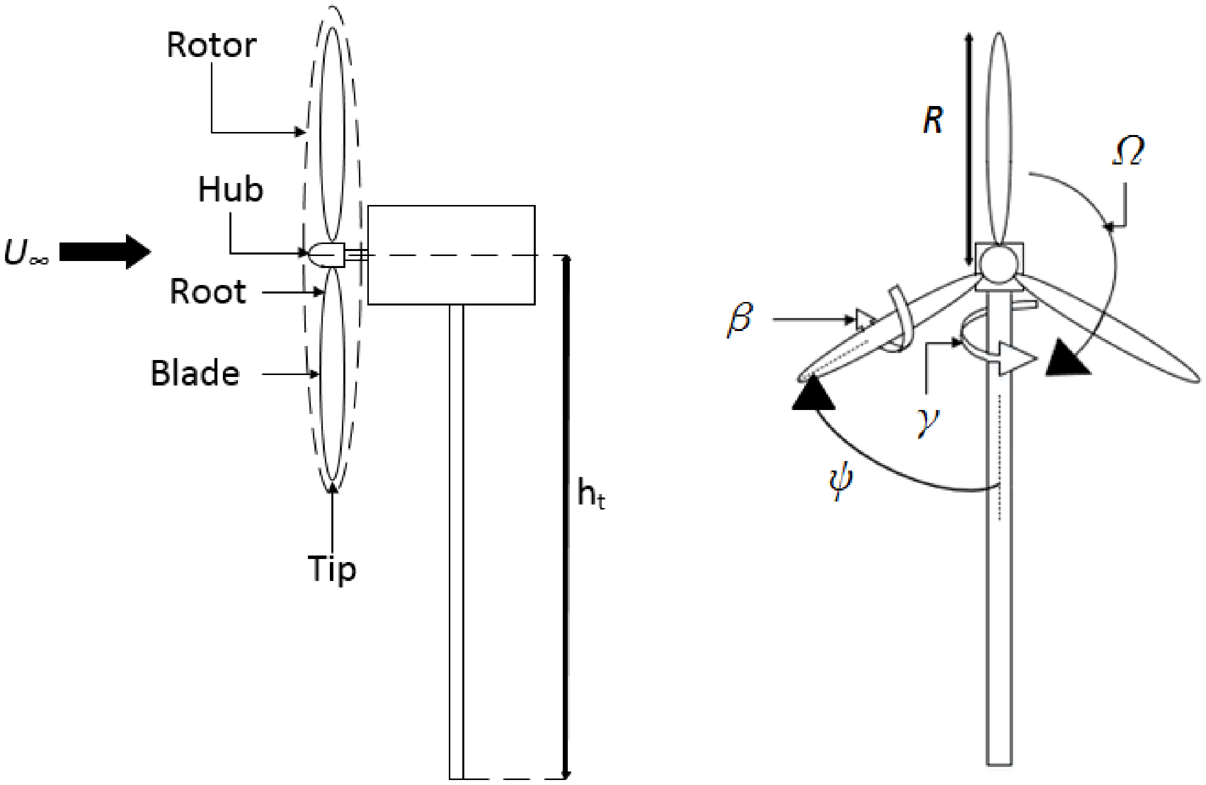

(a)

(b)

Figure 2.4: Labelled diagram of a horizontal-axis wind turbine from the (a) side view and (b) front view from upwind location

is positive. Note that these diagrams depict an upwind horizontal axis wind turbine design, which was the only wind turbine configuration investigated during this project.

As air flows over the rotating wind turbine blades, the aerodynamic shape of the airfoil generates lift on the blades. This lift is converted to torque by the rotor, which turns the generator and generates power. Large-scale turbines typically draw power from the grid to overcome their initial inertia and begin rotation, while smaller, lighter rotors can begin turning due to the wind alone. In both cases, the rotating wind turbine blades extract energy from the wind to drive a generator. This energy extraction process is often simplified using a rotating-disc [8] model, which is depicted in Figure 2.5.

The actuator disc model assumes that only the mass of air flowing through the disc is affected by the energy extraction, and all surrounding air is unaffected. The velocity of the

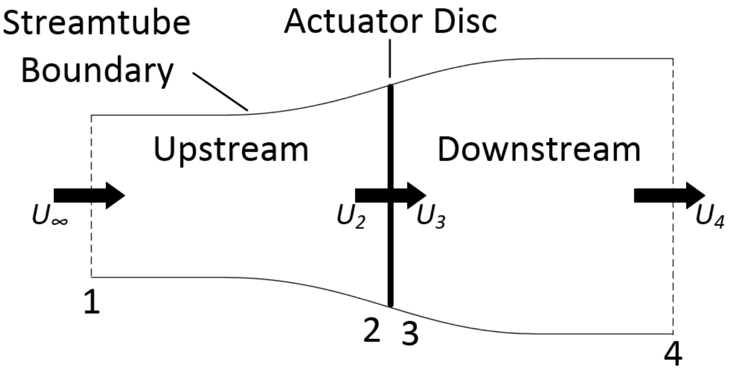

Figure 2.5: Diagram of the actuator disc model for air flow passing through a wind turbine

wind passing through the actuator disc is slowed as its kinetic energy is extracted. If the boundaries of the flow passing through the disc are extended upstream and downstream of the turbine rotor, a streamtube is formed which varies in cross-sectional area as it passes through the turbine and the velocity is decreased, in accordance with continuity laws.

The decrease in velocity of the air passing through the turbine is represented by the axial induction factor, a. The relationship between the wind speeds at points 1, 2, 3 and 4 in Figure 2.5 are established in equations (2.4) and (2.5):

$$U_2 = U_3 = U_\infty(1-a) \tag{2.4}$$

$$U_4 = U_\infty(1-2a) \tag{2.5}$$

where U_∞, U_2, U_3 and U_4 represent the wind velocity upstream, immediately upstream, immediately downstream, and far downstream of the rotor disc, respectively.

The rotation of the wind turbine rotor also has a rotational effect on the air passing through the actuator disc. In terms of Newton's third law of motion, the generation of torque on the wind turbine blades by the flowing air results in an opposite torque being applied on the wind by the turbine blades. The torque on the wind passing through the rotor area causes a rotation of the wake downstream of the turbine. The change in the tangential velocity of the air as it passes through the swept area is signified by the tangential flow induction factor, *a'* [8]. The tangential flow induction factor can be estimated using equation (2.6) :

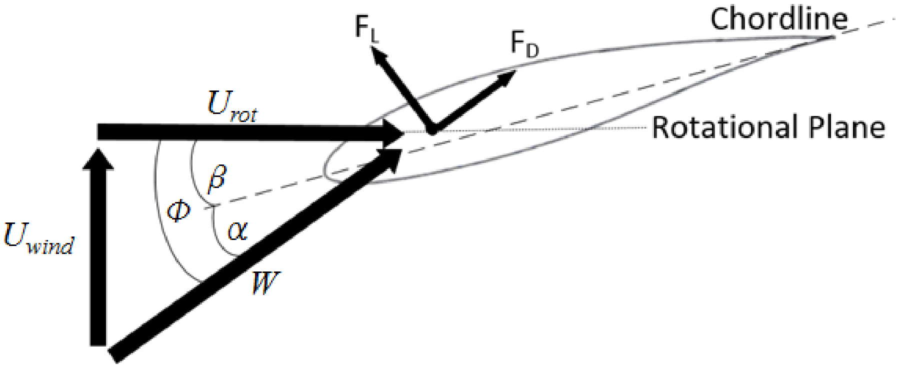

Figure 2.6: Airfoil diagram depicting the velocity triangle between U_{wind}, U_{rot} and W

$$a' = \frac{\omega}{2\Omega} \tag{2.6}$$

where ω is the angular velocity of the downstream wake.

Looking at the two dimensional airfoil presented in Figure 2.1, it is found that several changes are required for the velocity diagram to accurately reflect the velocities of flow passing over a rotating wind turbine blade. An airfoil that is rotating about an axis will experience both the upstream velocity as well as a relative air velocity caused by the rotation of the blade passing through the air. An updated diagram must also accommodate the axial and tangential flow induction factors. An updated version of the two dimensional airfoil diagram which includes these changes is presented in Figure 2.6.

In Figure 2.6, U_{wind} represents the velocity of the wind directly upstream of the rotor, U_{rot} represents the tangential velocity of the blade motion, W is the resulting relative wind speed, and ϕ is the sum of the blade pitch, β, and the angle of attack, α. The relationship between the three velocities is typically called the velocity triangle, and the geometry and interactions within the velocity triangle are critical background for the subject matter of the projects presented. Given the influence of the induction factors, these wind speeds can be defined using equations (2.7), (2.8), and (2.9). Here, r is the local radius of interest.

$$U_{wind} = U_2 = U_\infty(1 - a) \tag{2.7}$$

$$U_{rot} = \Omega r(1 + a') \tag{2.8}$$

$$W = \sqrt{U_{wind}^2 + U_{rot}^2} \tag{2.9}$$

The velocity triangle depicts several key relationships. The angle between the rotational plane of the rotor and the relative wind speed is labelled as ϕ, which is the sum of the blade pitch, β, and the angle of attack, α, which is now defined as the angle between the chordline and the relative wind velocity, W. The flow angle ϕ can be calculated using simple trigonometry, as shown in equation (2.10). After solving for ϕ, the angle of attack, which is one of the key variables of interest in this project, is defined using equation (2.11).

$$\tan\phi = \frac{(1-a)U_\infty}{\Omega r(1+a')} \tag{2.10}$$

$$\alpha = \phi - \beta \tag{2.11}$$

2.1.3 Atmospheric Boundary Layer

The actuator disc model presented in the previous section is an invaluable tool for understanding the physics of air flow through a rotating wind turbine rotor. However, it is important to remember that it is a simplification of a more complicated process. One complication present in actual wind turbine aerodynamics is the presence of the atmospheric boundary layer and wind shear.

As air flows over the Earth's terrain, frictional forces act against the wind. The strength of this effect is dependent on the surface roughness [2], but it always results in the development of an atmospheric boundary layer, in which the velocity of each layer of air flow is partially slowed by the layer below it. The result is an increase in the wind velocity as a function of the elevation up to a point, as demonstrated in Figure 2.7.

As demonstrated in Figure 2.7, the effect of the boundary layer is reduced at higher elevations, which is one reason that wind turbines are typically placed on tall towers. However, small-scale wind turbines that are mounted on shorter towers are often affected by the atmospheric boundary layer, which results in an uneven distribution of wind velocities over the vertical span of the rotor. The wind turbine blades then experience a cyclical loading as they rotate, which can lead to fatigue, wear, and eventually failure. A technique for measuring the effect of the boundary layer on the wind velocity distribution is developed in this thesis and described in Sections 2.2.2 and 4.1.4.

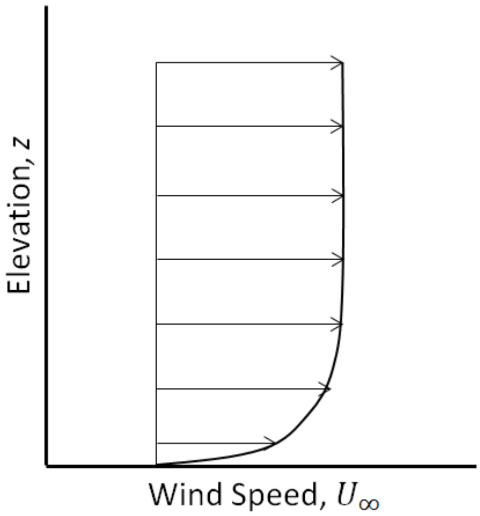

Figure 2.7: Demonstrative diagram of the boundary layer effect on the upstream wind speed

2.1.4 Performance Parameters

When examining the performance of wind turbines, several dimensionless parameters are commonly used for characterizing the rotational speed of the turbine and power generated. Such practice is common in fluid dynamics, as it allows for direct comparisons between flows of different sizes, speeds or fluids. The most common dimensionless parameter in fluid dynamics is likely the Reynolds number, which for flow over an airfoil is calculated using equation (2.3).

A common dimensionless parameter used in the discussion of wind turbine experimentation is the tip speed ratio, λ. The tip speed ratio is defined as the ratio between the blade tip speed and the freestream wind velocity, as expressed in equation (2.12). Typically, wind turbines operate at tip speeds ranging from 3 to 10, indicating that wind turbines with larger blades tend to rotate much slower than small-scale wind turbines in the same wind.

$$\lambda = \frac{\Omega R}{U_\infty} \tag{2.12}$$

When studying flow at a specific or local blade radius, the local tip speed ratio is used, defined as:

$$\lambda_r = \frac{\Omega r}{U_\infty} \tag{2.13}$$

The power producing potential of a wind turbine is typically presented as the ratio of the power captured by the turbine rotor relative to the total amount of power in the wind travelling through the same swept area. This ratio is known as the power coefficient, C_p, and is expressed as:

$$C_p = \frac{P}{\frac{1}{2}\rho U_\infty^3 A} \tag{2.14}$$

where P is the aerodynamic rotor power, and A is the swept area of the rotor, πR^2. Using the first law of thermodynamics to relate the rotor power to the axial induction factor, the power coefficient can also be expressed using equation (2.15):

$$C_p = 4a(1-a)^2 \tag{2.15}$$

From equation (2.15), it can be shown that the power coefficient reaches a maximum of 16/27 when the axial induction factor $a = 1/3$. The value of $C_p = 16/27$ is known as the Betz limit [8], and it represents the theoretical maximum amount of power that a rotating wind turbine blade can harvest from the wind. Due to inefficiencies in wind turbine design, as well as unavoidable losses, most wind turbines operate with a power coefficient between 0.2 to 0.45.

A thrust coefficient C_T can also be defined using the axial induction factor, as in Equation (2.16) derived from momentum theory:

$$C_T = 4a(1-a) \tag{2.16}$$

2.1.5 PROPID

When developing the aerodynamic design of a wind turbine blade, the values of certain variables or characteristics must be assumed. The free variables can then be calculated through an iterative process to develop a complete design. Typically, the assumed variables are chosen to be performance parameters such as those described in the previous section. This allows the designer to input the characteristics of their blade and calculate the performance parameters that would result. This is often an iterative process, as certain combinations design characteristics or limitations may not be capable of reaching the desired performance.

The iterative method most commonly used for the design of wind turbine blades is the Blade Element Momentum (BEM) method [8]. The method consists of dividing the length of blade into sections, or elements, and iterating through the design of each element until a consistent set of characteristics and performance parameters is achieved. This can be a time consuming process to conduct by hand, and several software packages have therefore been developed to conduct the calculations for designers given a set of fixed and free variables. One such package is PROPID developed by the UIUC Applied Aerodynamics Group at the University of Illinois [9]. As will be discussed in Chapter 3, the wind turbine blades used in this thesis were both designed using PROPID [9], and several performance parameters of the blade were calculated using the original design codes.

PROPID [9] uses an inverse design method in which the performance parameters and airfoil properties are input to the code, and the software uses the BEM method to calculate the blade properties required to reach this performance. For example, airfoil data, operating conditions, design constraints and a desired axial induction distribution may be set as inputs, and the software will calculate the chord and twist distribution that provide a performance as close to the desired values as possible. Any combination of design variables can be specified as inputs, provided that an equal number of parameters are left free to be calculated by the software.

More details about the PROPID codes used to design the test blades in this thesis can be found in [10] and [11]. Model outputs relevant to this project are presented in Sections 3.3.1, 3.4.1, and 4.1.3.

2.1.6 Wind Turbine Aerodynamics in Steady Yaw

To this point, wind turbine aerodynamics and related equations have been defined for a wind turbine that is aligned with the upstream wind direction. That is to say that the velocity triangle and airfoil diagram provided in Figure 2.6 was representative of the flow over a wind turbine blade with a 0° yaw-offset. When a wind turbine is oriented with a non-zero yaw offset, the aerodynamics become much more complex. For example, when the wind turbine is yawed out of the wind, the angle of attack will oscillate continuously as the rotation of the turbine takes the blade towards and away from the upstream wind. The wake downstream of the turbine will also no longer be aligned with the axial direction of the turbine, indicating that the induction of the wind by the turbine is also affected by the yaw-offset. In this section, two models for calculating the variation in the angle of attack for a wind turbine blade in a steady yaw case will be discussed: the Burton *et al.* model [12] and the Morote model [13].

Burton *et al.* Yaw Model

A model for calculating the wind turbine blade angle of attack in a steady yaw case was assembled from various models and theories in the literature and presented by Burton *et al.* [12]. As described by Burton *et al.* [12], the first difference to consider between the flow through an aligned and an unaligned wind turbine is the skew of the wake. When the wind turbine is aligned with the flow, the wake of the turbine propagates downstream in the axial direction. However, when the turbine is yawed, transverse pressure gradients cause the wake downstream to skew sideways, resulting in a skew angle χ between the centre line of the wake and the axis of rotation [12]. A diagram depicting the skew angle χ is provided in Figure 2.8. Using a simplified vortex cylinder model of a yawed actuator disc [12], an estimate of the skew angle can be calculated using equation (2.17).

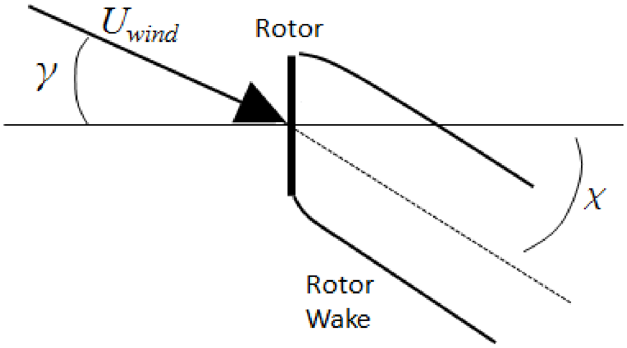

Figure 2.8: Diagram of the wind turbine wake and skew angle in a yawed flow, viewed from the top of the wind turbine

$$\chi = (0.6a + 1)\gamma \tag{2.17}$$

Then the influence of the skew angle on the induced velocity normal to the plane of the rotor, *K(*χ*)*, is given by the Coleman theory [12] in equation (2.18). Here, *K(*χ*)* represents the deviation of the inflow from the values predicted by standard BEM theory, estimated via rigid cylindrical vortex wake theories.

$$K(\chi) = 2\tan(\frac{\chi}{2}) \tag{2.18}$$

Equation (2.17) assumes that the wake downstream of the wind turbine does not expand as it propagates. In reality however, the wake does expand, which generates velocities in the radial direction. The radial velocities cause a normal induced velocity which also has an influence on the angle of attack and the aerodynamics of the rotating wind turbine blade. To quantify the influence of the normal induced velocity, the function $F(\mu)$ is used to determine the radial distribution of the induced velocity normal to the rotor plane [12]. The function is provided in equation (2.19), and is used in the calculation of the theoretical angle of attack.

$$F(\mu) = \frac{2\mu}{\pi}\int_0^{\pi/2} \frac{\sin^2(2\epsilon_r)}{\sqrt{(1+\mu)^2 - 4\mu\sin^2(\epsilon_r)}} \frac{1}{(\mu + \cos(2\epsilon_r))^2\cos^2(\chi) + \sin^2(2\epsilon_r)} d\epsilon_r \tag{2.19}$$

In this equation, μ is the ratio r/R and ϵ_r is the ratio of axial stress to total stress. Note that ϵ_r is not measured, but is defined by the boundaries of the integral.

Accounting for the variations in the aerodynamics due to the yaw-offset of the turbine, the model derived in Section 2.1.2 through the velocity relationships shown in Figure 2.6 can be re-evaluated to form a theoretical model for the variation in the angle of attack as a function of the azimuthal position [12]. From Burton *et al.* [12], the net velocities acting on the blade element and their relationships can be derived according to Figure 2.9. In the figure, $F_{\Omega r}$ and F_{wind} are wind velocities defined in equations (2.20) and (2.21), respectively [12].

$$F_{\Omega r} = \Omega r(1 + a'\cos\chi(1 + \sin\psi\sin\chi)) + U_\infty\cos\psi(a\cdot\tan\frac{\chi}{2}(1 + F(\mu)K(\chi)\sin\psi) - \sin\gamma) \tag{2.20}$$

$$F_{wind} = U_\infty(\cos\gamma - a(1 + F(\mu)K(\chi)\sin\psi)) + \Omega r a'\cos\psi\sin\chi(1 + \sin\psi\sin\chi) \tag{2.21}$$

The flow angle ϕ can then be calculated using geometry, as in equation (2.22). With the flow angle ϕ known at each blade azimuthal position of interest, the angle of attack α can be calculated as in equation (2.11).

$$\tan(\phi) = \frac{F_{wind}}{F_{\Omega r}} \tag{2.22}$$

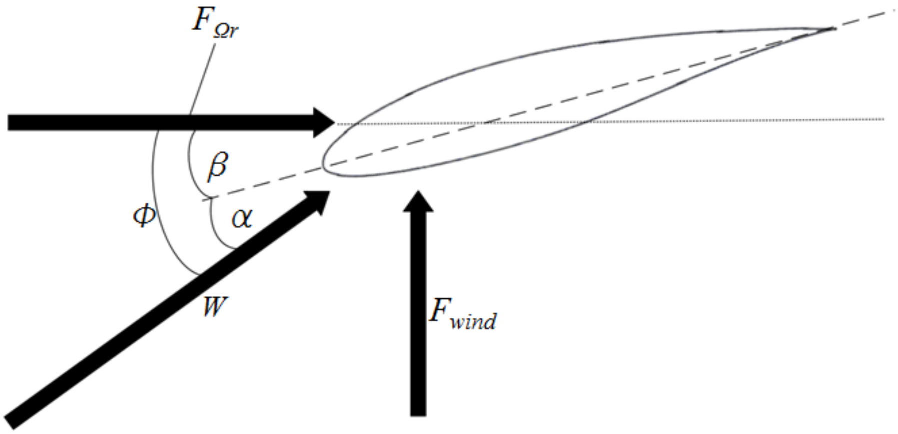

Figure 2.9: Velocity triangle between F_{wind}, $F_{\Omega r}$ and W in yawed conditions

Morote Model

While the Burton *et al.* [12] angle of attack model is presented as an appropriate baseline, recent publications show that accurately modelling the angle of attack distribution on wind turbine blades operating in yawed conditions is not a solved problem. Morote [13] derived a different model from the same basic velocity triangle diagram shown in Figure 2.6. To simplify the beginning stage, Morote defines a geometric angle of attack which is derived purely from the velocity magnitudes while neglecting the axial and tangential induction factors, as shown in (2.23):

$$\alpha_{geom} = -\beta(r) + \arctan(\frac{U_\infty}{\Omega r}) \tag{2.23}$$

where α_{geom} is the geometric angle of attack, β is the blade pitch at the radial location r, U_∞ is the upstream wind speed and Ω is the rotational speed of the turbine rotor.

At this point, Morote [13] branches away from the Burton *et al.* [12] method. Rather than adjust the velocity triangle at the leading edge of the blade to accommodate for variations in the wake and radial velocity, Morote [13] defines an axial interference function and span-wise interference function to account for the cyclical variations in flow velocities experienced at the blade [13].

First, it is assumed that the effective (or true) angle of attack, α_{eff}, is related to the unperturbed geometric angle of attack, α_{geom}, through two interference functions, *f(r)* and *g(r)*, via an equation of the form:

$$\sin \alpha_{eff} = \sin \alpha_{geom}[f(r) + g(r)\delta \sin \phi] \tag{2.24}$$

where δ is the sine of the yaw angle, γ. It is established that the velocity normal to the rotor disc is reduced at the rotor due to the axial induction, reducing α_{geom} by an induced angle, α_i, to α_{eff}, or [13]:

$$\alpha_{eff} = \alpha_{geom} - \alpha_i \tag{2.25}$$

From the geometry, and assuming a small axial induction, the induced angle can be defined as [13]:

$$\alpha_i = \frac{a(\lambda - \delta \cos \phi)}{\cos^2 \gamma + (\lambda - \delta \cos \phi)^2} \tag{2.26}$$

By combining equations (2.24), (2.25) and (2.26), Morote [13] shows that:

$$1 - \frac{a(\lambda - \delta \cos \phi)}{[\cos^2 \gamma + (\lambda - \delta \cos \phi)^2] \tan \alpha_{geom}} = f(r) + g(r)\delta \sin \phi \tag{2.27}$$

In an axial flow, the span-wise interference becomes negligible and γ is zero. The axial interference function *f(r)* can then be defined as [13]:

$$f(r) = 1 - \frac{a_0 \lambda}{(1 + \lambda^2) \tan(\alpha_{geom0})} \tag{2.28}$$

where a_0 is the radially dependent induction factor for axial flow, and α_{geom0} is the geometric angle of attack at a 0° yaw position [13]. By inserting Equation (2.28) back into Equation (2.27) and simplifying, Morote [13] showed that the span-wise interference function can be defined as:

$$g(r) = -\sqrt{A^2 + B^2} \tag{2.29}$$

where

$$A = \frac{a_{a0}}{(1 + \lambda^2)^2 \tan(\alpha_{geom0})} \frac{\lambda(1 + \lambda^2)(r/R)}{2(1 + a_{a0})} \tag{2.30}$$

$$B = \frac{a_{a0}}{(1+\lambda^2)^2\tan(\alpha_{geom0})}(\lambda^2 - 1 - \frac{2\lambda}{\sin(2\alpha_{geom0})}) \tag{2.31}$$

Here, a_{a0} is the radially dependent azimuthally averaged induction factor for axial flow. The equation for *g(r)* is only valid at certain radial positions, which means a phase shift Δ is also required. This phase shift accounts for the change in the azimuthal position of the blade as an air particle travels over the blade chord, which causes a slight variation in the angle of attack along the chord line. The phase shift can be calculated as:

$$\Delta = \arctan\frac{B}{A} \tag{2.32}$$

With the two interference functions defined, the Morote [13] model is completed by adding the phase shift to the assumed model of Equation (2.24) as:

$$\sin\alpha_{eff} = \sin\alpha_{geom}[f(r) + g(r)\delta\sin(\phi + \Delta)] \tag{2.33}$$

While Morote [13] did compare the new model to previously published results, it should be noted that the model has only been compared to experimental data by converting the modeled angle of attack to a pressure distribution over the wind turbine blade. No validation of the two models described against experimental angle of attack measurements could be found. This shows a lack of experimental data related to the variation in the angle of attack with wind turbine yaw and blade azimuthal position and was a strong motivator for this experimental work.

2.2 Multi-Hole Pressure Probes

The aerodynamic performance of a wind turbine blade is significantly affected by the angle of attack, as was established in Section 2.1.1. The angle of attack, which can be derived from the velocity relationships over the blade using models such as those described in [7] and [13], is related to the lift and drag forces generated by the blade, as well as the eventual stall of the airfoil. However, there is a lack of experimental angle of attack data in the literature for critically validating the theoretical models presented. While the angle of attack may be estimated for a wind turbine blade being tested in a flow field, the wind velocity is generally measured upstream of the wind turbine using a meteorological tower such that the actual, impeded wind speed directly at the blade is not known. Given these complications and the necessity for data, it is posited that to accurately measure the variation in the flow behaviour and blade performance with the angle of attack, the angle of attack must also be measured directly at the leading edge of the blade.

In this section, the use of five-hole pressure probes for measuring the angle of attack will be discussed, followed by a review of the relevant literature. A five-hole probe was used in this project to measure the flow characteristics at the leading edge of the blade, which were then used to validate theoretical models as well as predict the upstream flow field.

2.2.1 Review of Multi-Hole Probes

A five-hole pressure probe is a type of multi-hole pressure probe which can measure flow velocity and direction, as well as the local and static pressure [14]. A typical multi-hole probe consists of three or more holes at the open end which each measure an independent air pressure. Here, a center hole would be cut perpendicular to the probe axis, while the surrounding holes are sloped back away from the center probe to form a pyramid shape. The pressure distribution over three collinear holes can then be used to determine the flow direction in one dimension. Adding an additional line of holes, as shown in the picture of a five-hole probe in Figure 2.10, allows for a determination of the flow direction in three dimensions [14].

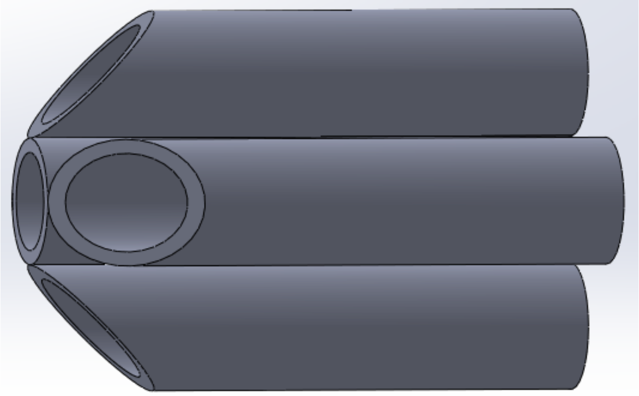

Figure 2.10: CAD image of a five-hole pressure probe tip

Five-hole pressure probes can be used to measure the flow direction in terms of both yaw, γ_f, and pitch, β_f, components relative to the probe. Generally, these types of probe require calibration to a known, uniform flow stream at different combinations of yaw and pitch angles, during which the pressure distribution over the five holes is recorded. In the following review of the literature, examples of the use of five-hole pressure probes will be discussed, as well as various methods for calibrating the probe.

2.2.2 Use of Multi-Hole Probes in the Literature

Despite the established nature of five-hole probes as a means of measuring the blade angle of attack experimentally, the use of such probes remains relatively uncommon in the literature [22]. Instead, the angle of attack is typically calculated using the simple velocity triangle model or more in depth mathematical models, such as those proposed by Morote [13] or Choudhry *et al.* [15].

The use of five-hole pressure probes has been reported in a few sources however. The most notable example of this is likely the NREL Unsteady Aerodynamics Experiments (UAE) [16] which began in 1987 and continued to 2001. In Phase VI of the UAE, experiments were conducted with a 10 m diameter, stall regulated 20 kW wind turbine based on the design of a Grumman Wind Stream 33 turbine [16]. The turbine rotor consisted of two twisted and tapered blades, and was operated in both upwind and downwind configurations. Testing was conducted in a wind tunnel at the NASA Ames Research Center in California, which has a cross-sectional area of 24.4 m by 36.6 m [16]. Given the scale of the study, the wind turbine was well equipped with measurement equipment, including five-hole pressure probes, pressure taps, strain gauges, position encoders, and more [16].

Unfortunately, measured data from the NREL experiments that can be found publicly is limited. However, the report detailing the instrumentation does provide equations necessary for relating the flow pitch angle relative to the probe and spanwise flow angle relative to the probe back to the flow angles with respect to the blade. Expressions for the local flow angle (*LFA*) and the spanwise flow angle (*SFA*) are provided in Equations (2.34) and (2.35) respectively [16]. Here, α_p is the local angle of attack with respect to the probe, β_p is the spanwise flow angle with respect to the probe, ϵ is the spanwise probe angle offset and θ is the local flow probe angle offset. The relevant geometry is demonstrated in Figures 2.11 and 2.12.

$$LFA = \arctan \frac{\cos\alpha_p * \cos(\beta_p + \epsilon) * \sin\theta + \sin\alpha_p \cos\theta}{\cos\alpha_p \cos(\beta_p + \epsilon)\cos\theta - \sin\alpha_p \sin\theta} \tag{2.34}$$

$$SFA = \arctan \frac{\cos\alpha_p \sin(\beta_p + \epsilon)}{\cos\alpha_p \cos\beta_p + \epsilon\cos\theta - \sin\alpha_p \sin\theta} \tag{2.35}$$

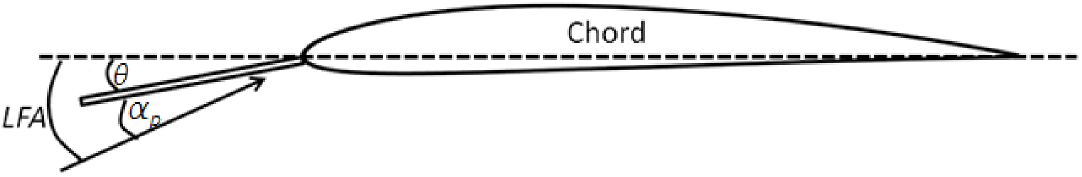

Figure 2.11: Demonstrative diagram of flow angles relative to the airfoil profile

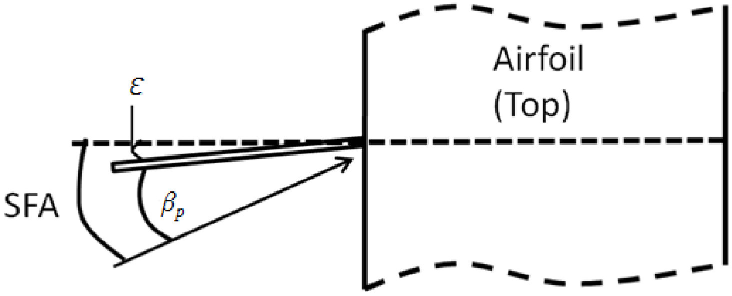

Figure 2.12: Demonstrative diagram of flow angles relative to the airfoil top view

The Unsteady Aerodynamics Experiments also resulted in the determination of several corrections required when doing experimental pressure measurements on a rotating wind turbine blade. In Phase I [17] of the UAE, the authors provide details for two corrections: minimizing the dynamic effects of the pressure transducers; and correcting for the influence of the centrifugal force on the transducers.

To avoid dynamic effects in the tubing from the blade surface pressure taps to the transducers, the tube lengths were minimized [17]. By keeping the tubing length below 0.457 m in length, gain amplifications and phase effects occurring in the tubes were found to be negligible up to a frequency of 50 Hz [16]. Because of these results, no compensation for dynamic effects was introduced by NREL in Phase VI [16].

In the UAE five-hole probe experiments, differential pressure transducers were used to measure the pressure at the tip of each probe. Experiments were completed in both axial and yawed conditions. To maintain a constant reference pressure, tubing connected each of the transducers to a common hole located in the turbine hub. To correct for centrifugal forces acting on the column of air in the reference tube, the pressure experienced by the transducers was corrected using Equation (2.36) [17]:

$$P_{atm} + P_{cf} = \frac{1}{2}\rho(r\Omega)^2 \tag{2.36}$$

where P_{atm} is atmospheric pressure and P_{cf} is the pressure measured due to the centrifugal force.

It must be noted here that the five-hole probe in Figure 2.11 is measuring the Local Flow Angle, which is not equivalent to the angle of attack due to the bound circulation close to the airfoil. In publications by Schepers and van Rooij [18], Butterfield [19], and Shen *et al.* [20], corrections based on the Biot-Savart law [8] were applied to LFA measurements to convert data to angle of attack data for study. The Biot-Savart law is defined as:

$$U_2 = -\frac{g}{2} = -aU_\infty \tag{2.37}$$

where g is the strength of the generated vorticity parallel to the rotor disc, expressed as a function of the blade circulation, Γ, the rotor radius, and the vortex helix angle, ϕ_t in Equation (2.38).

$$g = \frac{\Gamma}{2\pi R \sin\phi_t} \tag{2.38}$$

The strength of the bound circulation is therefore related to the vorticity generated by the rotor and, by extension, the induction of the rotor.

Maeda and Kawabuchi's Measurement of Pressure on a Rotating Wind Turbine Blade

Maeda and Kawabuchi [21] conducted measurements of the pressure distribution over a rotating wind turbine blade in yawed conditions. Tests were conducted using a three bladed 10 m diameter upwind test turbine with a rated power output of 8 kW. The hub height was set to 13.3 m, and the rotational speed was kept at a constant 80 rpm. A rotary encoder was used to measure the yaw angle, defined as positive in the counter-clockwise direction from above. The blade design itself was twisted and tapered, and consisted of DU and NACA airfoil profiles. Tests were conducted in the open environment, with a sonic anemometer 10 m upstream used to measure the oncoming wind speed. Data were collected for yaw angles in the range of -45° to +45° and separated into 15° increments.

Pressure taps were installed on one of the blades at radial sections at 32.5%, 50%, 70% and 90% of the blade span, with each section consisting of 60 taps on the pressure and suction sides. Two five-hole probes were mounted on the leading edge of the blade at radial locations 38.5% and 55.8% along the blade span for measuring the inflow angles. Pressure data were reduced using a non-dimensional pressure coefficient, C_p, related back to angle of attack and span-wise angle measurements, and results from the two probes were interpolated to calculate the angle of attack and span-wise angle for blade spans between the two probes. Note however that no correction from the measured local flow angle to angle of attack is described in the publication [21].

After testing, data was sorted into bins for analysis, both by yaw position (± 6.0°) and angle of attack (± 0.5°). Results showed that, at a 0°yaw-offset, the inflow velocity experienced by the blade was essentially uniform with the azimuthal location of the test blade. However, when the turbine was yawed ± 45° from the oncoming wind, the inflow velocity fluctuated significantly throughout the rotation, increasing as the blade rotated towards the wind and decreasing as the blade rotated away from the wind. Maeda and Kawabuchi [21] explain that the inflow velocity varied because it is a measure of the wind velocity relative to the blade, and it therefore increases as the blade and wind travel towards each other and decreases as they travel the same direction. A plot of the inflow velocities measured is presented in Figure 2.13a [21].

Extending the variation in the inflow velocity to the angle of attack, Maeda and Kawabuchi [21] found that, at a 0° yaw-offset, the angle of attack experienced a variation as high as 2.5° with azimuthal position, hitting a maximum when the blade was at the 12 o'clock position and a minimum when the blade was at the 6 o'clock position. The variation in α was posited to be caused by the influence of the wind shear, which would decrease the upstream wind speed experienced at the lower part of the turbine rotation relative to the upper part of the rotation.

When the turbine was yawed, it was found that at a -45° yaw-offset, there was a greater variation in the angle of attack than with a +45° yaw-offset, and that both cases followed the general trend observed in the 0° yaw case. No reason was given for the difference in amplitude of the change in α with azimuthal position. Of note is that the azimuthal variation in α measured at a yaw-offset of -45° was opposite to the variation observed in the inflow velocity. Azimuthal variation in the angle of attack measurements in yawed conditions will be discussed further in Section 4.1.2. The measured angle of attack distributions can be seen in Figure 2.13b [21].

In terms of the span-wise angle (labeled by Maeda and Kawabuchi [21] as "slip angle β" Figure 2.13c), it was observed that the angle remained fairly constant with azimuthal position during the 0° yaw-offset case. However, in the two yawed cases, the span-wise angle oscillated with the blade rotation, reaching a peak at approximately 270° azimuth

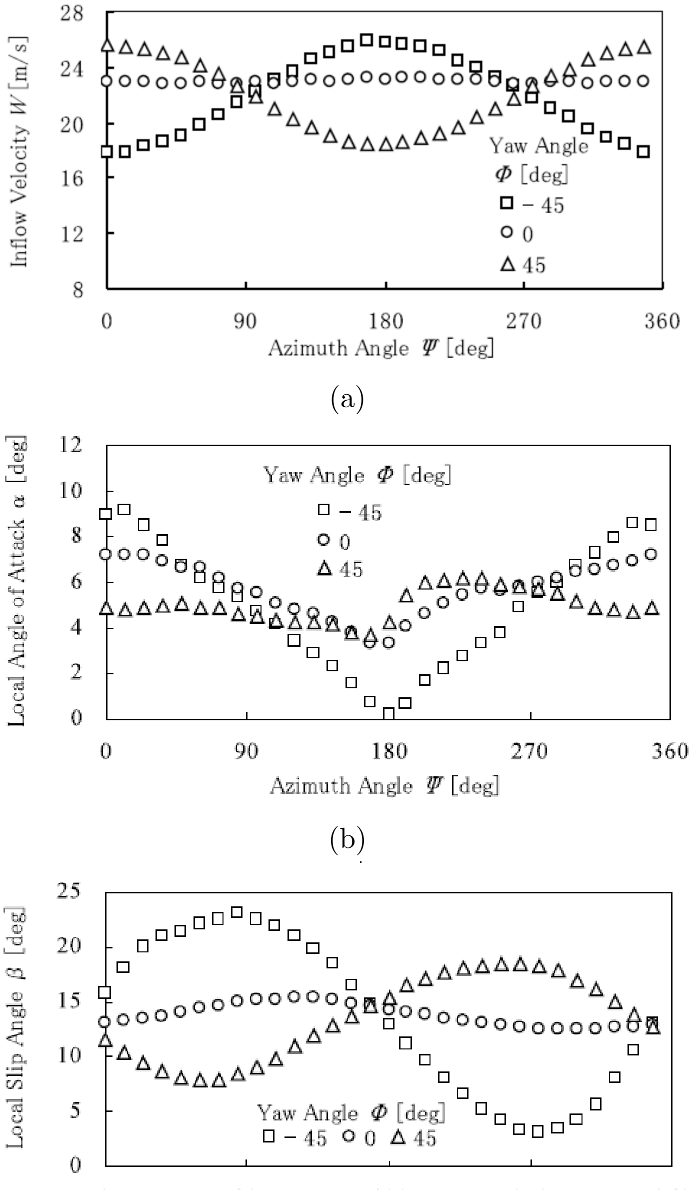

(a)

(b)

(c)

Figure 2.13: Measured (a) Inflow Velocity, (b) Angle of Attack and (c) span-wise flow angle distributions, reprinted from Maeda and Kawabuchi [21] with permission

and a low at approximately 90° azimuth in the -45° yaw-offset case, and the opposite was found for the +45° yaw-offset case. The variation in the span-wise angle was attributed to the upstream wind velocity traveling cyclically inboard and outboard along the blade [21]. Note here that a 0° azimuthal position is defined as the blade being at the 12 o'clock position, which is a 180° offset from the convention used in this thesis.

While the study by Maeda and Kawabuchi [21] does show the potential of measuring the incoming flow angles using a five-hole probe, only a limited number of test cases are presented in the literature (*e.g.* only one tip speed ratio, only 0° and ± 45° yaw positions reported, etc.). Given that this is one of few published studies which measure the flow angles at the leading edge of the blade, this shows that there is a need for more experimental measurements of the angle of attack and span-wise angle, and how these angles may vary with tip speed ratio, yaw-position and radial location.

Moscardi Development and Calibration of a Five-Hole Pressure Probe

The five-hole pressure probe used in this project was constructed and calibrated as described by Moscardi and Johnson [22]. In this section, calibration methods considered and the actual calibration experiments will be discussed. For more details on the fabrication of the five-hole probe, the corresponding electronics board, and the blade in which the probe was mounted, see Section 3.3.

From the beginning, the five-hole probe was intended to be installed on the leading edge of a 3D printed wind turbine blade with the required electronics housed within the blade section, meaning limited space was available and fast data acquisition was required. It was found that a non-nulling calibration technique was suited to these requirements [24]. For a non-nulling calibration, the probe must be introduced to a known flow, at which the pressure distributions over the multiple holes can be measured at various orientations. Each distribution of pressures over the multiple holes then corresponds to a set of pitch, yaw, and velocity values.

To determine the best calibration technique suited to the project, literature related to five-hole pressure probes was reviewed in detail. Much of the work is based on Dudzinsky and Krause [25], who showed that by normalizing the pressures measured over the probe, the freestream total and static pressure was no longer required to determine the flow direction. Dudzinsky and Krause [25] found that the best way to normalize the pressures for a five-hole probe was to use the difference between the center hole pressure and the average of the pressures measured by the surrounding four holes, as in Equation (2.39):

$$P_{norm} = P_5 - \frac{1}{4}(P_1 + P_2 + P_3 + P_4) \tag{2.39}$$

where P_{norm} is the normalized pressure, P_5 is the center hole pressure, and the remaining P values are the pressures measured by the surrounding holes.

Several calibration techniques were investigated, all of which use the pressure normalization technique introduced in [25]. These methods included the method used introduced by Dudzinsky and Krause themselves [25], the sectoring method first proposed by Gallington [27], and a modified version of the sectoring method described by Paul *et al.* [28].

Beginning with Dudzinsky and Krause [25], a single surface, or zone, is defined where four different pressure coefficients can be calculated. The first two are the pitch and yaw pressure coefficients, C_{p_p} and C_{p_y} respectively, used to determine flow direction:

$$C_{p_p} = \frac{P_1 - P_3}{P_5 - \bar{P}} \tag{2.40}$$

and

$$C_{p_y} = \frac{P_2 - P_4}{P_5 - \bar{P}} \tag{2.41}$$

where $\bar{P} = \frac{1}{4}(P_1 + P_2 + P_3 + P_4)$ is the average of the pressures measured by the four surrounding holes. Then, the total and static pressure coefficients, which are used to calculate the velocity of the flow, are defined as:

$$C_{p_{total}} = \frac{P_5 - P_{total}}{P_5 - \bar{P}} \tag{2.42}$$

and

$$C_{p_{static}} = \frac{\bar{P} - P_{static}}{P_5 - \bar{P}} \tag{2.43}$$

The single surface calibration established by Dudzinsky and Krause [25] is appropriate for measuring flow angles that are close to collinear with the probe itself (*e.g.* within ± 25°). However, at high flow angles, separation can occur on the downstream hole and cause significant changes to the pressure distribution measured. To correct for this, a multi-zone

Table 2.1: Summary of Pressure Coefficient Equations [28]

Var	Zone 1	Zone 2	Zone 3	Zone 4	Zone 5
$\bar{P}$	$\frac{P_4+P_5+P_2}{3}$	$\frac{P_1+P_5+P_3}{3}$	$\frac{P_4+P_5+P_2}{3}$	$\frac{P_1+P_5+P_3}{3}$	$\frac{P_1+P_2+P_3+P_4}{4}$
D	$P_1-\bar{P}$	$P_2-\bar{P}$	$P_3-\bar{P}$	$P_4-\bar{P}$	$P_5-\bar{P}$
C_{p_α}	$\frac{P_1-P_5}{D}$	$\frac{P_1-P_3}{D}$	$\frac{P_5-P_3}{D}$	$\frac{P_1-P_3}{D}$	$\frac{P_1-P_3}{D}$
C_{p_β}	$\frac{P_2-P_4}{D}$	$\frac{P_2-P_5}{D}$	$\frac{P_2-P_4}{D}$	$\frac{P_5-P_4}{D}$	$\frac{P_2-P_4}{D}$
$C_{p_{tot}}$	$\frac{P_1-P_{tot}}{D}$	$\frac{P_2-P_{tot}}{D}$	$\frac{P_3-P_{tot}}{D}$	$\frac{P_4-P_{tot}}{D}$	$\frac{P_5-P_{tot}}{D}$
$C_{p_{st}}$	$\frac{P-P_{st}}{D}$	$\frac{P-P_{st}}{D}$	$\frac{P-P_{st}}{D}$	$\frac{P-P_{st}}{D}$	$\frac{P-P_{st}}{D}$

approach was suggested by Gallington [27]. In the multi-zone approach, different coefficient equations are defined for each hole, to be used when their corresponding hole measures the maximum pressure. By establishing coefficients for each hole independently, a hole that is undergoing separation can be neglected by calculating the coefficients using the remaining four holes. For example, if hole 1 is experiencing the maximum pressure, it is likely that hole 3, opposite hole 1, may be experiencing separation. Hole 3 would then be neglected in the calculation of pressure coefficients for this set of measurements.

The sectoring approach defined by Gallington [27] was reviewed and modified by Paul *et al.* [28]. In the pressure coefficient equations established by Gallington [27], the pressure of the center hole, hole 5, was typically ignored. Paul *et al.* [28] considered the center hole pressure to be necessary for accurately depicting the pressure distribution over the five holes. A new set of pressure coefficient equations was established, and this set was used by Moscardi and Johnson [22] in calibrating their five-hole pressure probe. The Paul *et al.* [28] set of pressure coefficients are presented in Table 2.1 and can be used to establish flow angles up to $\pm$ 50°.

The fabricated five-hole probe was calibrated in an open jet wind tunnel for pitch and yaw positions of $\pm 50°$[22]. Calibration experiments were conducted at a single Reynolds number, chosen to approximate the expected Reynolds number that the blade would experience. A single Reynolds number was considered sufficient given the minimal impact of the Reynolds number on the functionality of multi-hole probes [29]. Given an expected range of velocities on the wind turbine blade of 25 m/s to 33 m/s, calibration was conducted at a constant 29 m/s velocity [22]. Steps of 5° were used to traverse through the range of angles, selected due to its common use in the literature. After several preliminary calibration measurements conducted at low and high inflow angles, it was found that taking 400 measurements per probe orientation was sufficient for stabilizing the standard deviation. Therefore, 400 calibration measurements were recorded at each probe orientation. More details concerning the traversing device used to set the probe orientation can be found in Moscardi and Johnson [22].

After conducting the calibration experiments and calculating the pressure coefficients at each position, an interpolation method was required to relate new pressure distribution measurements back to the known pitch and yaw positions measured during calibration. Moscardi and Johnson [22] compared several interpolation techniques, including cubic and linear interpolation, by conducting pressure measurements with the same wind tunnel and traverse system at known pitch and yaw positions other than those used in the calibration grid. By comparing the interpolated results to the known position, the errors associated with each method could be estimated. While the interpolation methods were found to give nearly identical results, cubic interpolation was chosen as the technique to use moving forward as it provided more accurate velocity measurements [22].

The developed five-hole pressure probe and corresponding electronics were installed in a wind turbine blade mounted to the University of Waterloo test turbine, as will be discussed in Section 3.3. Preliminary experiments were conducted in which the velocity, pitch angle and slip angle relative to the five-hole probe were measured as a function of time [22]. Tests were conducted at a 30° yaw-offset, and results showed an oscillation in the measurements consistent with those found by Maeda and Kawabuchi [21].

Characterizing Upstream Flow Field with Five-Hole Probe Measurements

Multi-hole pressure probes are most often used for measuring a flow velocity and direction. However, pressure measurements can also be used to characterize the upstream flow field. Petersen *et al.* [30] have developed a method for measuring the flow velocity and characteristics directly at the leading edge of the blade using five-hole pressure probes, and then extrapolating these characteristics upstream to calculate the axial and tangential induction factors, the undisturbed wind speed at the turbine location, the turbulence intensity of the flow and a shear profile of the wind at the location of the blade.

The first step of the method proposed is to use the pressure coefficients calculated via the probe calibration discussed in Section 2.2.2 to determine the flow angles and relative velocity at the leading edge of the blade. These measurements are then used to determine the velocity in Cartesian coordinates, u, v, w, at the blade. The velocities u, v, w can be defined as the Cartesian components of the velocity at the rotor, U_2, defined in Figure 2.5.

At this point, the contribution to the relative wind caused by the rotation of the blade must be subtracted [30].

The axial wind vector component, u, is affected by the axial induction of the rotor plane as expressed by Equation (2.4), where U_∞ is the upwind velocity and U_2 is the velocity at the rotor plane. Equation (2.16) is invalid for axial induction factors greater than 0.4. Petersen *et al.* therefore suggest the use of an alternate equation relating C_T to a proposed by Madsen *et al.* [31], provided in Equation (2.44). This equation was derived by Madsen *et al.* [31] through numerical simulations of an axis symmetric actuator disc model while studying modifications to the traditional BEM design method.

$$a = 0.0892C_T^3 + 0.0545C_T^2 + 0.2512C_T \tag{2.44}$$

The definition of the thrust coefficient is derived from the loading on the actuator disc, expressed via the lift and drag coefficients projected to the axial direction, C_y [31]:

$$C_y = C_l \sin(\phi) - C_d \cos(\phi) \tag{2.45}$$

The infinitesmal thrust dT on an annular element of length dr can then be defined as [31]:

$$dT = \frac{1}{2}\rho V_{rel_{xy}}^2 C_y c N_B dr \tag{2.46}$$

where $V_{rel_{xy}}$ is the relative velocity projected onto a section of the blade, N_B is the number of blades and $2\pi r$ is the swept distance of the blade element. The local thrust coefficient is then defined as:

$$C_T = \frac{dT}{\frac{1}{2}\rho U_\infty^2 2\pi r dr} = \frac{V_{rel_{xy}}^2 C_y c N_B}{U_\infty^2 2\pi r} \tag{2.47}$$

By assuming an initial U_∞ value and iterating through equations (2.47), (2.44) and (2.4), the axial induction factor and upstream wind speed can be calculated. By sorting pressure measurements into azimuthal position bins, the variation in the upstream wind speed with probe height can be determined and used as an estimate of the shear profile of the wind.

Petersen *et al.* [30] demonstrated this method using five-hole probe measurements taken from the DANAERO project [32], which involved measuring the inflow at a radius of 36.5 m on a 53.5 m blade belonging to a Siemens 3.6 MW wind turbine. More details about the DANAERO experiments can be found in [30]. The analysis method was also applied to simulated pitot tube measurements generated using HAWC2aero [30].

Simulations conducted showed close agreement between the generated wind field and the wind field predicted from the simulated five-hole probe measurements. To validate the method for the DANAERO experiments, the calculated wind field at the five-hole probe was compared to measured wind speeds at several masts upstream. Pitot probe measurements were sampled based on azimuthal location and used to calculate the velocity profile in the vertical direction. Comparisons to mast measurements showed close agreement, indicating that five-hole probe measurements can provide an accurate estimate of the flow field upstream of the wind turbine [30].

2.3 Tuft Flow Visualization

The techniques reviewed thus far have provided a method for measuring the angle of attack directly at the leading edge of a blade, as well as extrapolating from such measurements to characterize the upstream flow field. However, as was established in Section 2.1.1, while increasing angles of attack typically results in an increasing lift and turbine output, at high angles of attack the flow over the blade can also separate, or stall.

Generally, flow separation is a difficult phenomenon to visualize or measure directly [38]. One common method for visualizing flow separation is tuft flow visualization, which provides an instantaneous, qualitative picture of the flow direction and behaviour over a surface. In the case of wind turbine blades, several digital image processing methods have been developed for converting qualitative tuft flow visualization video to quantitative stall measurements. In the following sections, an overview of the tuft flow visualization method will be presented, followed by a review of several specific tuft flow visualization studies that have had a strong influence on the current project.

2.3.1 Review of Tuft Flow Visualization

Tuft flow visualization is a flow visualization technique that consists of attaching tufts (*e.g.* string or yarn) to a surface immersed in a flow. The movement of the tufts is then recorded with a camera, and their behaviour and orientation in the captured images can be used as an indicator of flow direction and flow separation [33]. In the context of measuring stall formation on a wind turbine blade, tufts are attached to the suction side of the airfoil and distributed evenly along the length of the blade. The orientation of an individual tuft in an image can then be used to indicate whether the flow at that point was attached or separated at that moment in time. An example image of tufts on a wind turbine immersed in a flow is provided in Figure 2.14.

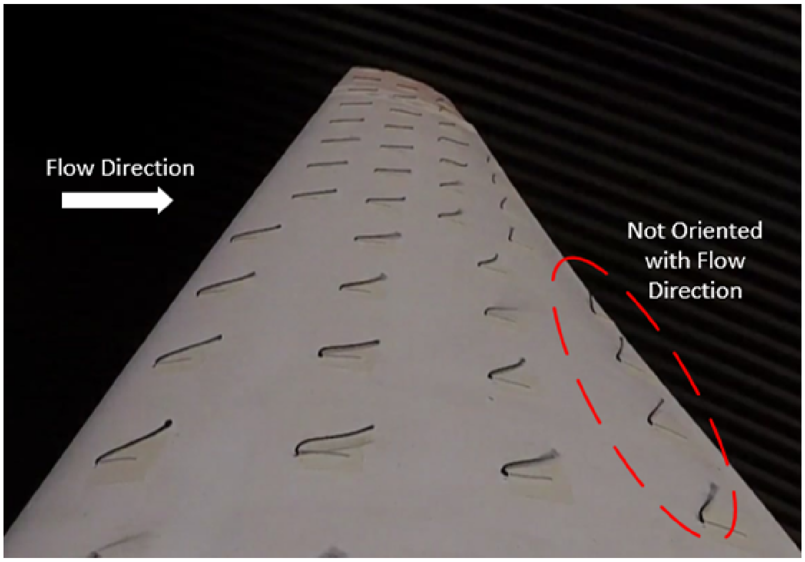

Figure 2.14: Image of surface tufts immersed in a flow

When reviewing images of tufts in a flow, tufts which appear aligned with the flow direction (*e.g.* left-to-right in Figure 2.14) indicate that the flow is attached at that location. In contrast, tufts that are not aligned with the flow, such as the circled tufts at the trailing edge of the blade in Figure 2.14, indicate that the flow is separated at that point, causing the tuft to oscillate rapidly in the wake. While there may be concern that the introduction of tufts to a surface would cause variations to the flow resulting in error, it has been shown in the literature that the location of the separation line with tufts is within 5% of the natural separation point [34].

More information than just the flow direction and separation can be inferred from the behaviour of tufts on the surface. The further potential of the method will be discussed in Section 2.3.2.

2.3.2 Use of Tuft Flow Visualization in the Literature

Given the simplicity and practicality of tuft flow visualization, it has been used frequently in early studies as a method of assessing stall over a rotating wind turbine blade. Eggleston and Starcher [35] conducted tuft flow visualization experiments using three downwind, fixed-pitch wind turbines: the Enertech 21-5, the Enertech 44-50, and the Carter 25. The use of multiple wind turbines allowed for observation of how stall formation can be affected by the design of the wind turbine blade. For example, the Enertech turbines were equipped with blades that had a variable chord and very little twist, and both turbines were found to experience stall beginning at the root, resulting in a triangular-shaped region of attached flow from the tip of the blade to a vertex on the leading edge [35]. In contrast, the Carter 25 turbine was equipped with a twisted, more aerodynamic blade, which caused trailing-edge separation near the middle of the blade which extended outwards towards the root as the wind speed increased [35].

Other studies, such as Haans *et al.* [6] and Maeda and Kawabuchi [21], involved the use of tuft flow visualization to assess the variation in stall formation as a function of the yaw-offset angle. Haans *et al.* conducted tests with a two-bladed micro-scale wind turbine in an open-jet wind tunnel with a yaw-offset angle of 45°. Results showed that, at this yaw position, the fraction of tufts indicating stall increased when the blade was in the 12 o'clock position, reaching maximum stall at an azimuthal position of 210° (where 0° is the 6 o'clock position). Similarly, tests by Maeda and Kawabuchi [21] showed an increase in the amount of stall on the wind turbine blade at the upper part of the rotation, just after the 12 o'clock position. With the wind turbine yawed, these positions correspond to the wind turbine blade rotating away from the wind.

While these studies have found useful qualitative data related to stall formation on a wind turbine blade, they (and other tuft flow visualization studies in the literature) share several common problems. For example, the authors of each of the cited studies analyzed the images of tufts manually, which opens the analysis to the possibility of inconsistent judgement, human error, and subjective results. Published tuft flow visualization studies also tend to have unclear criteria for what orientation or behaviour is considered stalled, which again reduces confidence in the consistency of the results. Finally, analyzing tuft images manually greatly limits the amount of data which can be practically analyzed by the researchers, which reduces the statistical significance of the results, limits studies to qualitative measurements rather than quantitative measurements, and also limits the amount of test cases which can be practically analyzed.

These common problems in tuft flow visualization studies have been addressed independently by two research groups via the development of digital image processing algorithms which can be used to automatically analyze tuft images and assess the stall on the blade. These algorithms will be reviewed in detail in the following sections.

Swytink-Binnema and Johnson Digital Image Processing Algorithm

Swytink-Binnema and Johnson [36] conducted a tuft flow visualization study using a 10 m diameter two-bladed 30 kW wind turbine installed on an outdoor site just outside of Waterloo. The turbine had a passive-yaw, stall-regulated design, and was equipped with turbine blades that had a constant 3° pitch and rotated at a fixed speed of 120 rpm. Approximately 100 tufts were secured to the suction side of one of the wind turbine blades, spaced 12 cm apart along the span and 6 cm to 8 cm apart along the chord line, depending on the space available. A wireless HD GoPro HERO2 [37] camera was mounted to the suction side of the blade, near the root, and was tilted to centre the tufted portion of the blade in the image. This orientation allowed for 1080 x 1920 pixel video of the tufts movement to be recorded at a rate of 30 Hz throughout the blade rotation, with all camera functions controlled via a wireless controller. Two 3.5 hour videos were recorded for testing, with wind speeds ranging from 11.7 m/s to 13.6 m/s. Each period resulted in approximately 375,000 frames of tuft video for analysis.

To analyze such a large quantity of data, a digital image processing algorithm was developed which could calculate the amount of stall present on the blade in each frame using simple, consistent criteria. More details on the algorithm can be found in Swytink-Binnema and Johnson [36] and Swytink-Binnema [38]. The software analyzed each frame individually and calculated the fraction of tufts in the image that were stalled, defined as the stall fraction, ζ, given in equation (2.48):

$$\zeta = \frac{N_s}{N_t} \tag{2.48}$$

where N_s is the number of tufts in the image flagged as stalled and N_t is the total number of tufts in the image. The algorithm calculated the stall fraction using three primary processes: foreground extraction, tuft location, and the flagging of tufts indicative of stall [36].

The first step of the algorithm was to extract the foreground from the image, such that only a black and white image of the tufts remained. Conversion of the original image to only tuft data itself required three input images: the original blade image, a cutout of the blade to mask the background, and the location of the tuft anchor points. An example of each of these inputs is demonstrated in Figure 2.15. Here, (a) is the original input image,

(b) is a background mask used to remove the background of the frame, and (c) is the anchor points of the tufts on the blade.

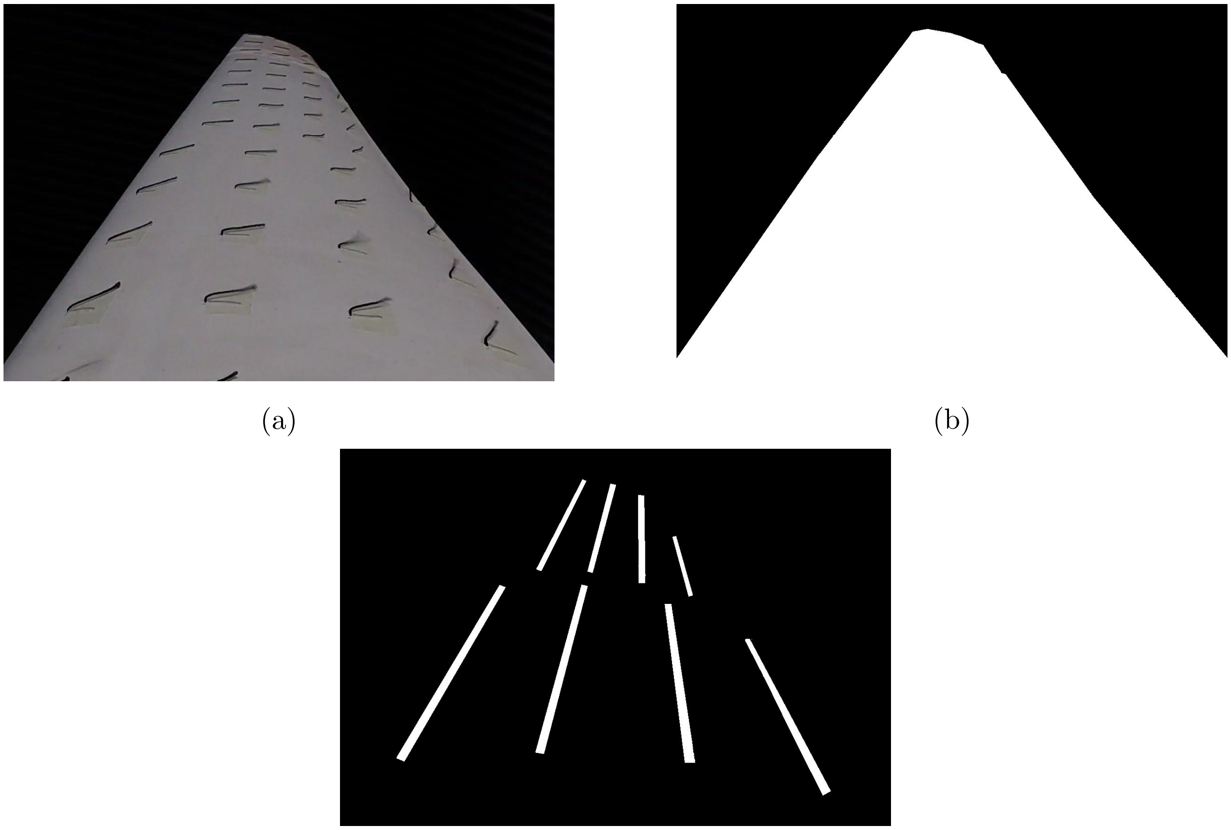
(a)

(b)

(c)

Figure 2.15: Input images for the Swytink-Binnema and Johnson [36] algorithm, including (a) the original frame, (b) the background mask and (c) the tuft anchor points

By applying the mask image shown in Figure 2.15b to the original frame, the background scenery could be effectively removed from the frame. The image was then converted to black and white, and all black objects connected to the edge of the blade image were removed. This left a completely white background with only the tufts remaining as black "blobs."

To accommodate for bending or vibration of the blade in the flow, eight masks were created for eight optimized blade flex locations, ranging from mask $N = 1$ for a nearly straight blade to $N = 8$ when the blade was flexed approximately 15 cm out of the rotor plane. Eight corresponding tuft anchor images were also created to account for the movement of the tufts with the blade [36].

After converting the image to a series of black blobs on a white background, the Swytink-Binnema and Johnson [36] algorithm distinguished which blobs could be informative tufts. The first step in this process was to remove any object that did not have an extremity anchored to one of the tuft anchor lines shown in Figure 2.15c. Next, objects were evaluated to remove any which were too large or too small to be interpreted as a single tuft. For this, Swytink-Binnema and Johnson [36] used an acceptable size range of 8 pixels to 150 pixels, which acounts for the changing distance of tufts relative to the camera along the span of the blade. Any remaining objects in the image were then approximated as ellipses with the same centroid and second moments of area as the original blob. The final criteria for an object to be considered a tuft would then be that the eccentricity, e, of the ellipse replacing the object be less than 0.8. If the eccentricity were larger, the object was considered too round to accurately provide the algorithm with a tuft orientation. The eccentricity of the ellipses was calculated using equation (2.49):

$$e = \sqrt{1 - \frac{b_2^2}{b_1^2}} \tag{2.49}$$

where b_2 and b_2 are the minimum and maximum radii of the ellipse, respectively.

After filtering for location, size and eccentricity, all remaining objects in the image were considered to be tufts. If fewer than $n_{min} = 35$ tufts were identified, the nearest neighbouring flex position N was selected, and the previous steps in the algorithm were repeated. The flex position would be incrementally increased and decreased from the starting position until a position where $n \geq n_{min}$ was found [36]. For example, the algorithm may start at position $N = 4$, then cycle through $N = 3$, $N = 5$, $N = 2$ before finding a sufficient match. The initial flex position for each frame was simply the successful position from the previous frame.

The orientation of the recognized tufts was used to assess the behaviour of the flow over the blade. Given a left-to-right flow, Swytink-Binnema and Johnson [36] assumed that the tufts should be oriented approximately to the right in attached flow and, accounting for the position of the camera relative to the blade, a criteria of less than 13° from the horizontal was set for tufts to be considered representative of attached flow. Any tufts with an angle greater than the threshold were flagged as stalled. To account for tufts which were oriented horizontally in the opposite direction, tufts were also considered stalled if their right extremity was on an anchor point while the left extremities were free. Finally, a stall fraction was calculated for each frame, which simplified the amount of stall on the blade down to one number. A flowchart summarizing the algorithm process taken from Swytink-Binnema and Johnson [36] is provided in Figure 2.16. An example output image from the algorithm with stalled tufts flagged as black is shown in Figure 2.17.

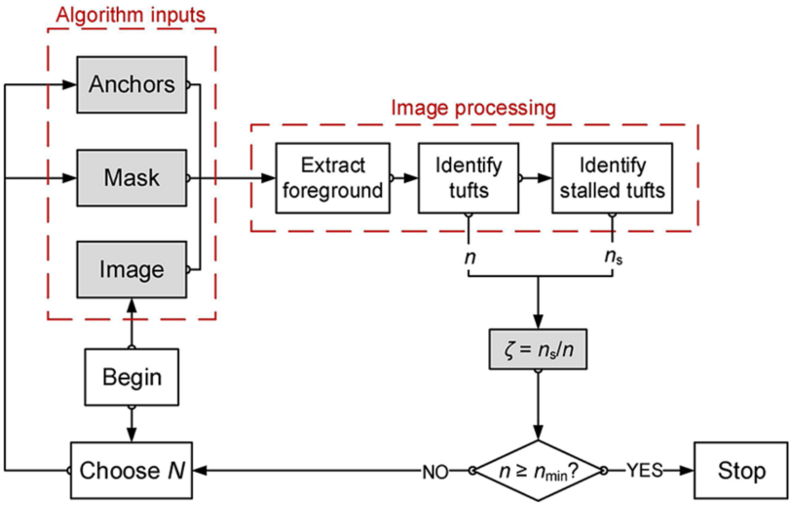

Figure 2.16: Flowchart summarizing the functionality of the Swytink-Binnema and Johnson [36] algorithm, taken from [36] with author's permission

As shown in Figure 2.17, the stall position on individual frames could be viewed by checking which tufts were flagged as stalled. In the case of Swytink-Binnema and Johnson [36], it was observed that stall on the 30 kW wind turbine blades occured primarily towards the root of the blade, with only the trailing edge showing signs of stall further outboard. This is a similar stall distribution as that found by Eggleston and Starcher [35] on the Enertech turbines, which were of a similar two-bladed, stall-regulated design.

Analyzing the average stall fraction data, results showed that the stall fraction increased as the wind speed increased [36], which is to be expected for a stall-regulated turbine while also considering the relationship between the wind speed, the angle of attack and stall formation reviewed in Section 2.1.2. An azimuthal variation in stall was also observed by sorting stall fraction data into 12 equal 30° azimuthal sections within ± 24°[36]. Stall was found to be at a maximum in the upper portion of the rotation, just after the blade passed the vertical position, similar to that observed by Haans *et al.* [6] during yaw conditions. It was concluded that the azimuthal variation was likely caused to vertical wind shear causing dynamic stall throughout the rotation or some effect of the unknown yaw angle [36].

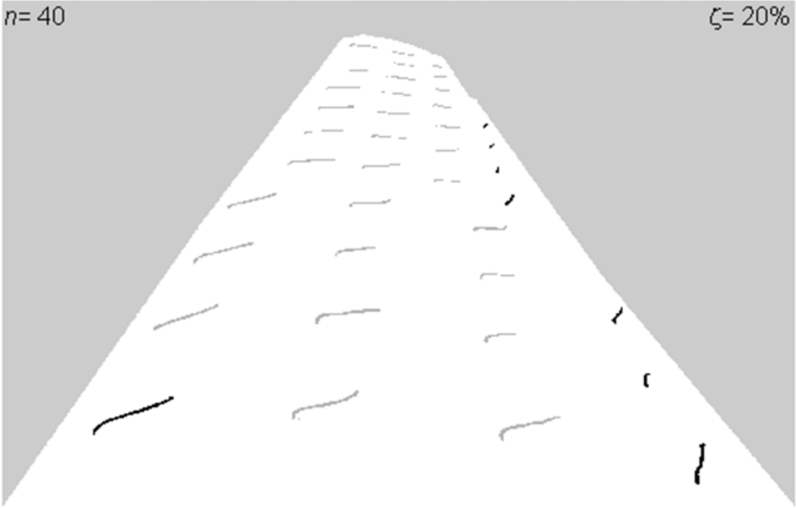

Figure 2.17: Example output of the Swytink-Binnema and Johnson [36] algorithm with stalled tufts highlighted in black.

While the algorithm is a great development and improvement on the manual tuft flow visualization analysis techniques of previous publications, several potential improvements have been identified. For example, the Swytink-Binnema and Johnson [36] algorithm uses a consistent stall threshold angle for all tufts over the blade. However, depending on the curvature of the airfoil or the distance from the camera, this may result in tufts which are aligned with the flow mistakenly being identified as stalled (*e.g.* the lower left tuft at the leading edge of the blade in Figure 2.17). Another issue is in the storage of stall data. In this algorithm, the only numerical data output for statistical analysis is the stall fraction in each frame, which is highly dependent on the number of tufts identified. The stall fraction also does not indicate where, on average, stall on the blade surface is occurring. Finally, the unknown yaw-offset angle and large uncertainty in the azimuthal position in the measurements makes the stall data difficult to interpret in this case, as not all of the influential variables have been quantified or controlled.

Vey *et al.* Method for Quantitative Tuft Flow Visualization

A second digital image processing algorithm for analyzing tuft flow visualization results was developed independently by Vey *et al.* [39] and used for a study published in 2014. The study was conducted at TU Berlin using an instrumented wind turbine blade known as the SMART BLADE GmbH, which was equipped with a traditional tuft flow visualization set-up. The wind turbine blade was installed on a wind turbine approximately 90 m in diameter in the 2 MW power range which was equipped with instrumentation for measuring wind speed, rpm, pitch, yaw, etc. Testing was conducted in the open environment over two days, with a total of 5000 images being captured by two cameras during the period.

Unlike the Swytink-Binnema and Johnson [36] technique, which utilized an HD camera mounted to the blade, the Vey *et al.* [39] method used ground mounted cameras to capture images of the tufts at specific blade positions during the turbine rotation. In the published paper, the results presented are those captured with one high resolution DSLR camera located 100 to 200 m downstream, which captured images of the descending blade at the horizontal position. Therefore, while the Swytink-Binnema and Johnson [36] study provided results throughout the full range of rotation, the Vey *et al.* [39] study provided a phase average of the tuft behaviour at one blade position.

However, while Vey *et al.* did acquire less information throughout the full turbine rotation relative to Swytink-Binnema and Johnson [36], their method did acquire more detailed and statistically significant information for the blade position that was examined. Quantitative flow data was acquired from the images by tracking the orientation of each individual tuft in each image, allowing for the calculation of per-tuft statistics. For example, Vey *et al.* [39] calculated the mean angle of each tuft on the blade and, using a line integral convolution, generated a high resolution image depicting where on the blade the flow is attached and separated, similar to an oil flow visualization image. This allowed for a qualitative and quantitative judgement of the location of the average separation line under particular flow conditions. An example output image of the Vey *et al.* method depicting the flow direction over the turbine blade, as well as the corresponding standard deviation, is provided in Figure 2.18.

Characteristics of the flow behaviour over the blade can be inferred from the flow map shown in Figure 2.18, but the flow can also be qualitatively analyzed by conducting a statistical analysis of individual tufts given their orientation in each frame. Vey *et al.* [39] plotted rose plots of tuft orientation, and used these to categorize particular tufts as being attached (*i.e.* aligned with the flow) or separated (*i.e.* not aligned with the flow). However, depending on the spread, or deviation about an average orientation, Vey *et al.* [39] were also able to infer the amount of turbulence particular tufts were experiencing at their particular azimuthal position. Bi-modality between attached and separated flow could be distinguished by tufts which appeared to have an even split between the being aligned with the flow and being caught in a turbulent crossflow. This provided much more insight into the tuft flow behaviour over the blade than has been possible in previous tuft flow visualization publications.

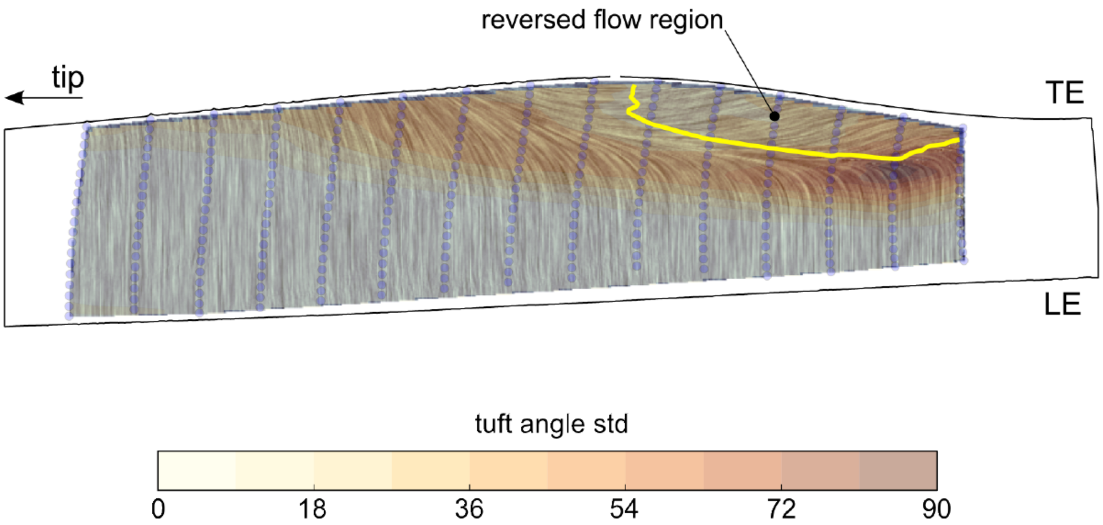

Figure 2.18: Example output of the Vey *et al.* [39] algorithm output depicting flow over the turbine blade. Reprinted from [39] with author's permission.

The results of the study showed stall forming primarily along the trailing edge inboard section of the blade [39], similar to the stall distribution found manually by Eggleston and Starcher [35] on the aerodynamic blade of the Carter 25 turbine. As expected, overall stall results showed that the amount of stall on the blade increased with wind speed, and the amount of turbulence present on the blade increased along the chord line.

While the Vey *et al.* [39] algorithm does have the advantage of providing per-tuft statistics from tuft flow visualization images, the requirement of having one high definition DSLR camera for each azimuthal location of interest greatly limits the amount of data that can be practically acquired throughout the wind turbine rotation. For example, measuring and observing the variation of stall with azimuthal location, as done by Swytink-Binnema and Johnson [36], would require dozens of tests with the camera position being constantly adjusted. This also limits the potential for measuring the variation with stall throughout the rotation in a constant flow field, and makes the cyclical variation in stall on a turbine blade operating at a yaw-offset difficult as well.

Chapter 3

Experimental Procedure

In this chapter, details of the experimental set-up will be presented for all of the test configurations used. To begin, descriptions of the Wind Generation Research Facility and Wind Energy Group test turbine used in all experiments are presented in Section 3.1 and 3.2, respectively. This is followed by a detailed overview of the five-hole probe measurement set-up in Section 3.3 before the experimental set-up for the tuft flow visualization measurements is presented in Section 3.4. Finally, an uncertainty analysis for the two project plans is presented in Section 3.5.

3.1 Wind Generation Research Facility

The University of Waterloo (UW) Fire Testing Research Facility, referred to here as the Wind Generation Research Facility, is located on the outer edge of the city of Waterloo, Ontario. The facility acts as a large-scale open circuit wind tunnel, using six 1.98 m diameter fans installed in the west wall of the building to generate constant-velocity winds. The fans are organized in a fan bank three across and two high, and are followed by a large plenum with limited flow conditioning provided by two settling screens and an array of flow-straightening ducts [41]. Summaries of the fan specifications and the facility geometry are provided in Tables 3.1 and 3.2, respectively. A photograph of the fan bank taken from inside of the facility is provided in Figure 3.1, including a scale to provide a sense of size. Note that Figure 3.1 only shows the section corresponding to the flow exit dimensions in Table 3.2; the expansion to the fan discharge plenum dimensions is not shown.

More details concerning the facility geometry and generated flowfield can be found in Devaud *et al.* [42], Gaunt [43] and Best [44]. Measurements by Gertz [11] in 2011

Table 3.1: UW Facility fan specifications [42].

Specification	Value	Details
Type	Vane axial fans	Howden-Buffalo Model 78-26 Series 1000 [42]
Size	1.98 m	Diameter
Number (arrangement)	6 (3 x 2)	-
Volume Flow Rate	78.7 m^3/s	Maximum per fan
Pressure	413.5 Pa	At maximum flow rate
Control	VFD	Individual operation

Table 3.2: UW Facility geometry specifications [42].

Area	Geometry Details
Fan discharge plenum	8.23 m long, 8.54 m wide, 5.9 m high
Plenum exit plane	Rectangular 8.0 m wide, 5.9 m high
Flow conditioning	Two settling screens and a 7 x 5 array of steel flow-straightening ducts in the discharge plenum
Test area	15.4 m wide, 19.5 m long, 7.8 m high along the sides and 13 m high at the peak
Flow exit	Squared, 7.9 m x 7.9 m

found that the facility is capable of generating wind speeds between 0 and 11.5 m/s with turbulence intensities in the range of 5.9% to 6.2%. The blockage ratio of the test turbine in the facility is approximately 7%, which is considered insignificant relative to blockage ratios common in closed wall wind tunnel testing [41]. The combination of high turbulence and low blockage is considered ideal for wind turbine testing, as it is representative of the environmental conditions that wind turbines would likely be exposed to in the field.

3.2 Wind Energy Group Test Turbine

The wind turbine used for all experiments in this project is a custom-built test rig designed and fabricated the Wind Energy Group and documented by Abdelrahman [10]. The turbine has an upwind horizontal-axis design, a hub height of 3 m, and is capable of supporting interchangeable rotors of three blades (or the like) depending on the desired test. A photograph of the test rig with blades developed by Gertz [11] installed is provided in

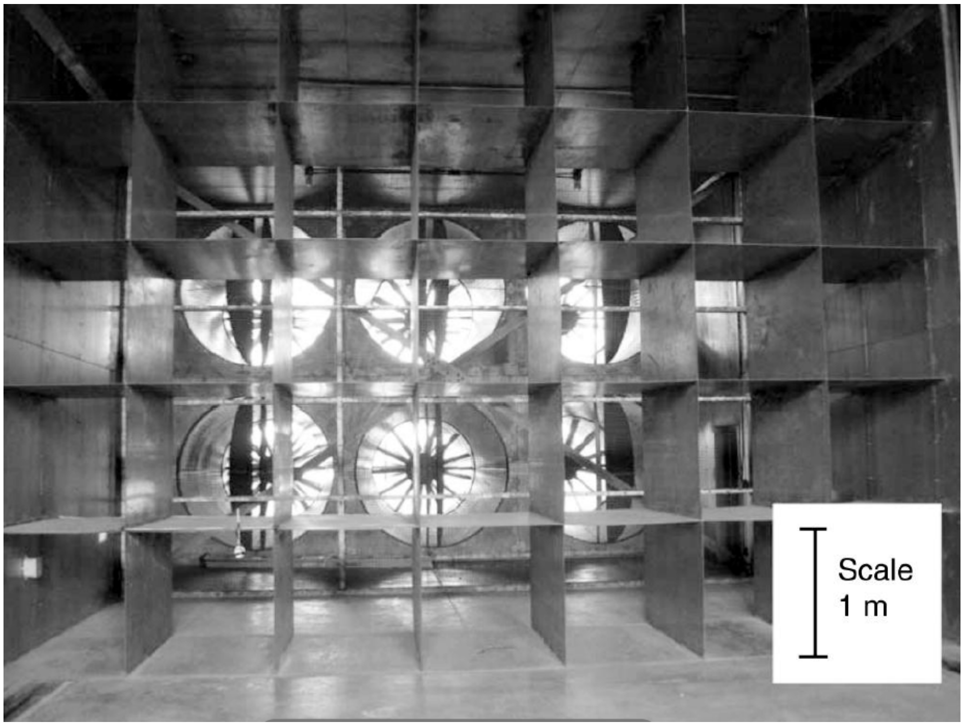

Figure 3.1: Photograph of Wind Generation Research Facility fan bank [10]

Figure 3.2. Details concerning the equipped blades, as well as their effect on the rotor operation will be discussed in Sections 3.3.1 and 3.4.1.

The wind turbine is equipped with a Marathon Electric Y287 184TC frame vector motor [45], which functions as both a motor and generator. This allows the turbine to produce power during live testing while maintaining control over the rotational speed of the turbine rotor at all times. The rotational speed of the motor is measured by an encoder which feeds back into an SP2203 Control Techniques Vector drive [46], a variable frequency drive which controls the speed of rotation. The drive is capable of communicating with the motor, the encoder and the brake to provide the user with complete control via a communications sub-panel in the control room [10]. Feedback from the brake, motor and encoder is presented on the control panel, allowing the user to view whether or not the brake is applied, as well as the current rotational speed and power output of the turbine. The feedback is then used by the SP2203 drive to adjust the control inputs to match the set values. A block diagram depicting the communication flow is provided in Figure 3.3.

The emergency brake is located between the motor and the gearbox and is used to lock

Figure 3.2: Photograph of the Wind Energy Group test turbine with Gertz [11] blades installed

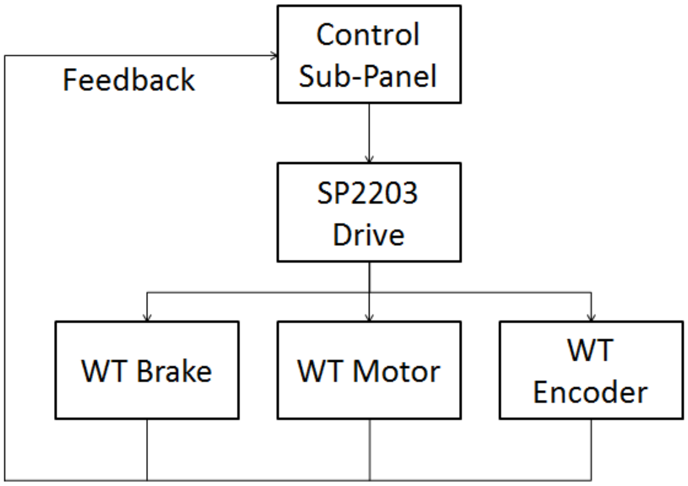

Figure 3.3: Block diagram depicting the test turbine control communication connections

the turbine in place when not in use as well as stop the turbine rotation in the event of an emergency. The brake is followed by a Nord helical in-line gearbox [47] used to reduce the shaft speed from the motor to the required operational range of the turbine rotor.

Between the rotor and the gearbox is a series of couplings and bearings, as well as a Futek Rotary Torque Sensor (Model TRS605) [48] which is mounted in-line with the main drive shaft. The torque sensor is a non-contact shaft to shaft sensor with a 200 Nm torque capacity, sized to meet the torque capacity requirements of the wind turbine [10]. The torque sensor is also equipped with a 1° resolution angular encoder, which is used in this project for tracking the angular position of the rotor and test blades.

A labeled photograph of the test rig drivetrain is provided in Figure 3.4, for reference. Not pictured is the wind turbine slip ring, which is mounted on the rotor shaft on the upwind side of the wind turbine. The slip ring was used to transmit signal data from a stationary wire connected to the hub of the turbine to the Arduino Uno [53] installed in the rotating wind turbine blade. The use of the slip ring in this project is described in Section 3.3.5.

3.3 Five-Hole Probe System

As discussed in Section 2.2.2, a five-hole pressure probe was developed and calibrated as described in [22] and [23]. This probe was used extensively through this project to measure

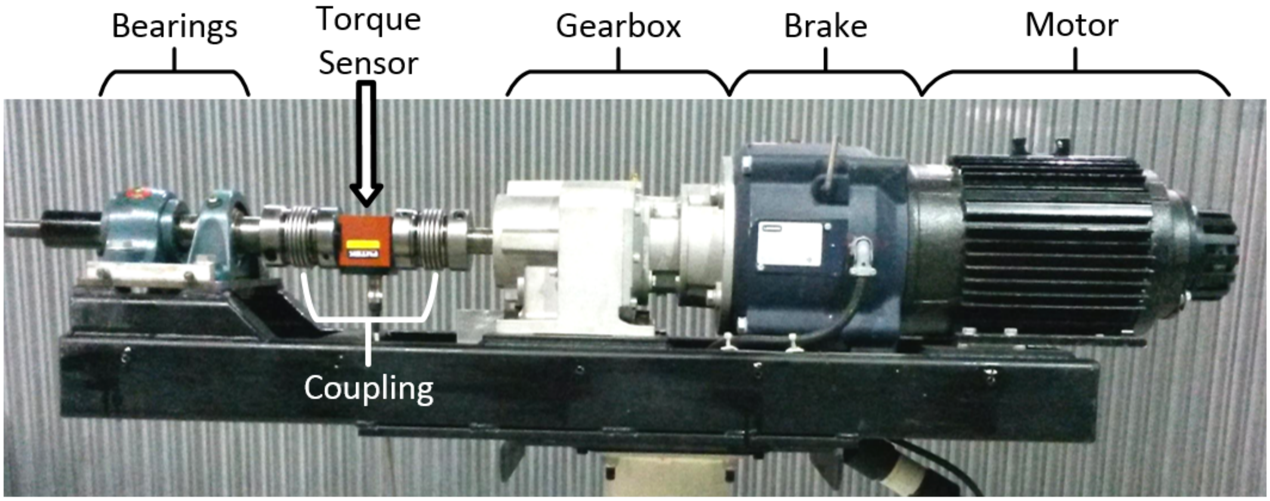

Figure 3.4: Labeled photograph of the Test Rig drivetrain

the flow angles at the leading edge of the blade as a function of the tip speed ratio, the radial location of the blade, the yaw angle of the turbine, and the azimuthal location. In this section, the test blade used for these experiments will be discussed in detail. Next, the data acquisition system installed in the blade for sampling pressure data will be presented. Finally, the test configurations used for the experiments will be discussed.

3.3.1 Test Blade

The five-hole pressure probe experiments were conducted using a test rotor designed and fabricated by the Wind Energy Group and reported in Abdelrahman [10]. The rotor consisted of one three-dimensional (3D) printed test blade, as well as two weighted rods which were used to balance the weight of the rotor. A photograph of the test rig with the Abdelrahman [10] blade installed is provided in Figure 3.5.

The 3D printed blade design is based on the NREL S833 [57] airfoil with a 1.7 m length. The design was developed iteratively using PROPID [9] software, resulting in a constant 178 mm chord and 6° pitch design for an optimal rotational speed of 200 rpm in an 8.5 m/s wind [10]. The blade was printed using PC-ABS plastic, and due to the size limitations of the printer, it was split into 5 main 285 mm long sections, plus one tip section. 3D printing was used because it allowed for a rapid, consistent and accurate manufacturing process, while also removing the need for a mold and allowing for a complicated internal design. An image of one of the blade sections is provided in Figure 3.6.

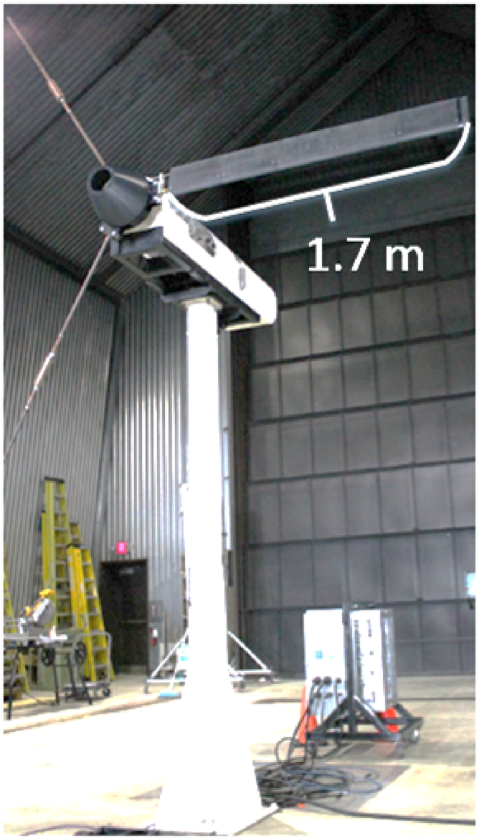

Figure 3.5: Photograph of the test rig with the Abdelrahman [10] blade installed

As can be seen at the edge of the airfoil section in Figure 3.6, the blade sections were each designed to be hollow. This provided savings for the cost and weight, but also weakened the structural integrity of the blade. To accommodate for the hollow design, as well as to provide a support to mount the blade sections to, a main tubular spar was inserted in the aerodynamic center of the blade. By having the blade sections attach to the tubular spar to form a complete blade, the design of the blade also became modular. That is, the order in which the blade sections were installed on the blade could be varied in order to test different configurations. This functionality was used throughout this project, as will be discussed in Section 3.3.6.

To accommodate the introduction of a five-hole pressure probe and corresponding data acquisition system into the blade, Moscardi and Johnson [22] prepared a new blade module which included an opening at the leading edge to support the probe. The redesigned blade

Figure 3.6: One of the five main 3D printed test blade sections

section also included a removable panel on the suction side of the airfoil, while the internal structure of the blade was changed to hollow out most of the space. The result is a blade section which can hold the data acquisition system inside as it rotates. The need for the data acquisition system, and its design, are discussed in the following section.

3.3.2 In-Blade Data Acquisition System

An innovative in-blade data acquisition (DAQ) system was used to sample pressures at the tip of the five-hole pressure probe. A portion of this set-up and experimental results were presented in Gallant and Johnson [50]. The DAQ used is the same used by Moscardi and Johnson [22] for the five-hole probe calibration, and consists of a compact design in order to fit within the hollow space of the 3D printed blade section. The electronics consist of the pressure transducers themselves, an analog to digital converter, a microcontroller, a wireless communication module, and a power supply. A photograph of the probe installed in the blade, and the DAQ components in the blade, is provided in Figure 3.7.

The five-hole pressure probe consists of five tightly packed stainless steel tubes arranged to form the shape of a cross. A diagram of the hole layout is provided in Figure 3.8. The upstream and downstream tubes are used to measured the pitch angle relative to the probe, and the root and tip probes are used to measure the spanwise flow angle relative to the probe. The four outer tubes are machined to form an angle of 45° between the tubes inlet and the axis of the probe [22]. Each tube has an exterior diameter of 1 mm, and extends approximately one chord length out from the leading edge of the blade. The probe is offset from the chord line of the blade by 15° to approximate the expected angle of attack at $r/R = 0.55$ at the design speed.

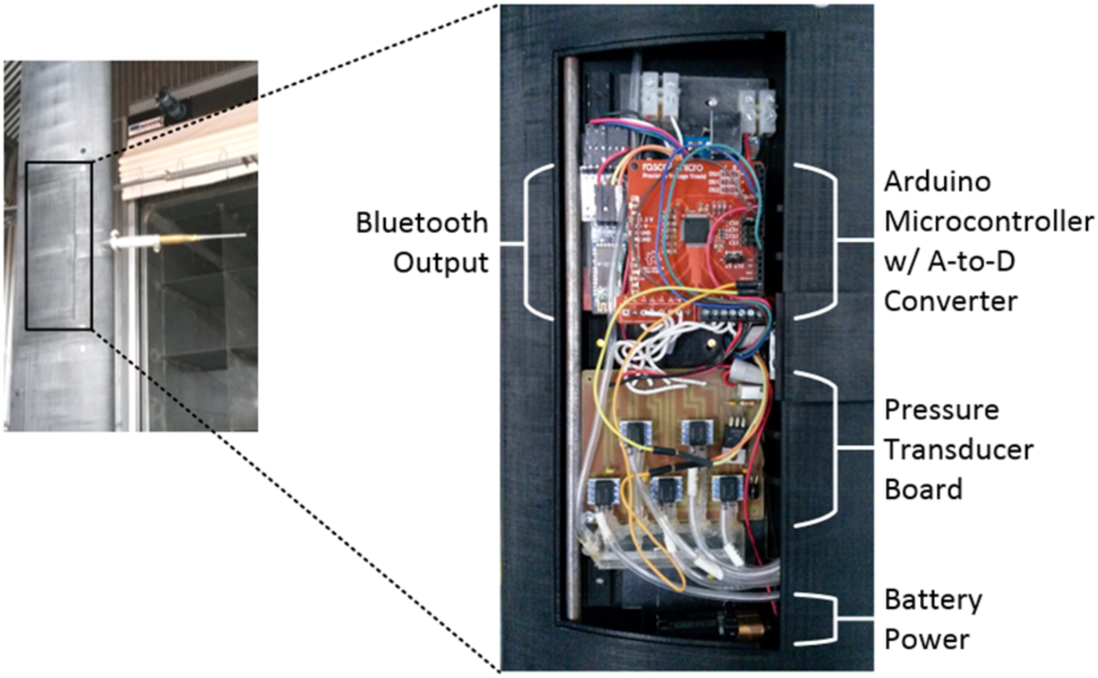

Figure 3.7: Photograph of the turbine blade with the probe attached (left) and of the DAQ system within the blade

Given the five-hole probe geometry relative to the wind turbine blade, this set-up would actually measure the local flow angle (LFA), rather than angle of attack. In this project, a correction was applied to convert the measured LFA to α data for analysis using induction factors modeled using PROPID [9] in combination with the Biot-Savart law, similar to the method used by NREL [18] as discussed in Section 2.2.2. More details on the PROPID [9] model and calculated axial induction factors is presented in Sections 2.1.5 and 4.1.3.

Each of the five tubes in the probe connects to its own pressure transducer mounted on the Pressure Transducer Board (PTB) via a plastic tube, pictured in Fig. 3.7. The pressure transducers used were Honeywell TruStability Board Mount Pressure Sensors [51], which are differential pressure transducers capable of measuring a pressure range of ±1245 Pa. In contrast, the expected maximum pressure that the transducers would experience at a radial location of $r/R = 0.55$ is approximately 400 Pa [22]. Each of the pressure transducers measured pressure at the tip of their respective tube relative to the pressure in a common reference pressure line. The common pressure line connected the transducers to the hub of the turbine where pressure was assumed to be essentially static. A similar

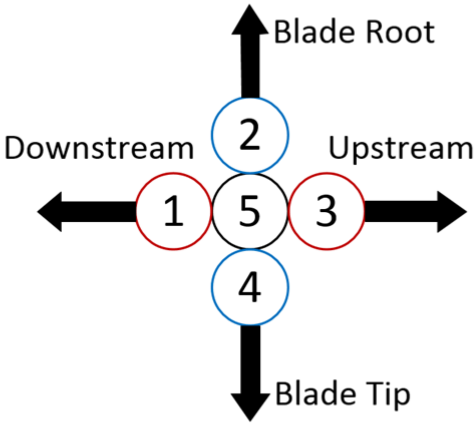

Figure 3.8: Diagram of the directional probe hole layout

approach was taken by NREL [16] during the Unsteady Aerodynamics Experiments, as discussed in Section 2.2.2.

The PTB also includes a potentiometer and voltage regulator to reduce power input from the battery power supply from 9 V to 5 V for the pressure transducers. A 9 V battery source was used to allow for the power source to be housed completely within the blade with the rest of the DAQ, while also providing enough power to operate all of the mounted components.

The pressure transducers on the PTB output their pressure readings as a voltage measured relative to the 5 V input. Their analog signal output was converted to a digital signal by an analog to digital converter (ADC) chip included on the Rascal Micro Precision Voltage Shield [52]. The ADC had a 16 bit resolution, and read 8 simultaneous bipolar channels, which was required for simultaneously reading the voltage input to the transducers and the five output voltages. Simultaneous reading was essential to the functionality of the five-hole probe, as the pressure distribution over the five tubes is more important than any individual reading.

In any pressure measurements conducted through tubing, the potential for dynamic effects or delays in the measurements should be addressed. Each of the pressure transducers is connected to a probe opening through a length of tubing ranging from 10 to 15 cm in length. Given the insignificance of dynamic pressure effects observed by NREL [17] in tubes less than 0.457 m as discussed in Section 2.2.2 and the similar set-up used here, no gain or phase corrections were implemented on the measured data. The short length of the tubing used is considered sufficient for mitigating this source of error. However, in the future, it is suggested that measurements be conducted to determine the time constant and response characteristics of the pressure transducers.

The Precision Voltage Shield [52] was mounted to a low-cost Arduino Uno microcontroller [53] which acted as the core of the DAQ. The Uno features 6 analog input pins, 14 digital I/O pins, and a compact size which made it well suited to this application. The Arduino Uno [53] was programmed to sample measurements from the pressure transducers converted to a digital signal by the Precision Voltage Shield via the digital I/O pins. The Uno would then parse this data and transmit data to the main data acquisition computer operating in the control room. The code (or sketch) used is presented in Appendix A, for reference.

Given the difficulty of performing wired communication from the Arduino Uno to the main computer during the wind turbine's operation, wireless communication was used. A Bluetooth output module was used to communicate serial data from the rotating wind turbine blade to the stationary computer in the control room. The high data transfer rate that Bluetooth provides was considered sufficient for communicating measurements with little delay [22].

3.3.3 Instrumentation and LabView Data Acquisition VI

During the five-hole pressure probe experiments, several independent variables were measured simultaneously to provide a complete picture of the turbine operation. These variables included the five-hole probe output, the shaft torque, the azimuthal position of the test blade, the upstream wind speed and air temperature. Because the encoder housed within the Futek Torque Sensor [48] only counted degrees of rotation with no set zero point, an phototransistor optical interrupter switch (H21A1) [55] and circuit board was mounted within the turbine nacelle to act as a permanent starting point. A metal tab was secured to the turbine shaft in line with the blade of interest such that, when the turbine blade was in the 0° (6 o'clock) position, the interrupter switch would be triggered. This trigger was used as the starting point for the encoder, allowing the azimuthal position to always be known relative to the 0° position.

To acquire the data from the measurement instruments simultaneously, LabView [56] VIs were created for each instrument individually, and the four were joined together in a primary VI. A flowchart summarizing the functionality of the primary VI is provided in Figure 3.9. As the flowchart depicts, when the VI is started, it first enters a loop in which it checks the output signal of the optical interrupter switch. When the switch is triggered, indicating that the blade is in the 0° azimuthal position, the encoder, pressure transducer, torque sensor and sonic anemometer sub-VIs all begin running simultaneously.

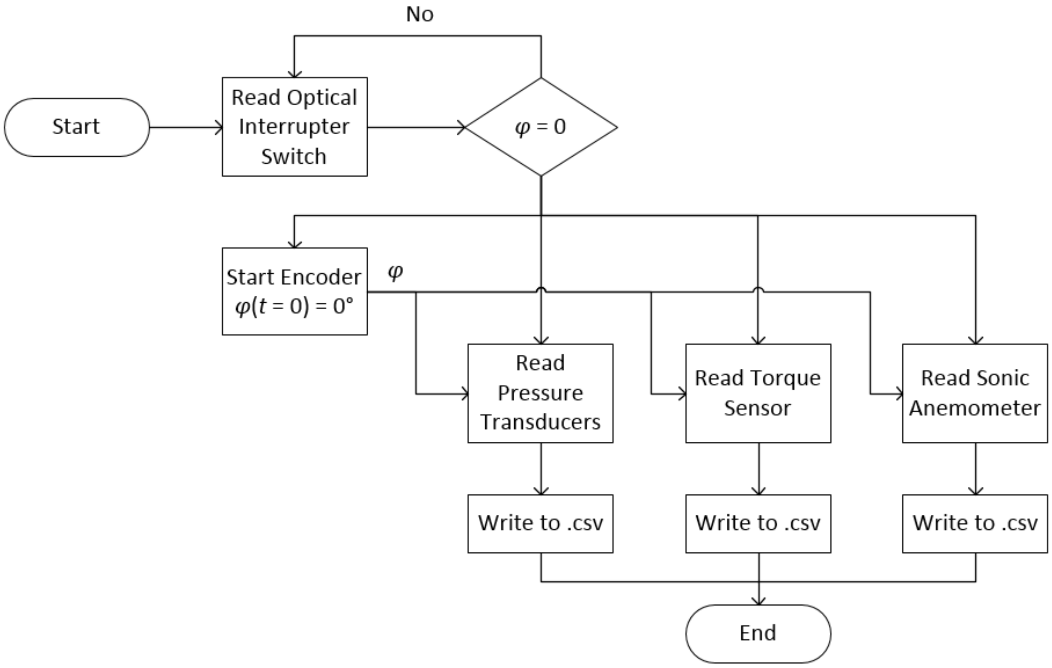

Figure 3.9: Flowchart summarizing the functionality of the primary LabView VI

At this point, azimuthal position measurements received from the encoder are also input into the other sub-VIs such that the blade position can be logged in tandem with all other measurements. Simultaneous position measurements are necessary for examining pressure or torque variations with azimuthal position. The relevant data is then recorded into separate Comma Separated Value (csv) files to accommodate the variation in sampling rates, and the program is ended at the command of the user.

The sampling rate of each instrument used was different based on its capabilities and the need for that variable. Shaft torque measurements were sampled from the Futek rotary torque sensor [48] at a rate of 720 Hz. Given the analog output signal, this was considered well within the sensors operational capabilities while also providing ample measurements for analysis. In contrast, the wind speed and temperature were measured by the CSAT3 [54] sonic anemometer at a frequency of 20 Hz, as the wind speed was expected to remain relatively constant throughout the tests in all cases. During the five-hole probe validation, discussed in Section 3.3.5, pressure measurements were sampled at specific azimuthal locations once per revolution. To increase the rate of data acquisition during the tests described in Section 3.3.6, the Arduino Uno [53] was programmed to sample as quickly as possible, with a 40 ms delay between each measurement.

3.3.4 Calibration of Pressure Transducers

The five-hole pressure probe used in this project was developed and calibrated by Moscardi and Johnson [22], as discussed in Section 2.2.2. However, this calibration was only done to relate pressure distributions over the five holes to various pitch and spanwise flow angles. The calibration of the individual pressure transducers was not conducted given the limited time available.

The first experiments conducted were therefore done to calibrate the five-hole probe and validate it's functionality while installed in the rotating wind turbine blade. Given the relatively low pressure capacity of the pressure transducers (± 1245 Pa), a small syringe filled with air was used to generate positive and negative pressures which were then applied to each individual transducer. Using a T-junction, tubing was simultaneously run to a small water manometer. A diagram depicting the calibration set-up is provided in Figure 3.10. Pressures were applied in increments of 10 mm of water from -60 mm to +60 mm, as read by the water manometer. At each measurement point, the voltage output by the transducer was recorded. It should be noted that the transducer calibrations were completed with the five-hole probe data acquisition system installed in the test blade. This was done to ensure that the temperature at calibration was similar to the temperature that would be experienced during testing.

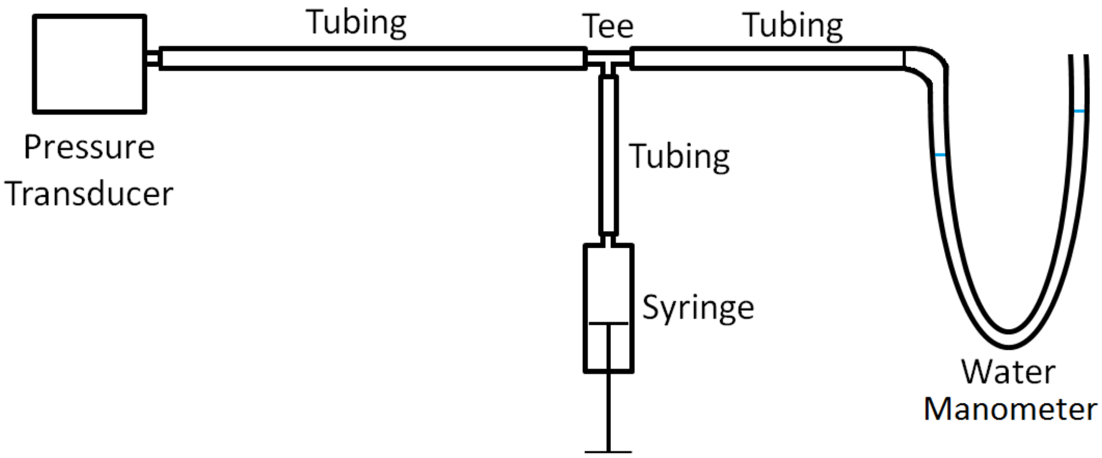

Figure 3.10: Diagram of pressure transducer calibration set-up using a syringe and water manometer (not to scale)

The result of the calibration is provided in Figure 3.11. The voltage output expected at each pressure is also plotted, and was calculated given the assumed linear relationship from the $P(V = 0 \text{ V})$ = -1245 Pa to $P(V = 5 \text{ V})$ = +1245 Pa, as established by the manufacturer [51].

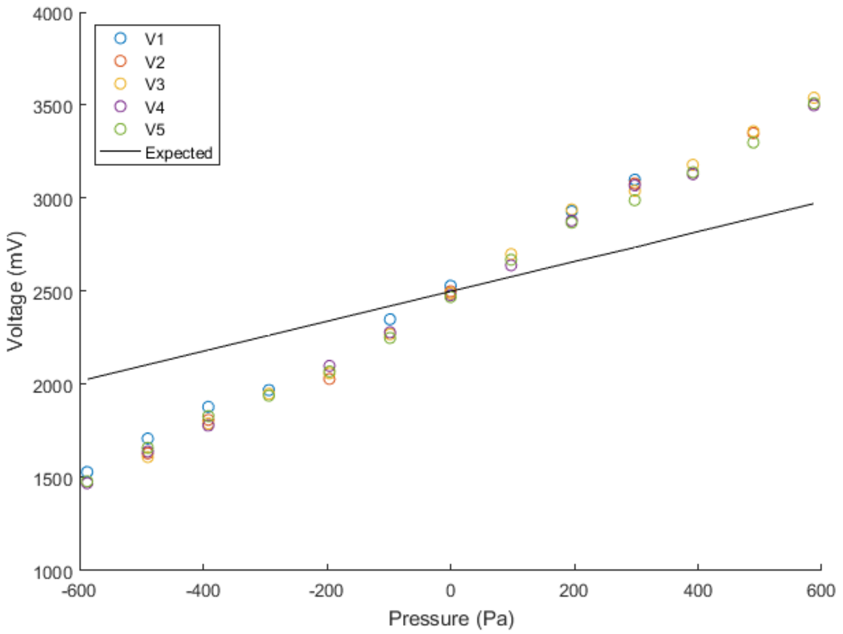

Figure 3.11: Plotted results of the board mounted pressure transducer calibrations

The calibration results plotted in Figure 3.11 show that the five transducers give a relatively consistent output at each pressure applied, indicating that no transducer is malfunctioning or providing an output significantly different than the others. The voltage output is approximately a linear function of the pressure applied for each transducer, which is to be expected given the manufacturer's specifications. However, the output curve measured is significantly steeper than the expected voltage, plotted in Figure 3.11 as a solid line. It is likely that this difference is caused by a difference in the environmental temperature during calibration. The cold temperature of the facility (ranging from -10°C to +5°C) would likely cause a change in the transducers' membrane properties, causing a change in the voltage output.

All measurements conducted for the five-hole experiments were done in the same temperature range. Therefore, the calibration data plotted for each pressure transducer was used to determine the true pressures at the probe inlet given the measured voltages. A line of best fit was approximated for each pressure transducer, and the resulting linear equations were used for converting voltage data to pressures. The resulting equations are presented in Appendix D.

3.3.5 Five-Hole Probe Validation

The measurement data being output from the five-hole probe was validated through a series of experiments in which the wind speed directly downstream of the five-hole probe was measured during wind turbine operation. The wind velocity measured by the five-hole probe (and by extension, the angle of attack), could then be compared to the wind speed measured at the same location. To measure the wind speed, the CSAT3 sonic anemometer [54] was used. The method used was inspired by the approach used by Johnson *et al.* in [41].

For these experiments, the five-hole probe was installed at a blade radius of $r/R = 0.55$, or roughly 0.935 m from the hub. The sonic anemometer was used to measure the wind speed approximately 10 cm downstream of the turbine blade, directly behind the five-hole probe. An image of the anemometer placed downstream of the blade is provided in Figure 3.12. Given the manual nature of moving the sonic anemometer to different azimuthal positions, measurements were made at 45° increments throughout the full blade rotation, beginning at 0°. Upstream wind speeds corresponding to the fan frequencies tested were acquired from Best [44].

As was described in the previous section, to match sonic anemometer measurements to those taken by the five-hole probe, pressure probe measurements were triggered by the LabView [56] VI to occur when the probe was passing the sonic anemometer. The trigger was transmitted via a wired connection from the control room, through the turbine slip ring, to the Arduino Uno [53], ensuring an almost instantaneous connection. The Arduino would then take a measurement sample from the pressure transducers and transmit the data back to LabView via the Bluetooth connection. The total time between the blade being in position and the Arduino Uno taking a measurement was measured to be at most 2 ms, which at a 200 rpm rotational speed corresponds to a delay of 2.5°.

Validation Test Configurations

Validation tests were conducted at three wind speeds, each with the wind turbine rotating at a constant 200 rpm. This was a conscious decision made to mimic the way operating wind turbines in the field function at a constant rpm, with only the wind speed affecting the tip speed ratio. The test configurations used are summarized in Table 3.3, and involve

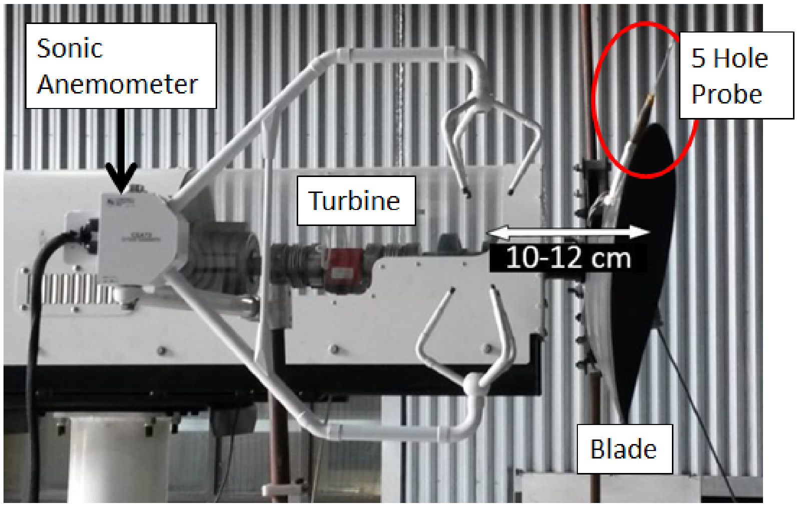

Figure 3.12: Photograph of the sonic anemometer placement downstream of the wind turbine blade

tests at $\lambda = 5.0$, 4.2, and 3.5. Tests were conducted for approximately 5-6 minutes at each azimuthal position, resulting to approximately 1000-1200 measurement points for the pressure probe and 6000-7000 measurement points for the sonic anemometer at each location.

Table 3.3: Summary of validation experiment test configurations

Test Case	Turbine RPM	Wind Velocity	Tip Speed Ratio	Fan Frequency
1	200	7.1 m/s	5.0	33.4 Hz
2	200	8.5 m/s	4.2	45 Hz
3	200	10.2 m/s	3.5	53.7 Hz

3.3.6 Test Configurations

After verifying the accuracy and functionality of the five-hole pressure probe and corresponding data acquisition system, the final five-hole probe experiments were conducted. The goal of these tests was to measure the wind turbine blade angle of attack and span-wise angle as a function of the tip speed ratio, radial location, yaw-offset position, and azimuthal position. The angle of attack measurements could then be compared to theoretical models reported by Burton *et al.* [2] and Morote [13], while also being used as an indicator of the upstream flow field as reported by Petersen *et al.* [30]. A secondary objective was to measure the shaft torque generated throughout all of these tests, as this could be used as an indicator of the performance of the blade as a function of the angle of attack.

Testing was conducted at tip speed ratios of $\lambda = 5.0$, 3.6, and 3.1, each with a rotational speed of 200 rpm. Tip speed ratios were adjusted following the validation tests due to the measured effects of temperature on the fan-generated wind speeds. Given the modular nature of the blade, the five-hole probe section could be moved to different radial locations. Experiments were conducted with the five-hole probe installed at $r/R = 0.38$, 0.55 and 0.72. With the probe installed at $r/R = 0.72$, tests were conducted with the yaw-offset ranging from -15° to +15° in 5° increments. However, after observing little incremental changes between the yaw-offset positions, the remaining radial locations were only tested at yaw positions of -15°, 0°, and +15°. The results measured for the intermediate yaw-offset positions are plotted in Appendix C. The yaw-angle sign convention used in this thesis is provided in Figure 3.13, in which the turbine is viewed from the top. The turbine blades rotate clockwise from the viewpoint of the upstream flow.

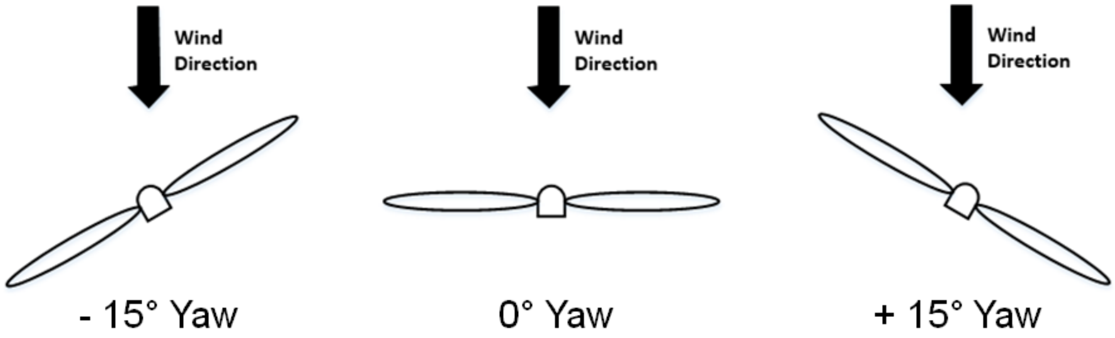

Figure 3.13: Diagram of the yaw angle conventions used throughout this thesis (turbine viewed from above)

As was mentioned in Section 3.3.3, the triggering method used during validation testing was abandoned in favour of sampling the transducers' output voltages as quickly as possible with a 40 ms delay after each reading. This increased the rate of data acquisition while also removing the issue of noise in the trigger signal which was observed in previous measurements. Torque measurements were recorded at a frequency of 720 Hz. The azimuthal location of each pressure and torque measurement was recorded simultaneously using the LabView VI structure discussed in Section 3.3.3.

Each test configuration was run for approximately 6 minutes, resulting in a minimum of 5400 pressure probe measurements each and over 100,000 torque measurements. These measurements were organized by azimuthal position into bins 10° in size, which allows for an analysis of the variation in flow angle and torque throughout the turbine rotation.

To account for the influence of the centrifugal forces on the pressure transducers installed in the blade (as referred to in Section 3.3.2), a test was conducted at each radial location with the pressure probe blocked such that the influence of the 200 rpm rotation on the transducers could be recorded. This influence was then subtracted from all other raw pressure data to ensure the only results observed were caused by inflow at the leading edge of the blade.

3.4 Tuft Flow Visualization System

After the five-hole probe measurements described in the previous section were completed, the Abdelrahman [10] rotor was removed from the test turbine and three aerodynamic test blades fabricated by Gertz [11] were installed for conducting tuft flow visualization experiments. Videos of tuft measurements could then be processed using a modified version of the Swytink-Binnema and Johnson [36] algorithm described in Section 2.3.2. In this section, details of the test blade and instrumentation used will be provided, followed by a discussion of the modifications made to the algorithm and the test configurations used for the experiments.

3.4.1 Test Blade

All tuft flow visualization experiments conducted were completed using wind turbine test blades designed and fabricated by Gertz [11]. These blades are 1.6 m in length and designed to operate at a rotational speed of 200 rpm in a 6.5 m/s wind, which gives a design tip speed ratio of $\lambda = 5.15$. The design of the blade was again developed iteratively using PROPID [9] software, and was based on the NREL S83x family of airfoils [57], which are appropriate for a wind turbine of this size. The NREL S833 was placed at the 75% radius, the S834 airfoil from 95% to the tip, and the S835 from the root to 40%. Between the defined airfoil sections, a linear blend of the airfoil shapes was used for the blade design.

The blades were fabricated using fibre-reinforced plastic, and include removable maple wood tips to allow for testing with alternative winglet designs [11]. The blade geometry varied from a chord of approximately 200 mm and a twist of 19° at the root to a chord of 100 mm and twist of 0.5° at the tip [11]. Plots of the chord and twist distributions along the blade span are provided in Figures 3.14 and 3.15. A photograph of the test turbine with the Gertz blades installed was provided in Figure 3.2.

Another plot of interest from Gertz [11] is the predicted and measured performance of the test blades as a function of the tip speed ratio, as shown in Figure 3.16. The measured results (labeled "Standard tip average") peak at approximately $\lambda = 6.5$, which is slightly higher than the design speed of 5.15. As the tip speed ratio decreases then (which corresponds to an increasing U_∞ and an increasing α), the performance of the wind turbine blade decreases rapidly, reaching nearly one third of the peak C_p at $\lambda = 3$. This would indicate a significant increase in stall over the wind turbine blade, which may be confirmed in Section 4.2.1.

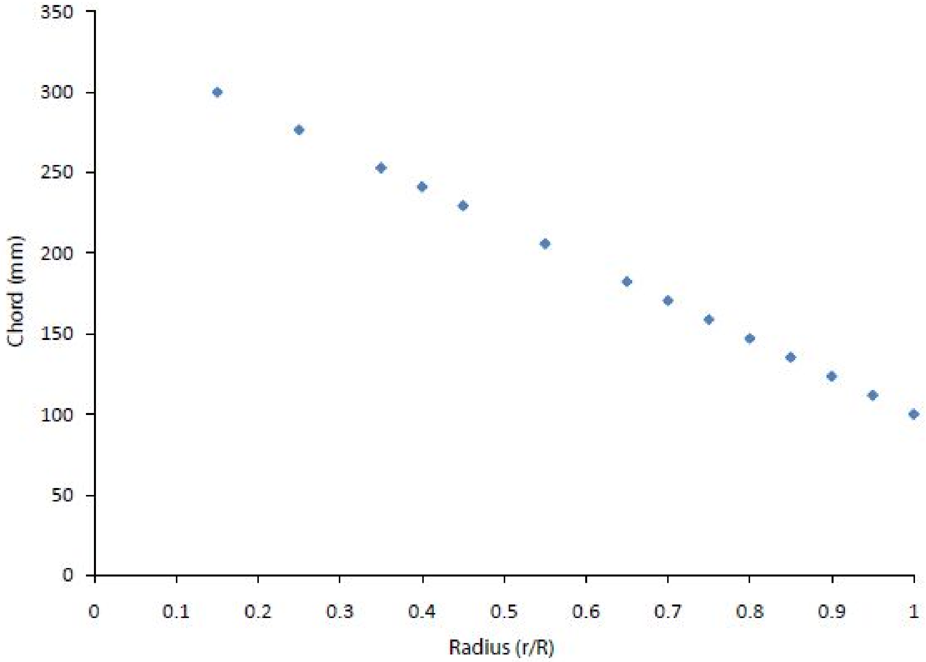

Figure 3.14: Chord distribution of the Gertz test blades, taken from [11] with author's permission

3.4.2 Instrumentation

The layout of tufts over the Gertz [11] blades was developed with the intention of visualizing as much of the flow over the blade surface as possible. First, preliminary testing of various

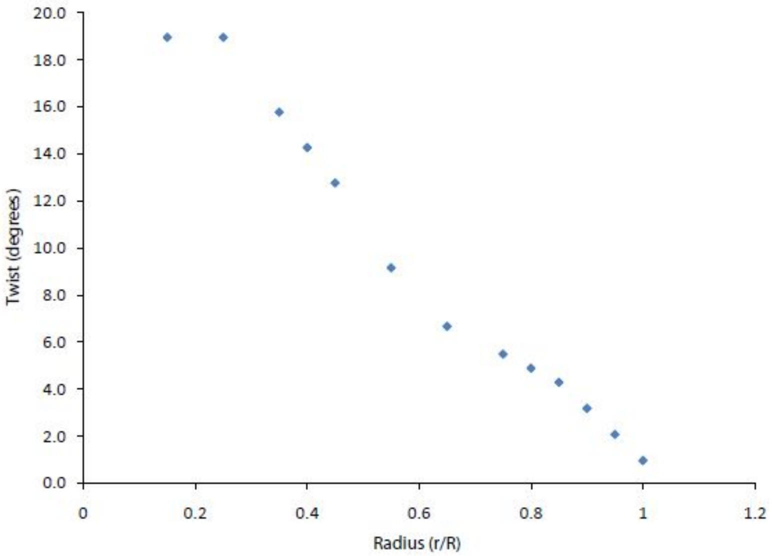

Figure 3.15: Twist distribution of the Gertz test blades, taken from [11] with author's permission

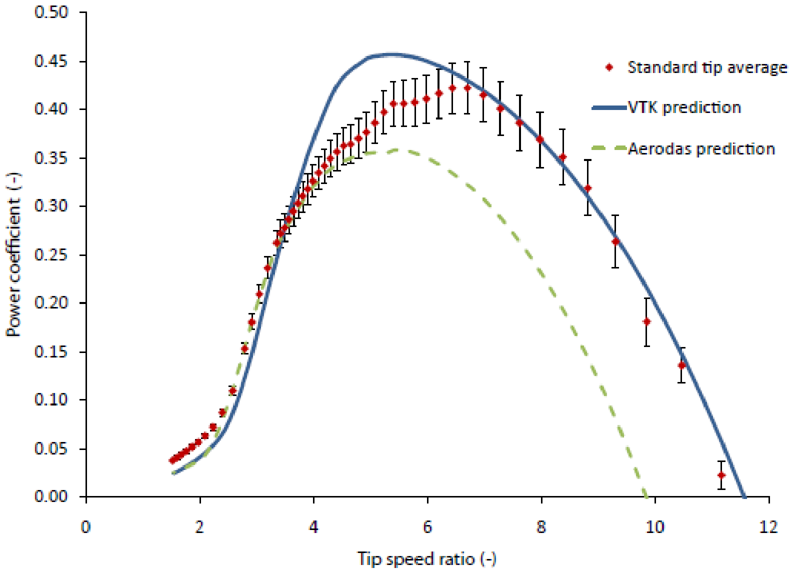

Figure 3.16: Measured Power Coefficient vs. Tip Speed Ratio for Gertz test blades, taken from [11] with author's permission

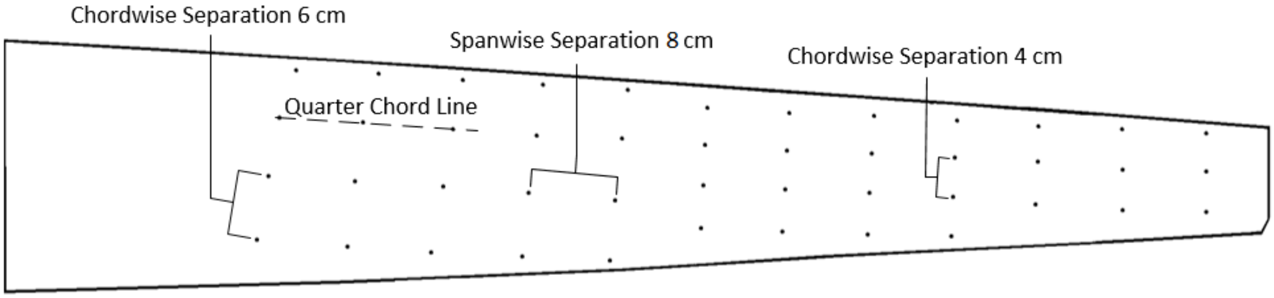

Figure 3.17: Dimensioned diagram of tuft layout on test blade

tuft materials and lengths was conducted at the University of Waterloo campus using an open circuit wind tunnel. The goal was to find a tuft length which was as short as possible and a material that would be flexible enough to accurately represent the flow. After reviewing the preliminary results, it was decided to use 3 cm lengths of cotton yarn approximately 1 mm in diameter for the experiment. Sections were cut and dipped in hot glue to prevent the ends from fraying.

45 tufts were distributed evenly on the blade surface using white masking tape, which was selected so that the tape would blend into the blade in the images. Tufts were attached to the blade following the pattern presented in Figure 3.17. The pattern was aligned parallel to the quarter chord line, with tufts spaced 8 cm apart in the span-wise direction and 4 to 6 cm apart in the chord-wise direction depending on the space available. This was done both to prevent tufts from becoming tangled with each other during testing as well as to prevent tufts from overlapping in the camera images given that individual tufts must be recognized for post-processing.

To record the tufts movement during testing, a GoPro Hero3 [58] HD camera was attached to the root of the blade using an adhesive mount, as shown in Figure 3.18. Video was recorded at 1080p resolution at 60 frames per second with a narrow setting activated on the camera to focus the video on the tufts. Note that all images of tufts on the wind turbine blade presented in this thesis were captured using the camera in the configuration shown.

Shaft torque generated by the wind turbine operation was again measured using the Futek rotary torque sensor [48], which was set to measure at a frequency of 360 Hz. The frequency was lowered after conducting the five-hole probe measurements, as the amount of data being accumulated was considered unnecessary, and the higher sample rate would occasionally lead to errors in the LabView VI [56]. Data acquisition from the encoder and torque sensor was controlled by the LabView VI [56] described in section 3.3.3.

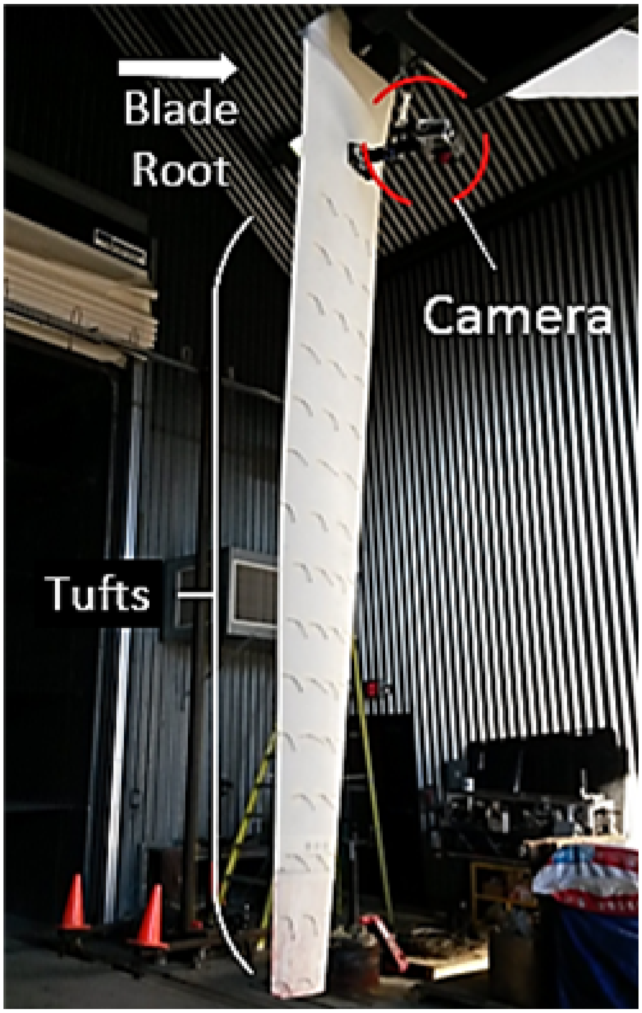

Figure 3.18: Photograph of camera and tufts attached to test blade

3.4.3 Modifications to Swytink-Binnema and Johnson Algorithm

The digital image processing algorithm used to process the video results in this project was a modified version of the Swytink-Binnema and Johnson [36] algorithm discussed in detail in Section 2.3.2. The primary goal of the modifications was to expand the functionality of the algorithm to allow for an analysis of per-tuft statistics similar to the functionality included in the Vey *et al.* [39] algorithm. This would include logging each of the tuft orientations for each individual frame, and organizing the data in such a way that the data pertaining to an individual tuft's movements throughout the test could be statistically analyzed. A secondary goal of the modifications was to individualize the stall criteria for the tufts over the blade to account for the effect of the curvature of the airfoil on the measured angle of tufts indicating attached flow.

To implement these changes, the anchors image files were modified to label anchor points for each individual tuft, rather than the anchor lines used in the original algorithm. An example of the original and updated anchor image formats is provided in Figure 3.19. MatLab [61] was used to label each anchor point in the updated image, from left to right, based on the centroid of each square. Eight versions of the updated anchor files were created to account for different flex positions, just as was done for the original anchor files. No changes were made to the mask format.

With the individual anchor points identified and labeled, the algorithm followed the same steps described in Swytink-Binnema and Johnson [36] as summarized in Figure 2.16 up to the identification of which blobs are recognized as tufts (*e.g.* which tufts have a left extremity on an anchor point). After tufts in the image were recognized, the function `sort_tufts` was called. The function cycled through each of the anchor points and tufts recognized and matched the two together based on the coordinates of the anchor areas and the tuft extremities. If the right extremity of a tuft was on an anchor point and the left extremity was free, the tuft was flagged as stalled just as in the original algorithm. The output of the `sort_tufts` function was matrix of the sorted tufts organized by their respective anchor points, as well as each tuft's orientation. To maintain a consistent matrix size between frames, anchor points which did not have a recognized tuft assigned to them were assigned a filler value of NaN to allow the anchor to be filtered out during analysis. A flow chart depicting the method used to assign tufts to anchor points is presented in 3.20. Note that, at this point in the overall program, the orientation of the individual tufts had already been calculated following the method presented by Swytink-Binnema and Johnson [36].

After the individual tufts were sorted into anchor points, they were each evaluated to determine which were representative of stall using the same series of checks described in

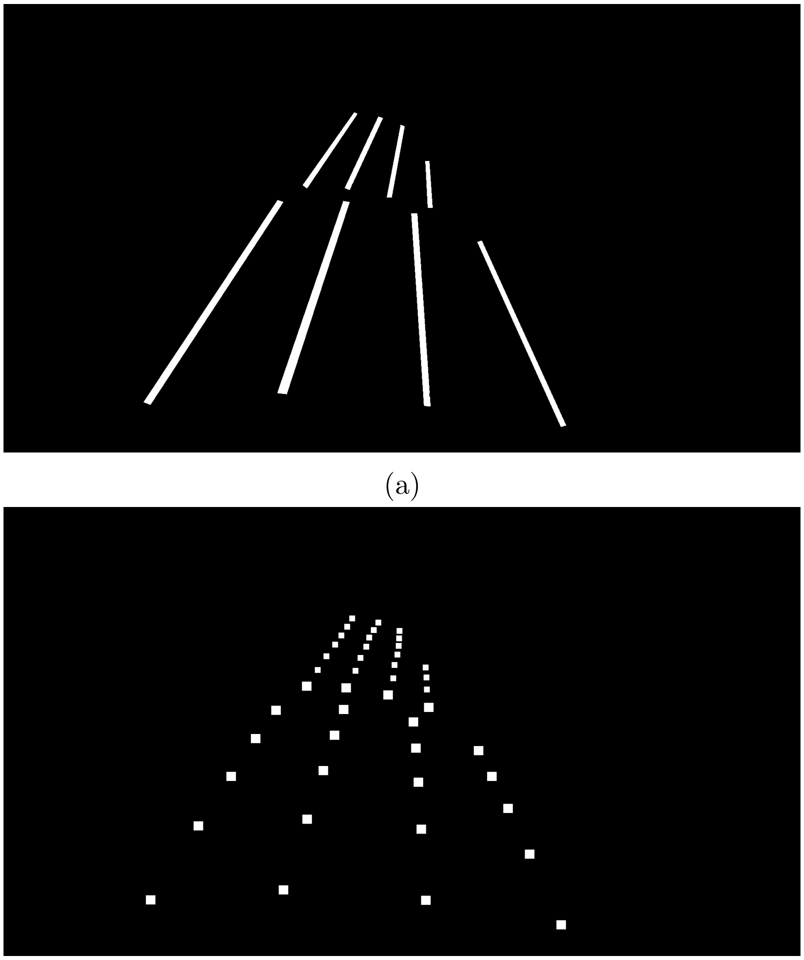

(a)

(b)

Figure 3.19: Example Images of the (a) Original and (b) Updated Anchor Point Formats
0

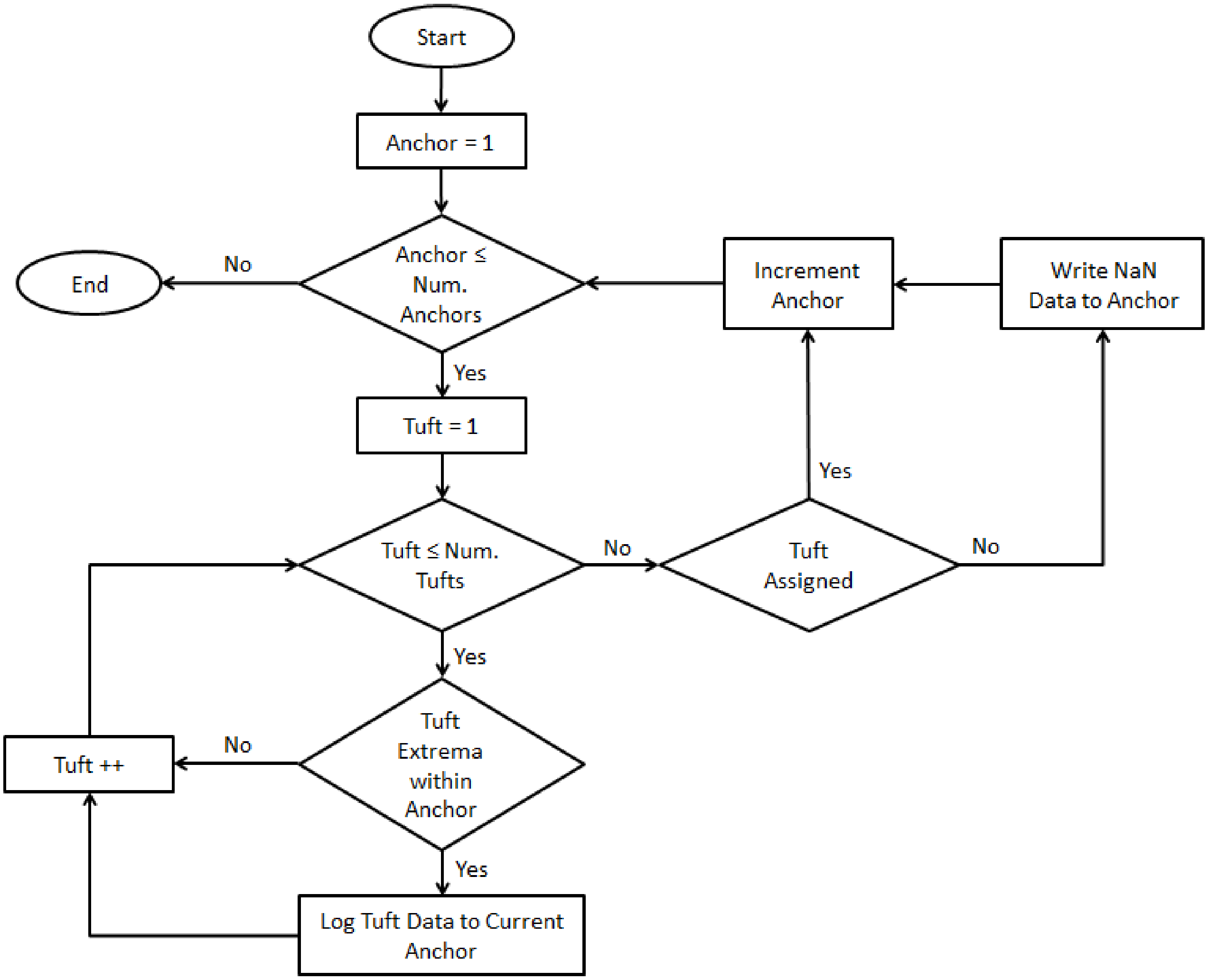

Figure 3.20: Flowchart depicting the `sort_tufts` function written to assign tufts to anchor points

Swytink-Binnema and Johnson [36]. The tuft orientations were evaluated against individualized criteria, which was manually coded based on an estimate of the angle of the airfoil surface at each tuft location with respect to the camera. All tufts were given a specific 20° window which would be indicative of attached flow (*i.e.* 10° from horizontal, ±10°). After checking each tuft, a matrix including each anchor point, the corresponding tuft orientation, and a boolean value indicating whether that tuft was stalled was output to the main function.

At this point, if less than 35 tufts were recognized in the frame, the algorithm would move to the next set of masks and anchor points following the same procedure established in Swytink-Binnema and Johnson [36]. When a suitable mask and anchor point combination was found, the algorithm stored the output matrix of tuft orientations and stall flags for that frame and repeated the process for the following frame in the video.

Because the modified algorithm was storing individual tuft orientations for each of the 18,000 frames being processed, the computational load was increased significantly relative to the original algorithm, in which only the stall fraction was saved. The updated algorithm also requires more manual input when preparing a new tuft layout, as the stall criteria for each individual tuft must be established. However, while these modifications do increase the processing time required for analyzing the video data, the increased accuracy in stall identification and increased potential for statistical analysis is considered to be well-worth the reduction in computational efficiency.

It should also be noted that, while the algorithm is calculating the orientation of each individual tuft on the blade, it is doing so from a two-dimensional image. This means that it cannot differentiate between a tuft orientation facing partially towards or partially away from the camera. This was considered acceptable for the current project, as tuft orientations both away or towards the camera are representative of flow separation and stall. However, a future iteration of this algorithm may be able to estimate the absolute orientation of tufts in an image via some form of calibration or calculation using the tuft length or geometry recognized.

3.4.4 Estimation of Azimuthal Position in Tuft Video

The GoPro Hero3 [58] camera used for recording tuft video was operated independently of the Data Acquisition LabView VI [56] described in section 3.3.3. Because of this, there was no direct way to determine what azimuthal position the wind turbine blade was oriented at in a given frame of tuft video. Initially, azimuthal position was recorded simultaneously with the corresponding timestamp using LabView [56] in order to synchronize video frames with the azimuthal position. Unfortunately, given the limited resolution of the current timestamp available with the consumer camera, this synchronization was found to be too imprecise to provide any accurate estimation of the blade position.

Instead, a method based on the azimuthal estimation technique described by Swytink-Binnema and Johnson [36] was used. A marker was placed on the floor below the turbine such that it would be in the video frame when the blade was oriented at $\psi = 0°$ (*i.e.* the 6 o'clock position). This marker, combined with the rails installed in the floor for the sonic anemometer tower, provided a clear visual indicator of the camera orientation once per rotation. Knowing that the camera frame rate was a constant 59.94 Hz and that the turbine rotated at approximately 200 rpm, it was calculated that the turbine blade rotated approximately 20° in each frame.

A Matlab script was written to calculate the blade orientation in each frame using this information. Tuft video was manually analyzed to identify frames roughly 30 seconds apart in which the blade was oriented at approximately 0°. The timestamp for these frames was then used to reset the azimuthal position calculation during the analysis to prevent any errors in the position estimation from propagating throughout the entire video. A value of 30 seconds was recommended by Swytink-Binnema and Johnson [36] after they found that a manual intervention every 60 seconds was insufficient for high accuracy.

To evaluate the effectiveness of the technique for estimating azimuthal position, 240 frames identified as being at approximately $\psi = 0°$ were manually checked. Given that each frame of video covers 20° of rotation, the best resolution achievable is approximately 10°. Frames were therefore sorted into four categories based on their accuracy: the frame identified was closer to 0° than the two adjacent frames (*i.e.* accurate to less than 10°); the frame identified was an equal distance from 0° as one of the adjacent frames (*i.e.* accurate to 10°); the frame identified was adjacent to a frame showing 0°; or the frame identified was more than one frame from 0°. A summary of the azimuthal position check results is provided in Table 3.4.

Table 3.4: Summary of Azimuthal Position Accuracy Checks.

No.	Proximity to $\psi = 0°$	Error magnitude	No. of Frames	
1	Nearest Frame	<10°	201	83.8%
2	±0.5 Frames	≈10°	35	14.6%
3	±1 Frame	<20°	3	1.3%
4	More than 1 Frame	>20°	1	0.4%
Total			240	100%

The results presented in Table 3.4 indicate that the azimuthal position of the blade in a given tuft video frame is less than 10° from the position indicated in 84% of the frames tested, and the position is within ±10° over 98% of the time. Relative to the Swytink-Binnema and Johnson [36] results in which nearly 30% of the frames could only be identified within ±24°, the use of manual intervention every 30 seconds and more consistent rotational speed of the test turbine are shown to result in a significant increase in the accuracy of the blade position estimation in the tuft video.

3.4.5 Test Configurations

Tuft flow visualization experiments were conducted using the test turbine, the Gertz [11] turbine blades, and the tuft layout and instrumentation described in the previous sections. The goal of these experiments was to evaluate the formation of stall and variations in flow direction over a rotating wind turbine blade as a function of the tip speed ratio, yaw-offset position and azimuthal position. While the results of these experiments were expected to provide interesting insight into the behaviour of flow over a full-scale wind turbine blade, the results of the experiments are also viewed as a demonstration of digital image processing for tuft flow visualization results, including the modifications made to the Swytink-Binnema and Johnson [36] algorithm to include functionality introduced by Vey *et al.* [39].

Tests were conducted at tip speed ratios of λ = 7.0, 5.15, 4.0 and 3.2, each with a rotational speed of 200 rpm. As was described previously, the design tip speed ratio of the Gertz [11] turbine blades is $\lambda = 5.15$, so the values chosen were selected to study flow speeds below and above this set point. Care was also taken to select test configurations which were originally conducted by Gertz [11] during the original testing of the blade to ensure that data was available for comparison. Tests were conducted at yaw-offset positions of 0°, +15° and -15°.

Torque and wind velocity measurements were acquired as described in Section 3.4.2. Tests were conducted for 5 minute lengths each, resulting in approximately 18,000 frames of data per test recorded at 60 fps. Given that 12 test configurations were completed, these experiments resulted in over 200,000 frames of data to be processed. Such a quantity of tuft video data would be impossible to process using conventional manual methods as used by Eggleston and Starcher [35] or Haans *et al.* [6], as described by Swytink-Binnema and Johnson [36].

3.5 Uncertainty Analysis

Estimating the experimental uncertainty is an essential part of acquiring and interpreting experimental data. When planning testing and instrumentation configurations that will be used, it can be helpful to assess what the expected uncertainty associated with each piece of equipment or sample rate and test length would be to identify any changes that should be made. In this section, the estimation of experimental uncertainty associated with the sonic anemometer, the torque sensor, the five-hole probe study and the tuft flow visualization set-up will be discussed. The methods established here were used during data analysis to develop the error bars that will be presented in Section 4.

3.5.1 Sonic Anemometer Uncertainty Analysis

The CSAT3 [54] sonic anemometer, like all instrumentation used, is subject to multiple types of errors. These errors include: the 0^{th} order uncertainty associated with the offset error of ± 8.0 cm/s and a resolution of 1 mm/s; the 1^{st} order uncertainty, which includes time varying effects that can be estimated using the precision error as shown in Equation (B.2); and N^{th} order uncertainty, which would include errors in the placement and orientation of the anemometer.

Combining the offset error and half of the least count resolution using the root-sum-square method, the bias uncertainty associated with the anemometer itself was found to be $u_{b,anem} = 0.08$ m/s. The bias uncertainty was then combined with the calculated precision error, again using the root-sum-square method. Given the high number of wind speed measurements, this total uncertainty tended to be dominated by the bias uncertainty.

While the orientation of the sonic anemometer is likely to be offset from the flow direction by as much as $\pm 5°$, the effect on the axial wind speed measured by the anemometer is expected to be negligible. The uncertainty presented will therefore consist solely of the bias and precision uncertainties associated with the instrument and measurements.

3.5.2 Torque Sensor Uncertainty Analysis

The Futek rotary torque sensor [48] has specified uncertainties associated with the zero balance, nonlinearity, hysteresis, and nonrepeatability for the torque measurement output, each given as a percentage of the rated output of 200 Nm. Combining these using the root-sum-square method [14] to find the total bias uncertainty results in $u_{b,torque} = \pm 2.00$

Nm. This is a significant value, as typical torque values measured in this thesis range from 5 to 25 Nm. Sample calculations for deriving this value are provided in Appendix B. Given the thousands of data samples recorded at frequencies ranging from 360 Hz to 720 Hz, the calculated precision uncertainty was found to be negligible when compared to the bias uncertainty. No errors associated with a misalignment of the torque sensor were observed.

The encoder contained with the torque sensor simply counts 360 pulses per revolution, and it was assumed that no errors occur given the simplicity and reliability of the device. However, the 0° position is defined by the optical interrupter switch and the interrupting tab secured to the rotating shaft. The tab was aligned to trigger the interrupter switch when the blade was oriented in the 6 o'clock position, and it was estimated that the error in this placement could be as high as 2°. Combining this bias error with half of the least count results in a total azimuthal uncertainty of ±2.06°. This uncertainty is not represented in the data plots for visual clarity, but it should be noted that it is present for all measurements other than the tuft video results, which will be discussed in Section 3.5.4

3.5.3 Five-Hole Probe Uncertainty Analysis

The uncertainty associated with the flow angle measurements conducted using the five-hole probe is a combination of several stages of uncertainty, beginning with the transducers themselves and propagating through the pressure measurements, interpolating through calibration data and finally through the NREL [16] equations that relate the flow angle measured by the probe to the angle relative to the blade. The estimation of the total uncertainty associated with the five-hole probe measurements is explained in detail in Appendix C.

To summarize the calculation, the bias uncertainty of the pressure transducers was first calculated to be ±3.65 Pa. This value is then combined with the estimated precision uncertainty for each pressure transducer to calculate a total uncertainty in the raw pressure measurements. This total uncertainty was then used to determine the uncertainty associated with the pressure coefficients, which was then directly correlated to an uncertainty in the flow angles using the same process described in Section 2.2.2 for regular five-hole probe use.

The uncertainty analysis showed that the bias uncertainty associated with the probe angle offset was the most significant contributor to uncertainty in the flow angles. For the angle of attack, this offset was estimated to be approximately ±0.1°. As will be shown in the results, this value approaches the total uncertainty associated with the angle of attack measurements.

3.5.4 Tuft Flow Visualization Uncertainty Analysis

In this section, uncertainty associated with the image processing algorithm and estimate of the stall fraction will be discussed. Uncertainty in the estimate of the azimuthal position for each frame of video was discussed earlier in Section 3.4.4, and it was established that the azimuthal uncertainty could be considered $u_\psi = \pm 10^\circ$ with 98% confidence.

Uncertainty in the calculation of the stall fraction for a frame of video data was previously discussed by Swytink-Binnema [38] during the initial creation of the image processing algorithm. The bias uncertainty of the stall fraction is a function of several factors including parallax caused by the camera orientation, errors in the stall criteria for specific tufts due to human judgement, or on rare occasions, a tuft being associated with the wrong anchor point. However, the most significant source of error is caused by tufts not being recognized by the algorithm, either because of lighting issues, the tuft appearing too blurred in the video to be viewed as a black object, or because the tuft was not located on an anchor point. This can become a significant problem at high tip speed ratios, when turbulence in the generated wind flow results in faster blade vibrations and, in turn, lower tuft recognition. When tufts are not recognized, whether they indicate stall or not, they reduce the value of N_t, as well as potentially N_s. As was established by Equation (2.48), this would bias the stall fraction towards a larger value than the true percentage. Swytink-Binnema [38] simplified the bias uncertainty associated with the stall fraction to:

$$b_\zeta = \left| \frac{\zeta}{n} b_n \right| \tag{3.1}$$

where b_ζ is the stall fraction bias uncertainty, and b_n is estimated by subtracting the total number of tufts on the blade from n for the individual frame. When tuft data were sorted into azimuthal position bins and averaged, the precision uncertainty was also calculated and combined with the bias uncertainty to find a complete estimate, which is indicated in the error bars presented in the results.

The expansion of the digital image processing algorithm discussed in Section 3.4.3 also requires an estimate of uncertainty for the orientation of each individual tuft measured. This data is currently only used to calculate the average tuft orientations as a function of the azimuthal position, and the orientation calculated by MatLab [61] is considered accurate. Neglecting parallax effects, the uncertainty is therefore dominated by the precision error. Tuft flow visualization uncertainty results are presented and discussed further in Section 4.2.

Chapter 4

Results

In this chapter, the results of the experiments described in Chapter 3 will be presented. The chapter has been divided into two sections. The first section focuses on the results of the five-hole pressure probe experiments. This includes: the probe validation experiments; the angle of attack measurements and comparisons to models; the characterization of the upstream flow speed; and finally an overview of the corresponding span-wise flow angle and torque measurements. The second section focuses on the tuft flow visualization study, including the presentation of stall fraction measurements and the comparison of these results to five-hole probe measurements. Averaged and interpolated tuft flow visualization results which provide maps of the flow over the turbine blade at different azimuthal locations are also presented.

4.1 Five-Hole Probe Results

4.1.1 Five-Hole Probe Validation Results

The functionality of the five-hole probe was verified by conducting flow field measurements throughout the blade rotation using the five-hole probe and the CSAT3 [54] sonic anemometer simultaneously, as described in Section 3.3.5. Pressure distribution data over the five holes was used to calculate the angle of attack, α at the leading edge of the blade. Then, knowing that the rotational speed of the blade was a nominal 200 rpm, the velocity relationships defined in Figure 2.6 were used to calculate the axial wind velocity at the rotor plane, $U_\infty(1-a)$. Because the experiments were conducted with a low-induction, single-blade rotor, it was assumed that the tangential induction factor, *a'*, was negligible. The same axial velocity was measured using the sonic anemometer, which was placed just downstream of the wind turbine rotor. The independent measurements of axial wind velocity at the rotor plane are presented in Figure 4.1. Note here that only the axial component of the measured flow speed is presented.

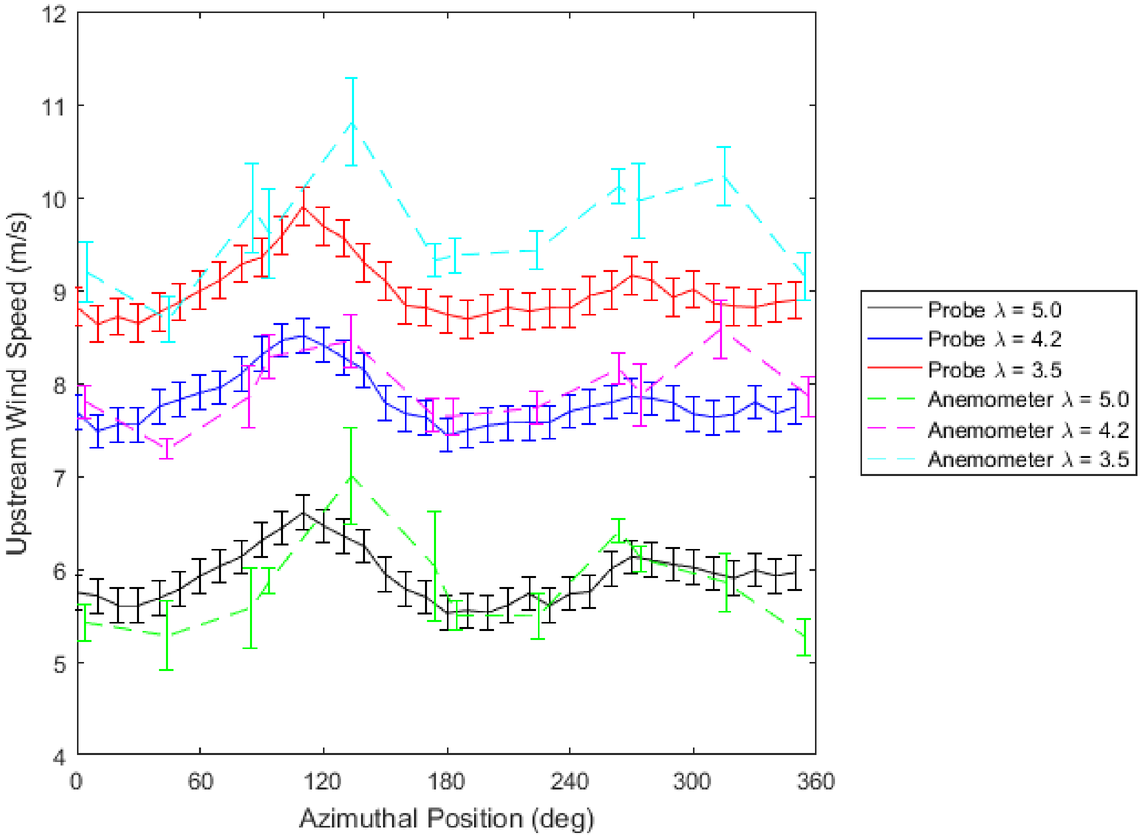

Figure 4.1: Experimental measurements of the axial wind velocity at the rotor plane using the five-hole probe and sonic anemometer. Lines between measured points are for reference only.

The wind velocity measurements plotted in Figure 4.1 show close agreement between the sonic anemometer and five-hole probe results, especially at tip speed ratios of $\lambda = 5.0$ and 4.2. At the highest wind speed, or $\lambda = 3.5$, the axial wind velocity measured by the sonic anemometer is approximately 1 m/s to 2 m/s greater than the velocity measured simultaneously using the five-hole probe. Variations between the five-hole probe and sonic anemometer measurements may be due to the number of data points recorded. However, the relative similarity of the curves at $\lambda = 3.1$, and the almost identical anemometer and probe measurements at the lower wind speeds, provide suitable confidence in the functionality of the five-hole pressure probe, the in-blade data acquisition system and the calibration.

It is notable that the uncertainty associated with the sonic anemometer measurements varies between points, with some of the error bars being significantly larger than those associated with the five-hole probe measurements. This is due to the slow sampling speed of the anemometer relative to the rotational speed of the wind turbine. During the validation testing, only wind speed measurements sampled when the blade was passing in front of the sonic anemometer were counted. Given the measurement frequency of 20 Hz and the rotational frequency of approximately 3.33 Hz, some tests resulted in a lower number of samples than others. The reduced number of measurements then resulted in an higher precision uncertainty. Despite this variation, the measurements and uncertainty presented here are considered sufficient for validating the functionality and accuracy of the five-hole probe and in-blade data acquisition system.

During these experiments, it was also noted that the wind velocity measured by both instruments appears to increase by 1 to 2 m/s between azimuthal positions of about 100° to 175°, which corresponds to the 10 to 12 o'clock positions of blade rotation (from upstream). Upon review of previous experiments in the facility, it was found that the same non-uniformity in the flow was also observed by Devaud *et al.* [42] and Best [44]. Weisinger [59] posited that the increased flow speed was caused by the flow output of the top-center and top-north fans combining to form a flow jet. To mitigate this issue in the rest of the experiments, an extra square meter of meshing was added to the flow straighteners at the appropriate location to reduce the magnitude of the jet. While this was found to not completely solve the problem, the magnitude of the jet was noticeable decreased in the following tests.

4.1.2 Angle of Attack Measurements

With the pressure transducers calibrated for operation in the test environment, and the functionality of all of the measurement systems validated, full-scale measurements of the angle of attack, span-wise angle and shaft torque were conducted following the procedure outlined in Section 3.3 [1]. Note that measurements presented here are angle of attack

---

[1] Presented at CANCAM 2015, June 1, 2015

measurements, as the measured local flow angle was corrected using the Biot-Savart law similar to the method used by NREL [18]. The measured angle of attack distributions at $r/R = 0.72$ with a γ=0° yaw-offset for $\lambda = 5.0$, 3.6 and 3.1 are presented in Figure 4.2.

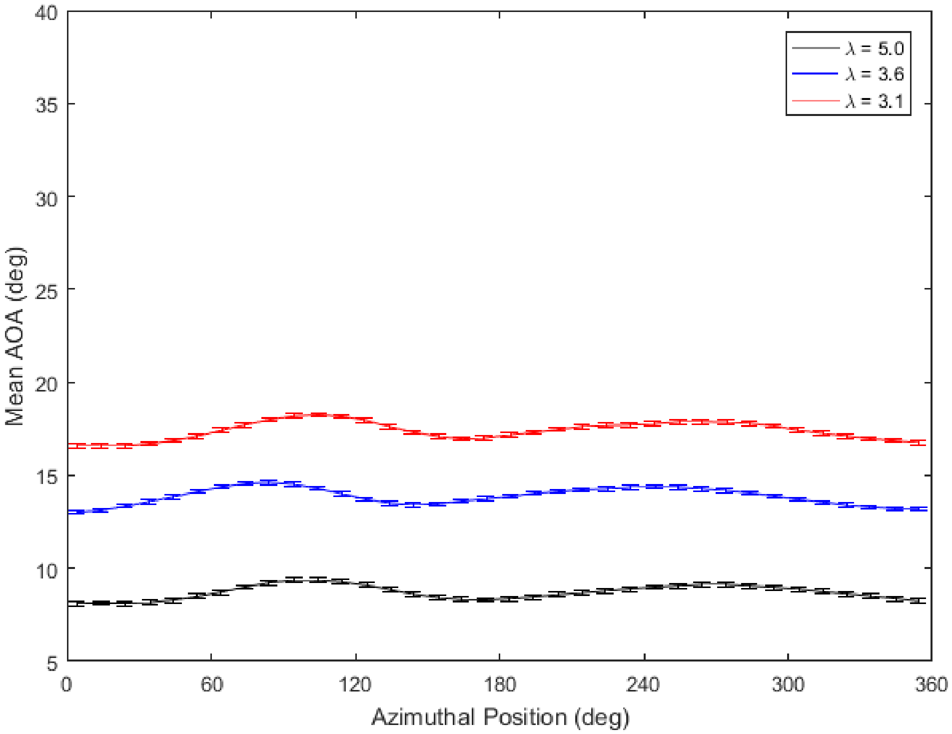

Figure 4.2: Measured α distribution at $r/R = 0.72$, $\gamma = 0°$

The angle of attack measurements shown match expected trends; as the velocity increases and the tip speed ratio decreases, the angle of attack grows in magnitude. This could be predicted by examining the velocity relationships in Figure 2.6, which shows that as the upstream wind velocity increases, the resultant vector W is aligned more with the upstream wind direction, increasing α. Because of the 0° yaw-offset, α remains nearly constant throughout the blade rotation, indicating that the effect of the facility floor on the flow is negligible over the small height difference of the wind turbine swept area. The only variation in the constant α distribution occurs at azimuthal positions at 100° and 200°. While the increase at 100° may be partially attributed to the flow non-uniformity, it is possible that the increase may also be caused by flow being guided around the nacelle and tower increasing the flow speed in these regions. The impact of the flow non-uniformity

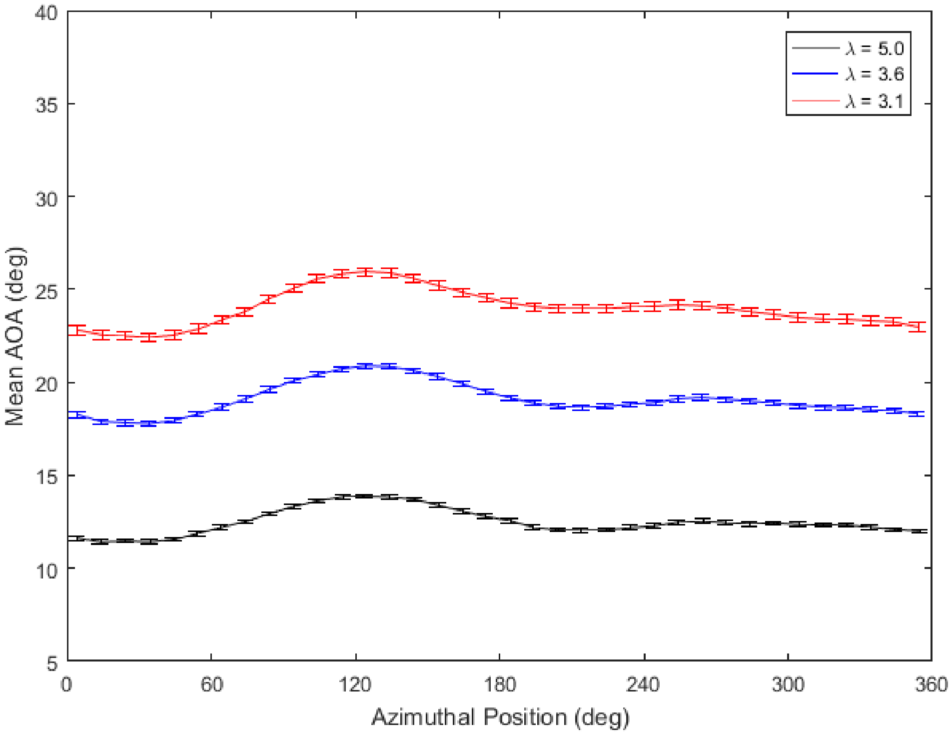

Figure 4.3: Measured α distribution at $r/R = 0.55$, $\gamma = 0°$

here is reduced relative to preliminary testing conducted without the extra flow dampening screen. The results of similar measurements taken at radial locations $r/R = 0.55$ and $r/R = 0.38$ are presented in Figures 4.3 and 4.4, respectively.

The measurements at $r/R = 0.55$ follow similar trends to those presented for $r/R = 0.72$. As the tip speed ratio λ decreases, the angle of attack increases, and the azimuthal variation remains relatively constant except for azimuthal positions close to 100° and 150°. Comparing the results at $r/R = 0.55$ to those at $r/R = 0.72$, it is observed that the angle of attack for all tip speed ratios has increased as the probe has moved further inboard. The increase in α can be explained using the velocity relationships defined in Figure 2.6. The angle of attack is defined as the angle between the chord line of the airfoil and the relative wind direction. As the probe is moved towards the root, the tangential velocity of the blade section it is connected to decreases, while the upstream wind velocity remains constant. The constant of the pitch of the wind turbine blade does not accommodate for

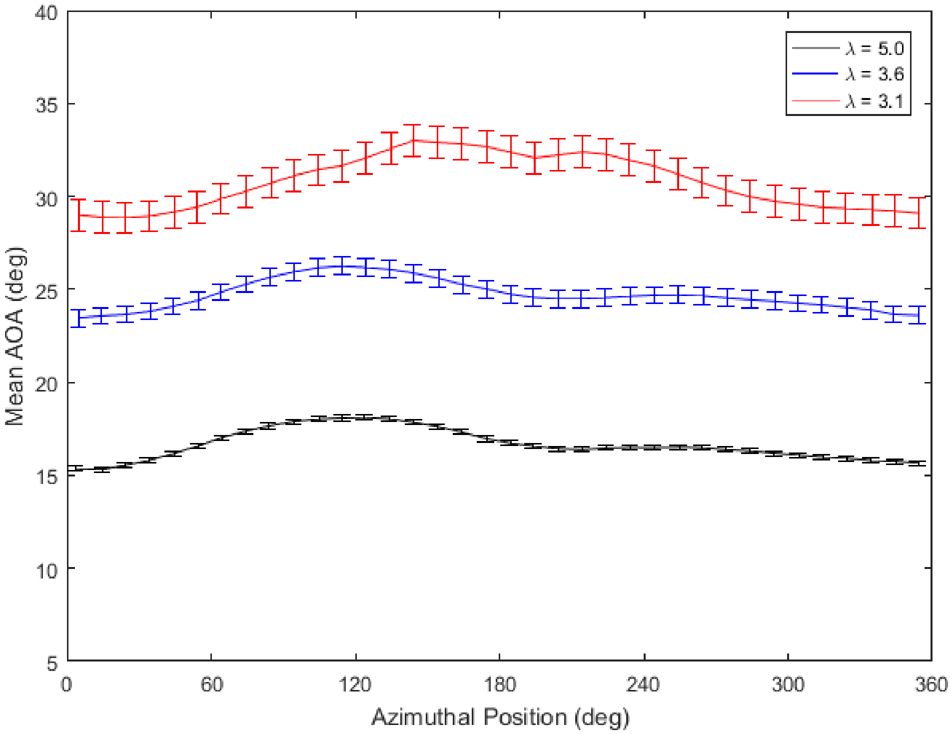

Figure 4.4: Measured α distribution at $r/R = 0.38$, $\gamma = 0^\circ$

the change in angle with r/R, and the relative wind velocity vector is therefore moved towards the upstream wind direction, which increases the angle of attack.

As the probe is moved inboard to $r/R = 0.38$, the measured angle of attack increases significantly by as much as 5° relative to $r/R = 0.55$. It can be observed in Figure 4.4 that, at high α values, the uncertainty associated with the measurements increases. In Figures 4.2 and 4.3, the uncertainty calculated using methods described in Section 3.5.3 is consistently less than ±0.2° given the low bias uncertainty and large number of samples. However, as the flow speed is increased in Figure 4.4, the uncertainty is shown to grow larger and larger, reaching approximately ±2° at $\lambda = 3.1$. Because the bias error and number of samples is consistent, the increased uncertainty must be due to a greater variation in the angles measured. It is posited that a greater variation in the measured angles could be due to an increased turbulence near the nacelle and root of the turbine blade as the wind speed is increased. However, the average values plotted follow the same trends as observed

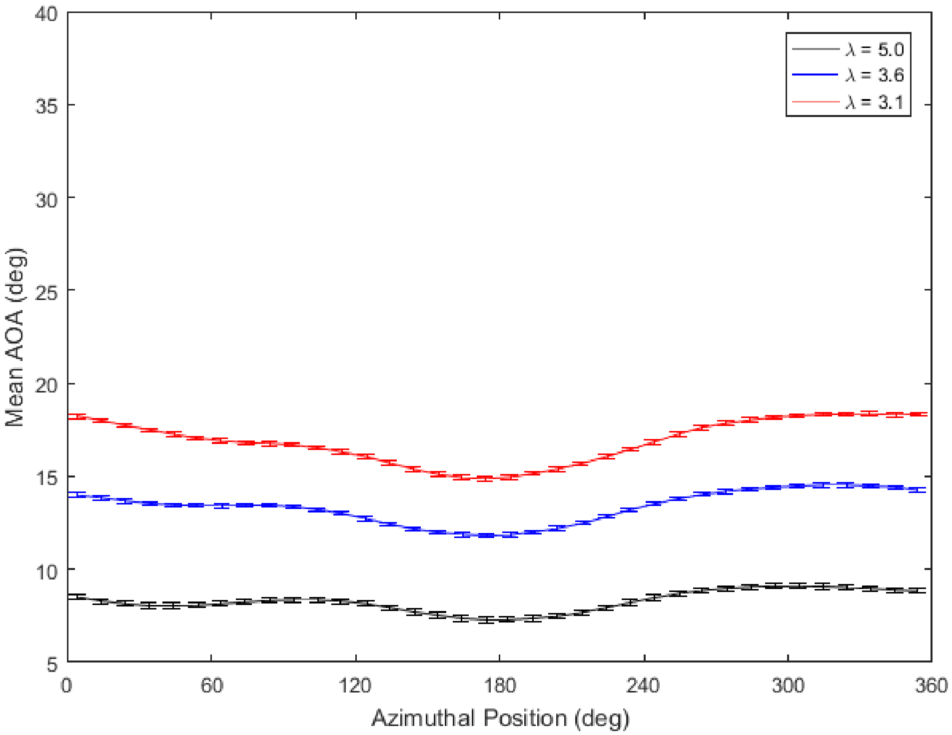

Figure 4.5: Measured α distribution at $r/R = 0.72$, $\gamma = 15^\circ$

at $r/R = 0.72$ and 0.55.

After testing with a 0° yaw offset, the test turbine was yawed to positions of ±15° and tests at the same tip speed ratios were conducted. Measured results at $r/R = 0.72$ at a yaw-offset position of +15° are presented in Figure 4.5. Note that a positive yaw degree position is defined as having the turbine rotated clockwise about the vertical axis, as defined in Figure 3.13.

Comparing the results shown in Figure 4.5 and 4.2, the oscillation in the angle of attack during yawed rotation can be observed. It is most apparent in the $\lambda = 3.1$ case, where the angle of attack has changed from a relatively constant 17° in Figure 4.2 to an oscillating value, peaking at nearly 18° at the 0° azimuthal position and a minimum of 15° at an azimuthal position of about 200° in Figure 4.5. It is expected that, if it were not for the increased flow speed at azimuthal positions near 100°, the plot shown would be symmetrical as the blade repeatedly rotated towards and away from the wind.

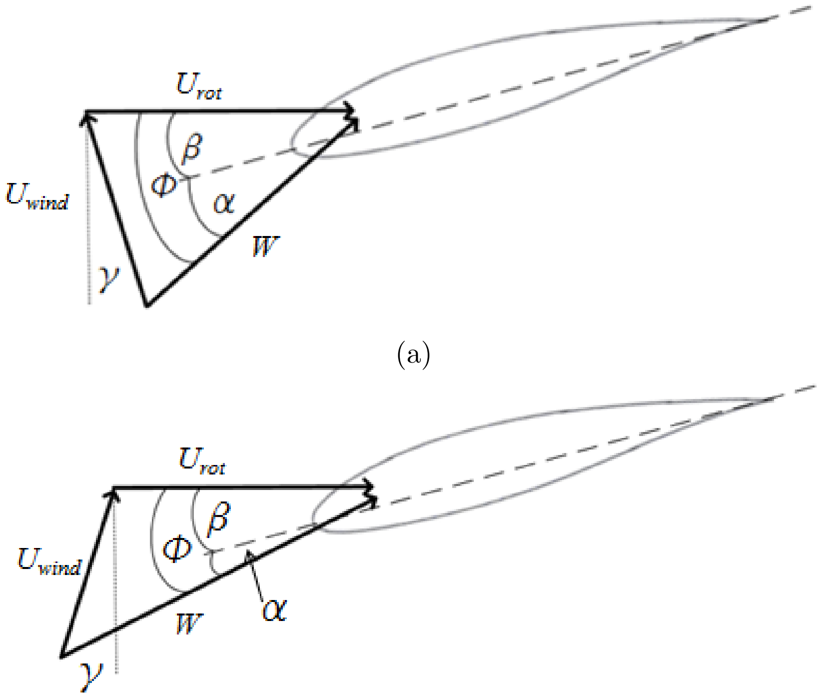

(a)

(b)

Figure 4.6: Demonstrative diagrams of the effect of wind direction on α for a blade rotating (a) with the wind and (b) against the wind

The oscillation in the angle of attack in the yawed case is similar to that observed by Maeda and Kawabuchi [21] as described in Section 2.2.2. As shown in Figure 2.13 (remembering that their convention has a 180° azimuthal position offset compared to the convention used here), the inflow velocity and angle of attack measured by the five-hole probe varied cyclically throughout the rotation. The reason for this is demonstrated in Figure 4.6.

The demonstrative diagrams shown in Figures 4.6a and 4.6b depict an upstream wind vector, U_{wind} oscillating from travelling away from the blade and towards the blade, respectively. It is observed that, in Fig. 4.6a, as the tail of the U_{wind} vector approaches the airfoil, the flow velocity W that the blade experiences decreases in magnitude while the angle of attack α simultaneously increases in magnitude. The opposite happens in Fig. 4.6b, where W increases in magnitude while α becomes smaller.

Given this oscillation, it could be expected that when the turbine is yawed in the oppo-

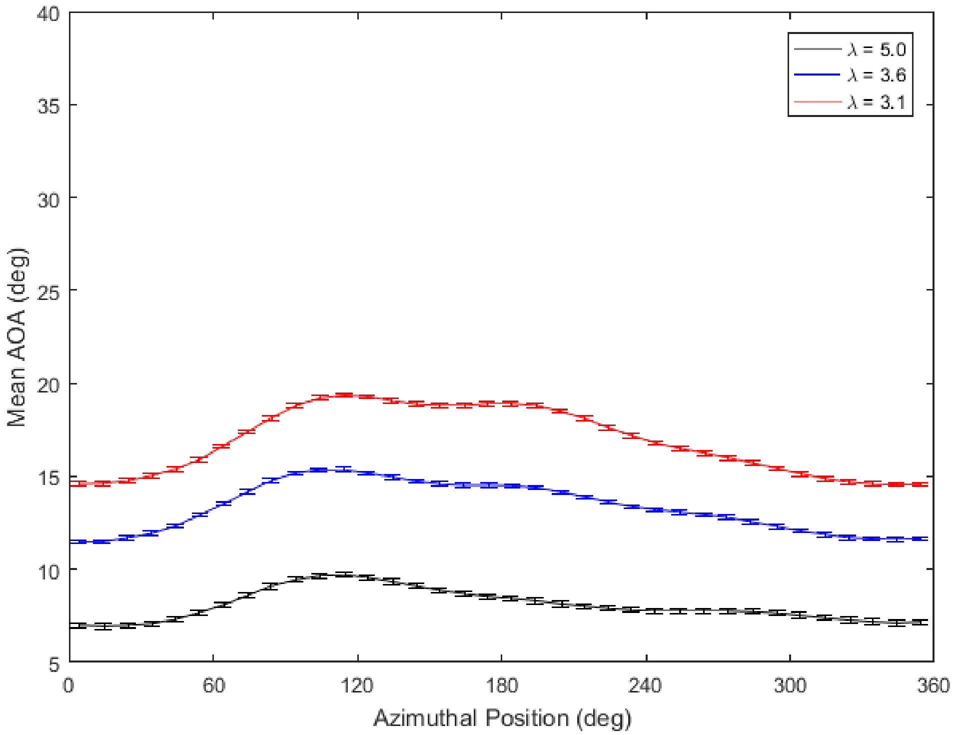

Figure 4.7: Measured α distribution at $r/R = 0.72$, γ = -15°

site direction to a -15° yaw-offset, the cyclical variation would be shifted by an azimuthal position of 180°. This is confirmed in the plot of measured results at $r/R = 0.72$, γ = -15° provided in Figure 4.7. Here, the non-uniformity of the flow field again skews the results slightly, but the variation in α with the azimuthal position is shown to be similar in magnitude to that observed in Figure 4.5, though offset now by 180° on the x-axis.

Similar to the axial flow cases, results at $r/R = 0.55$ for yaw-offsets of ±15° follow the same trends as the results at $r/R = 0.72$, though with higher angles of attack. The measured results at this location for $\gamma = \pm 15°$ are provided in Figures 4.8 and 4.9, respectively.

At $r/R = 0.55$, $\gamma = 15°$, the angle of attack cycles between maximum and minimum values once per rotation, similar to at $r/R = 0.72$. At $\psi = 0°$, as the blade rotates away from the wind, the angle of attack is at a maximum. The opposite occurs when the blade is oriented towards the wind at $\psi = 180°$. Results at γ = -15° plotted in Figure 4.9 follow a similar pattern, with α reaching a minimum as the blade rotates towards the wind at

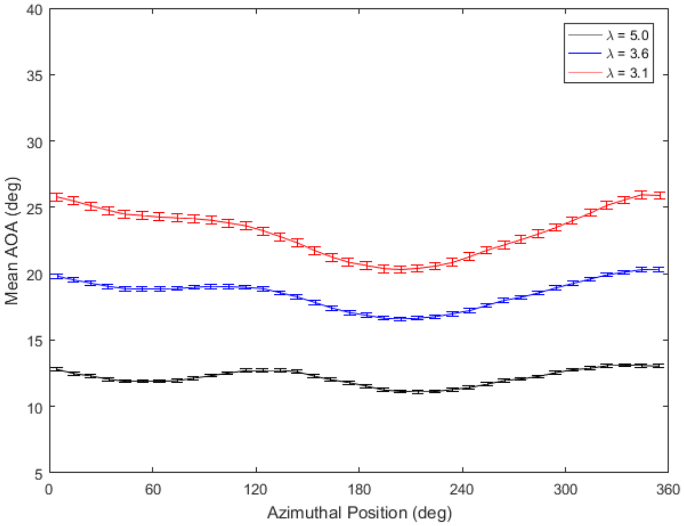

Figure 4.8: Measured α distribution at $r/R = 0.55$, $\gamma = 15°$

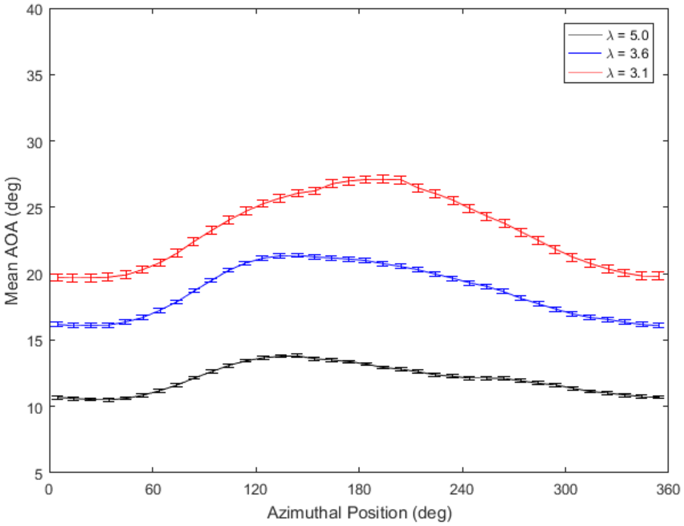

Figure 4.9: Measured α distribution at $r/R = 0.55$, $\gamma =$ -15°

$\psi = 0°$, and the maximum α occurring at roughly $\psi = 180°$ (neglecting the effect of the non-uniformity at approximately $\psi = 100°$). Comparing the results at $r/R = 0.72$ and 0.55 for the same yaw positions, the only significant difference is in the magnitude of the angle of attack, which is nearly 5° higher in the $r/R = 0.55$ case. As was explained for the axial flow case, this decrease in α can be attributed to the greater influence of the rotational speed vector in the velocity relationships defined in Figure 2.6.

Another thing to note in Figures 4.8)and 4.9 is that the angle of attack distributions measured are not symmetric about $\psi = 180°$, as would be expected given the geometry presented in Figure 4.6. The non-symmetrical distributions are partially caused by the flow non-uniformity at $\psi = 120°$, at which there is consistently an increase in the α value measured. However, the non-symmetrical measurements in the yawed case may also be caused by variations in the span-wise interference as described by the Morote [13] model in Section 2.1.6.

Looking to the measured results at $r/R = 0.38$ at a yaw-offset of -15° shown in Figure 4.10, the increased uncertainty in the axial flow case in Figure 4.4 has a more significant effect here. For the outer radial positions ($r/R = 0.55$, 0.72), uncertainty in the measured angle of attack remained below ±0.2°. However, it is suspected that the increased turbulence over the probe due to the nacelle and blade root resulted in greater uncertainty at $r/R = 0.38$ in axial flow. The effects of this are more apparent here as the measured angle of attack at $\lambda = 3.1$ decreases significantly from the peak of $\alpha = 38°$ down to $\alpha = 20°$.

The sudden decrease in α here is attributed to separation of the flow over the five-hole probe. Because the angle of attack measurement is dependent on an increased pressure at hole 1 and a decreased pressure at hole 3 in Figure 3.8, separation over hole 3 would reduce the pressure differential and cause a decrease in the calculated angle of attack. This shows that, while the calibration curves developed by Paul *et al.* [28] are capable of measuring flow angles up to ±50°, the current probe is not suitable for such angle magnitudes. For this reason, $r/R = 0.38$ values were not modelled, and these experimental results are not used for validation.

The effect of separation at $r/R = 0.38$ could be mitigated by increasing the probe offset angle relative to the chord line to more closely mimic the angle of attack at the radial location. However, because this would require a redesigned blade module for the inboard location, this solution was not implemented. For reference, the maximum angle of attack calculated using the Morote [13] model for $r/R = 0.38$, $\gamma = -15°$ was approximately 38°. The five-hole probe does measure values close to this angle when the blade passes $\psi = 180°$, likely due to the flow reattaching to hole 3 after the blade passes the flow non-uniformity.

To summarize the radial variation in the measured angle of attack, α distributions

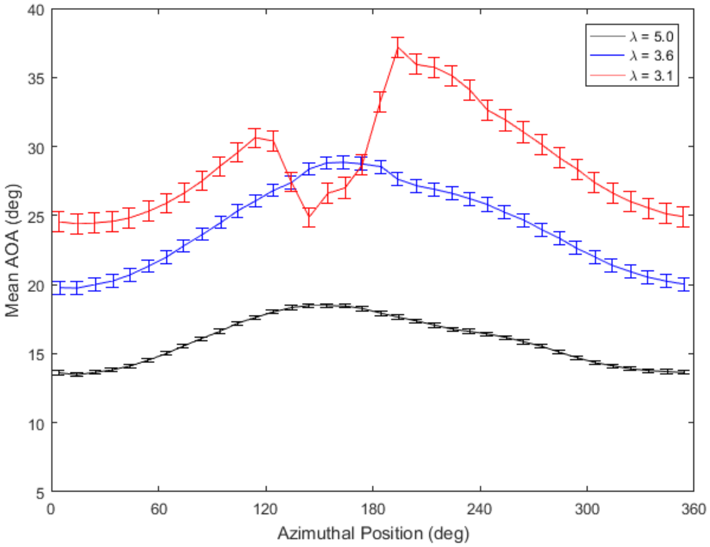

Figure 4.10: Measured α distribution at r/R = 0.38, γ = -15°

measured at the three radial positions at $\lambda = 4.2$, $\gamma = 0°$ are presented in Figure 4.11. It is observed that α increases as the five-hole probe is moved towards the root and r/R decreases. At the same time, as the probe is moved to $r/R = 0.38$, the increase in measured uncertainty relative to the $r/R = 0.72$ and 0.55 positions is clear. However, the trends observed in the azimuthal variation are similar between the three radial positions, with slight increases in α observed near $\psi = 120°$ and a relatively constant α distribution throughout the rest of the rotation.

4.1.3 Comparison to Models

The experimental results presented in the previous section demonstrate the successful use of the five-hole probe and in-blade data acquisition system to measure the angle of attack at the leading edge of a rotating wind turbine blade. Such measurements could be instrumental in correctly measuring and interpreting a wind turbine blade's performance. However, such data could also be compared to outputs from theoretical models to validate or guide their development.

Two theoretical models for predicting the variation in angle of attack with azimuthal position and yaw-offset were presented in Section 2.1.6. First was the historical model,

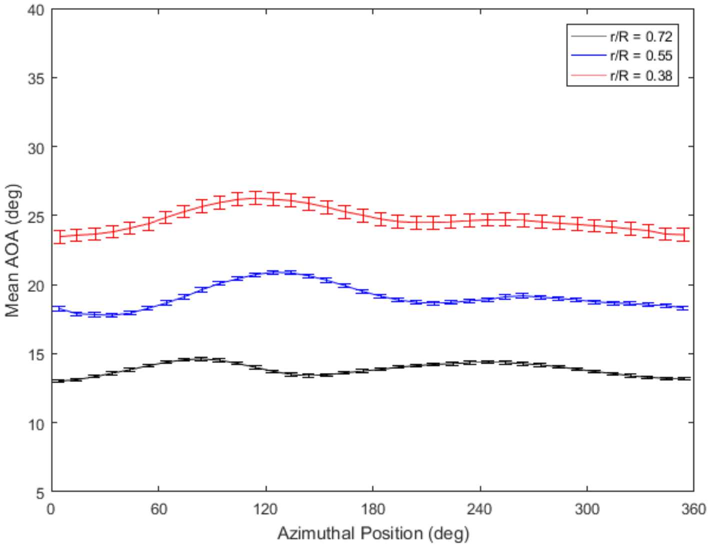

Figure 4.11: Measured α distribution at $\lambda = 4.2$, $\gamma = 0°$

reported by Burton *et al.* [2], and the second was developed by Morote [13]. In this section, the measured angle of attack values reported will be compared to the modeled values for the same set of configurations [2]. Only $r/R = 0.55$ and 0.72 positions were modeled given the significant uncertainty and separation observed at $r/R = 0.38$.

For both models, the axial induction factor, a, along the blade span was required for calculating the flow speed at the leading edge. Because tests were completed with the turbine in yaw-offset positions, the sonic anemometer could not be placed directly downstream of the blade during the final tests, meaning no independent wind speed measurements were made at the rotor plane at the test temperature. Therefore, to estimate the axial induction factor, a PROPID [9] (see Section 2.1.5) model of the Abdelrahman [10] blade and rotor was created based on the PROPID code originally used. By iterating through the blade momentum method with the blade and operational parameters set, a was calculated to range from 0.042 to 0.104. While these values may appear low considering the optimal axial induction factor is 0.33, it must be noted that the test rotor being used only has one real turbine blade. Given the reduced solidity of the rotor, the wind flow through the rotor meets less resistance than in a three-bladed turbine, resulting in a reduced axial induction.

Inputs to the theoretical models are provided in Table 4.1 and the calculated axial

---

[2] Published in Journal of Physics: Conference Series, V. 753

induction factors (discussed in Section 2.1.2 are summarized in Table 4.2. Note that as a simplification in the Morote [13] model, the axial induction factor a_0 was assumed to be equal to the azimuthally averaged axial induction factor a_{a0}. Theoretical models were not compared to the sonic anemometer measurements presented in Figure 4.1 due to the different tip speed ratios tested.

Table 4.1: Angle of Attack Model Inputs

Variable	Value	Units
U_∞	[7.05, 10.0, 11.45]	m/s
Azimuth	0 - 360	degrees
Rotational Speed	200	rpm
Pitch	6	degrees
r/R	[0.55, 0.72]	-
γ	[15, 0, -15]	degrees

Table 4.2: Summary of Calculated Model Axial Induction Factors

r/R	$\lambda = 5.0$	$\lambda = 3.6$	$\lambda = 3.1$
0.55	$a = 0.076$	$a = 0.059$	$a = 0.042$
0.72	$a = 0.104$	$a = 0.094$	$a = 0.074$

A plot of the angle of attack distribution calculated using the Burton *et al.* [2] and Morote [13] models for $r/R = 0.55$, $\gamma = 0°$ is presented in Figure 4.12. The experimental values for α are also plotted, for comparison.

The plot in Figure 4.12 shows that the Burton *et al.* [2] and Morote [13] models are nearly identical in a 0° yaw-offset case, with the Morote model estimating a slightly higher angle of attack at low tip speed ratios. As could be expected, for a 0° yaw-offset, both models predict zero variation in the angle of attack with azimuthal position. While the Morote [13] model may account for the variation in flow speed caused by wind shear (due to the floor) via an azimuthally varying a_0, the Burton [2] model has no such correction. The boundary layer effect has already been shown to be negligible for these experiments, though this may not be the case for larger, in-field wind turbines.

Comparing the modeled results to the experimental results also plotted in Figure 4.12, it was found that they are generally in good agreement. Neglecting the increased α at $\psi = 120°$, the models appear to slightly overpredict α at the lower wind speed cases ($\lambda = 5.0$ and 3.6) while underpredicting α at the higher wind speed. However, most of the plotted results are within ±1° of each other.

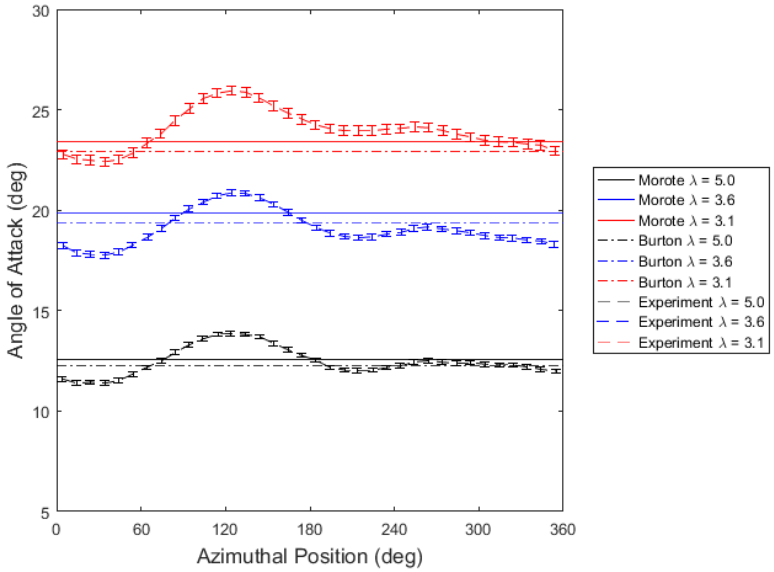

Figure 4.12: Modeled and Measured α distribution for $r/R = 0.55$, $\gamma = 0°$[2] [13]

Similar trends were observed at $r/R = 0.72$, as can be seen in Figure 4.13. However, as the probe was moved further outboard, the agreement between the models and the experimental results did decrease. It is posited that this is likely caused by an error in the predicted axial induction factor, as varying these values has significant impacts on the model outputs. For example, decreasing the axial induction factor at $r/R = 0.72$, $\lambda = 3.1$ by 10% from 0.074 to 0.067 corresponds to a 1% increase in α from 16.54° to 16.70°. While this is a seemingly small relative change, it does improve agreement between the models and experimental data at $\lambda = 3.1$.

Modeled and experimental α values at $r/R = 0.55$, $\gamma = 15°$ are presented in Figure 4.14. Modeling the angle of attack variation with a wind turbine yaw-offset presents the same azimuthal variation in α observed in the experimental results. The models both show peaks in α occurring at $\psi = 0°$ when the blade is rotating away from the wind and the minimum value occurring at $\psi = 180°$ when the blade travels towards the wind.

As was established in Figure 4.12, the models over-estimate the angle of attack at $\lambda = 3.6$ and 3.1. However, in the +15° yaw case, the modeled and experimental $\lambda = 3.1$ results are almost identical (neglecting the non-uniformity of the experimental flow field). Similar results were observed at a yaw-offset of -15°, as shown in Figure 4.15.

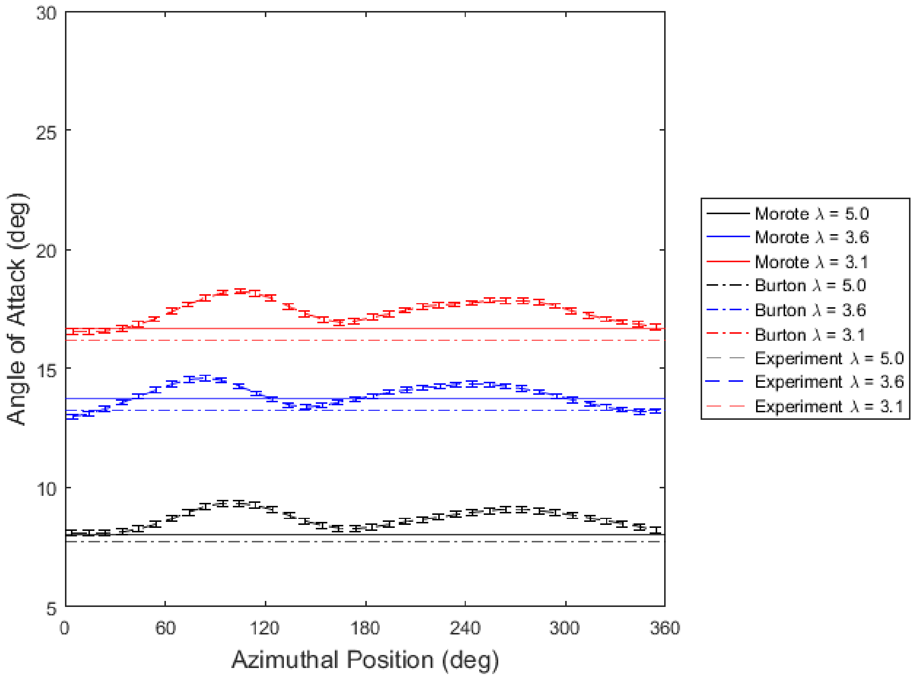

Figure 4.13: Modeled and Measured α distribution for $r/R = 0.72$, $\gamma = 0^\circ$[2] [13]

4.1.4 Characterization of Upstream Flow Field

As reviewed in Section 2.2.2, Petersen *et al.* [30] developed a method for estimating characteristics of the flow upstream of a wind turbine given five-hole probe measurements taken at the turbine rotor in axial flow. In this sub-section, the Petersen *et al.* [30] method is applied to the experimental results discussed in the previous sections to estimate the upstream flow speed, the axial induction factor of the blade, and the shear profile of the facility over the turbine area. These results are compared to the values expected given the set fan frequencies and PROPID [9] calculations.

The Petersen *et al.* [30] method requires more inputs than just the experimental results. The geometry of the rotor, including the chord length, number of blades, and airfoil performance data were input to the calculation to complete the model. Lift and drag curves for the NREL S833 airfoil [57] used were obtained from AirfoilTools [60] for Reynolds numbers of 200,000 and 500,000. It is estimated that, during testing, the flow over the five-hole probe reached Reynolds numbers ranging from 250,000 to 340,000. Interpolation was used

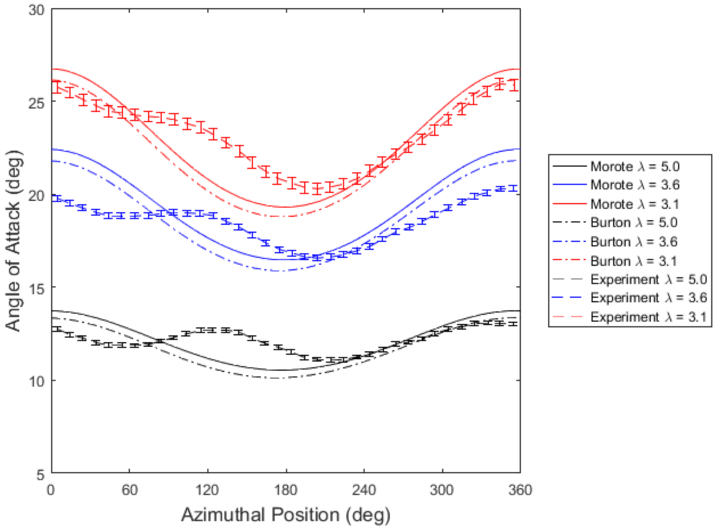

Figure 4.14: Modeled and Measured α distribution for $r/R = 0.55$, $\gamma = 15°$[2] [13]

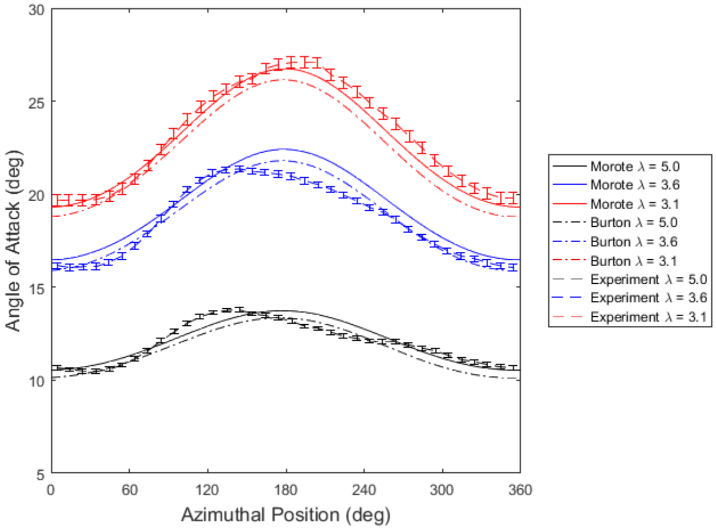

Figure 4.15: Modeled and Measured α distribution for $r/R = 0.55$, $\gamma =$ -15°[2] [13]

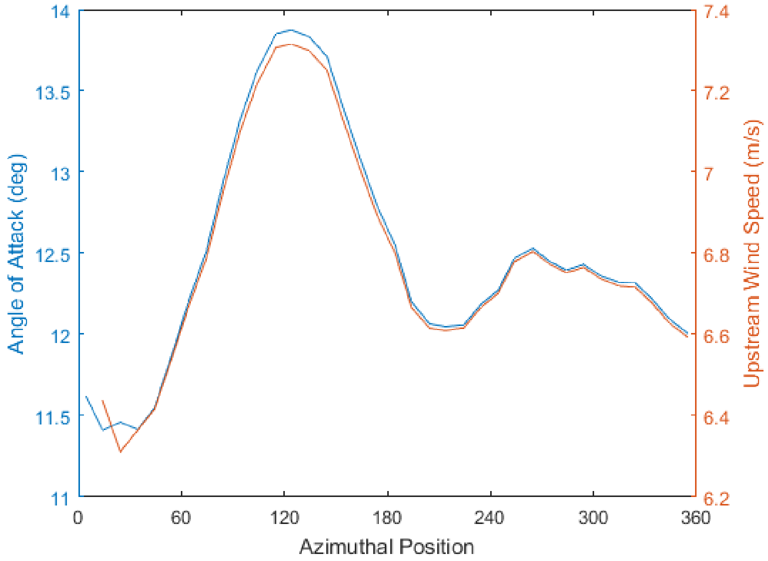

Figure 4.16: Comparison of Measured α Curve and Calculated U_∞ Curve for $r/R = 0.55$, $\lambda = 5.0$

to calculate the corresponding lift and drag data from the airfoil curves.

Because the geometry of the airfoil is a constant and the Reynolds number variation is also reflected in variations in the angle of attack measurements, the resulting estimations of upstream wind speed, U_∞, vary with azimuthal position according to distributions almost identical to the variations with α observed in Section 4.1.2. An example of this is plotted in Figure 4.16, which shows the measured α and corresponding U_∞ curve calculated using the Petersen *et al.* method at $r/R = 0.55$, $\lambda = 5.0$. This dependence is to be expected given that the variation in angle of attack is directly influenced by the variation in wind speed.

The calculated upstream wind speeds for the $r/R = 0.55$ and 0.72 tests are presented in Figures 4.17 and 4.18, respectively. Comparing the two, it is observed that the wind speed is relatively constant with azimuthal positions in all cases, which is to be expected given axial flow with a small wind turbine. It is also noted that the wind speeds estimated at $r/R = 0.55$ and 0.72 are in close agreement with each other. This similarity supports the validity of the Petersen *et al.* method as applied here, as the same fan frequency settings were used in both series of tests. The only impact of the change in radial location of the probe noticeable in the upstream wind speed estimates is in the magnitude of the increased

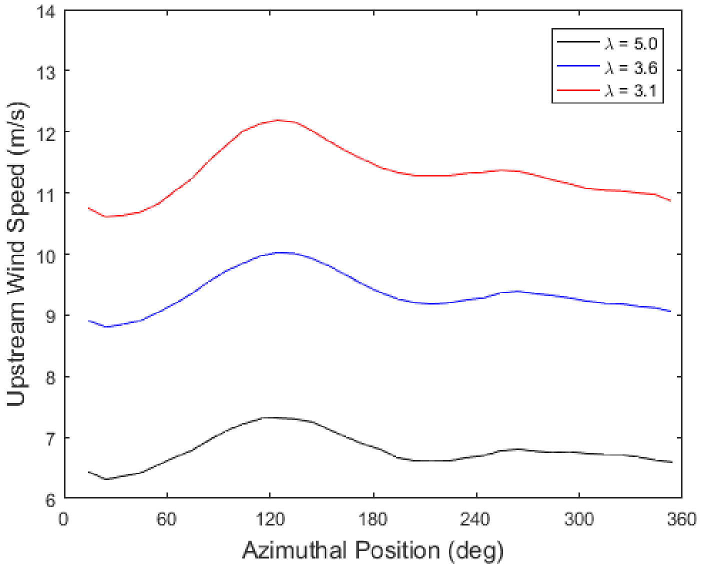

Figure 4.17: Calculated U_∞ Curve for $r/R = 0.55$ using the Petersen *et al.* [30] method

flow between $\psi = 100°$ and $150°$. The non-uniformity in the flow field seems to be more significant at $r/R = 0.55$ than at $r/R = 0.72$, which agrees with the measured flow field maps presented by Best [44].

Mean values of the calculated upstream flow speeds were used to compare the Petersen *et al.* [30] method results to the wind speeds set by the fan controller and used by PROPID [9]. Means of the calculated axial induction factors were also calculated to compare to the PROPID [9] values used as inputs to the Morote [13] model. Summaries of the values used and predicted by PROPID [9] and the corresponding values calculated using the Petersen *et al.* [30] method for $r/R = 0.55$ and 0.72 are presented in Tables 4.3 and 4.4, respectively.

Table 4.3: Comparison of PROPID [9] and Petersen *et al.* [30] values for $r/R = 0.55$

	PROPID [9]		Petersen [30]	
λ	U_∞	a	U_∞	a
5.0	7.05	0.076	6.78	0.034
3.6	10.00	0.059	9.35	0.019
3.1	11.45	0.042	11.31	0.000

The U_∞ values presented in Table 4.3 confirm what was expected from the plotted

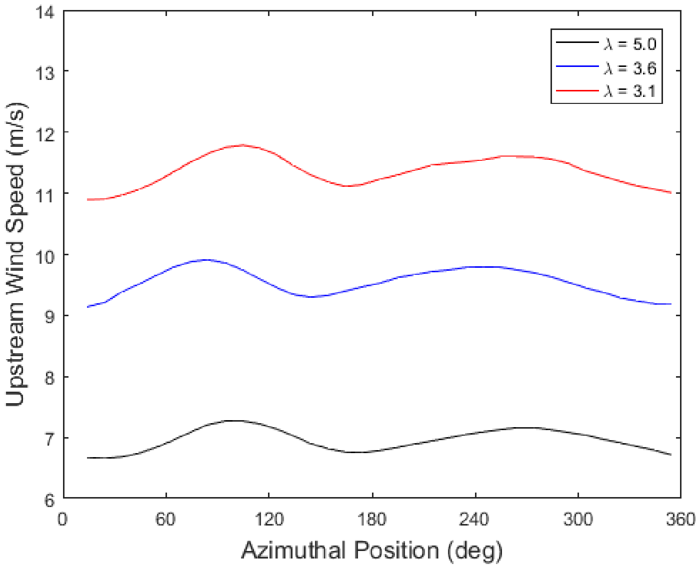

Figure 4.18: Calculated U_∞ Curve for $r/R = 0.72$ using the Petersen *et al.* [30] method

values in Figure 4.17; the upstream wind speed values calculated using the Petersen *et al.* [30] method are in close agreement with the expected values given the fan frequency settings. All of the calculated U_∞ values are within 7% of the values expected given the fan frequencies used and corresponding wind speeds as presented by Best [44]. Given the limited information used to iterate measurement data at the rotor to the upstream conditions, this is considered to be sufficient accuracy for assessing the true upstream wind values in the absence of a suitable meteorological tower.

Unfortunately, the calculated and expected axial induction factors do not show such close agreement. While the scale and trends of the values is similar (all values are small due to the single blade rotor and decrease with decreasing λ), the magnitude of the values is off by greater than 100%. At $\lambda = 3.1$, the axial induction factor output using the Petersen *et al.* method is $a = 0$, which is known to be false given that torque was being generated by the blade (as will be discussed in Section 4.1.6). It is expected that the error in the Petersen *et al.* [30] method axial induction outputs is due to errors in the lift and drag coefficients for the airfoil due to a lack of data in the narrow range of Reynolds numbers tested. While the Petersen *et al.* [30] method does account for the number of blades in the rotor, it is also possible that the induction model is not sufficiently accurate for a single-bladed wind turbine. All other inputs to the Petersen *et al.* [30] method are taken directly from five-hole probe measurements or the known blade geometry. Given the agreement between the Morote [13] models calculated using the PROPID [9] a values and the measured α values, as well as between the five-hole probe measurements and sonic anemometer measurements, it is posited that the values listed in Table 4.2 are more fitting to the experimental reality.

Table 4.4: Comparison of PROPID [9] and Petersen *et al.* [30] values for $r/R = 0.72$

	PROPID [9]		Petersen [30]	
λ	U_∞	a	U_∞	a
5.0	7.05	0.104	6.95	0.0318
3.6	10.00	0.094	9.53	0.0279
3.1	11.45	0.074	11.34	0.0221

At $r/R = 0.72$, the expected and calculated U_∞ values are again in very close agreement, with the $\lambda = 3.1$ values being nearly identical. This again supports the use of Best's [44] wind speed measurements at the given fan frequencies. However, the axial induction factors at the $r/R = 0.72$ radial location were shown to be just as erroneous as at $r/R = 0.55$. Again, the a values output using the Petersen *et al.* [30] method were found to be significantly less than the expected values, and also decreased with decreasing λ.

Effect of Floor Shear

Angle of attack measurements throughout the wind turbine rotation can also be used to estimate the strength of the boundary layer and wind shear over the wind turbine rotor area. As was discussed in Section 2.1.3, friction between the wind and terrain causes the formation of a boundary layer and, by extension, an increase in the upstream wind velocity with elevation. While many large-scale wind turbines may be elevated above any significant boundary layer effects, the distribution of wind speeds can be significant over small-scale wind turbines such as the test turbine used in this project.

As discussed in Section 2.2.2, the upstream flow speed estimations calculated using the five-hole probe measurements may be used to estimate the effect of the boundary layer. By converting the azimuthal position of the five-hole probe to a height off the ground (*i.e.* treating the probe location as a sine wave oscillating about the rotor height), the wind speed calculated using the five-hole probe measurements could be plotted as a function of the height. Wind shear results calculated using this method and measurements acquired at $r/R = 0.72$ are plotted in Figure 4.19.

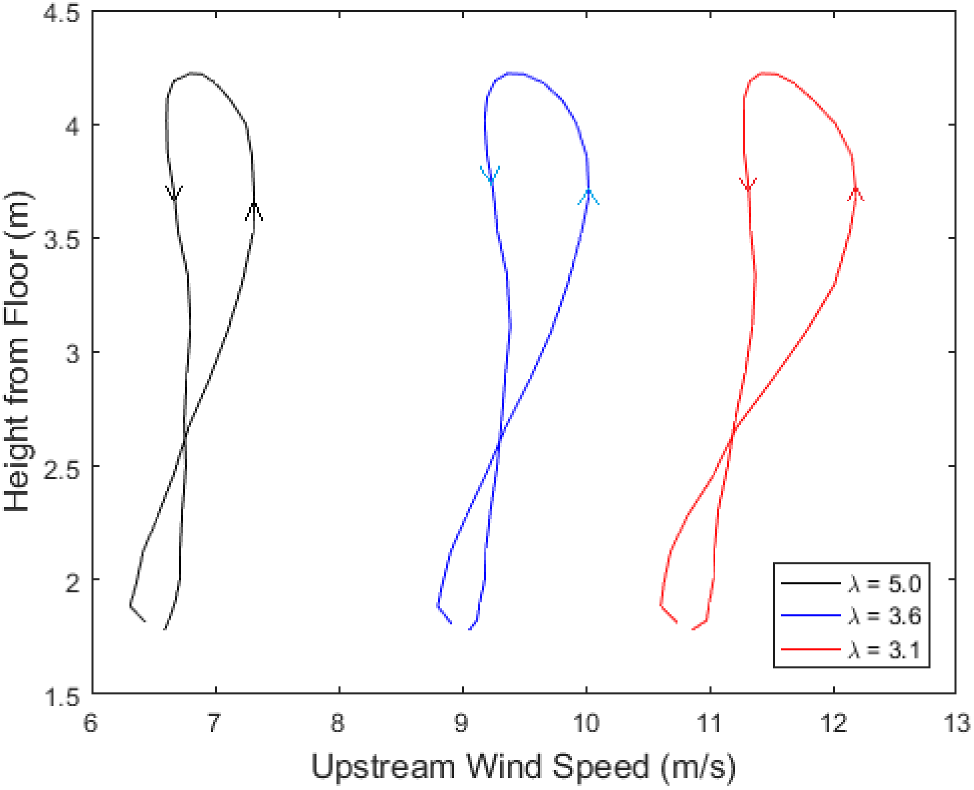

Figure 4.19: Estimated Upstream Wind Shear Profile Based on Probe Measurements and the Petersen *et al.* [30] Method

The curves plotted in Figure 4.19 depict the upstream flow velocity from heights of approximately 1.8 m to 4.2 m. The curves at each tip speed ratio appear to show a shear profile when the blade travels upwards, increasing in speed almost linearly with height. However, this increase in speed is actually caused by the non-uniformity in the flow, as was shown in the angle of attack measurements presented in Section 4.1.2. The true vertical profile of the wind at each tip speed ratio is depicted by the corresponding vertical line, generated as the probe measures the wind velocity while descending. This plot acts as a final confirmation that the wind shear acting over the wind turbine swept area due to the proximity to the ground is negligible.

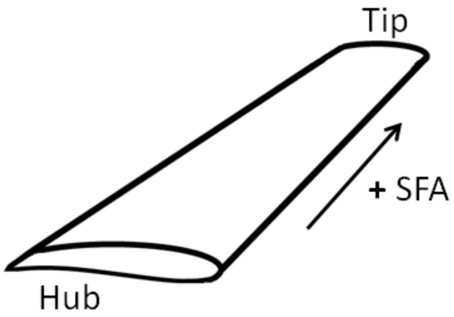

Figure 4.20: Positive direction convention for the span-wise flow angle; the SFA is positive when flow moves outboard

4.1.5 Span-Wise Flow Angle Measurements

While the primary use of the five-hole pressure probe in this project has been to measure the angle of attack at the leading edge of the airfoil, the variation in the measured span-wise angle can also be interesting and informative as to how the air flow passes over the airfoil. The span-wise flow angle, labelled as SFA in Equation (2.35) and in Figure 2.12 is defined as being positive when the flow direction is outboard (*i.e.* toward the tip of the blade). A diagram depicting the positive flow convention is provided in Figure 4.20. The average measured span-wise flow angle during axial rotation at radial positions of $r/R =$ 0.55 and 0.72 are provided in Figures 4.21 and 4.23, respectively.

The span-wise flow angles measured at $r/R = 0.55$ indicate that the flow over the blade is consistently oriented a minimum of 15° outboard throughout the wind turbine operation, with values increasing as λ decreases. The outboard movement is to be expected when reviewing the actuator disc model presented in Figure 2.5 in the Aerodynamics Review of Section 2.1.2. As the wind approaches the turbine rotor, the flow cylinder slows and expands outward, which causes the wind approaching the hub of the turbine to flow towards the tips of the blades. As the wind speed increases, the laws of continuity for the actuator disc would indicate that, to achieve the same volume flow rate, either the induction through the rotor must decrease (as seen in Tables 4.3 and 4.4) or the downstream area of the streamtube must grow in diameter, which would result in increased span-wise flow angles. The results presented here indicate that both scenarios occurred during the experiments.

The span-wise flow angles at the three tip speed ratios presented in Figure 4.21 all increase in magnitude at azimuthal positions of approximately 150° to 250°, which would indicate that there is an upward flow in the facility when the turbine is operating. A

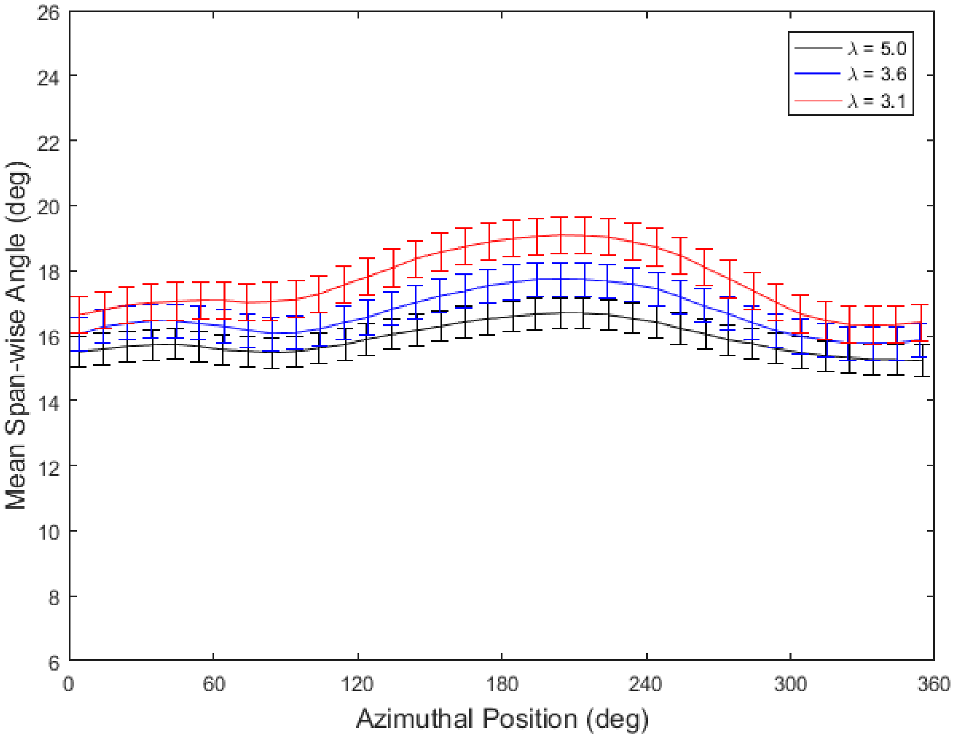

Figure 4.21: Measured span-wise angle distribution at $r/R = 0.55$, $\gamma = 0^{\circ}$

diagram depicting the existence of an upward flow in the upstream wind flow is provided in Figure 4.22. This was confirmed by examining the vertical component of the sonic anemometer measurements taken during the probe verification experiments relative to the axial flow velocity. The x- and z-components of the wind velocity measured (where the x-component is axial and z-component is vertical) using the sonic anemometer were used to calculate an upward flow angle of approximately 4° at azimuthal positions around 180° in all three tip speed ratios tested.

Given the proximity of the five-hole probe to the ground when at the lower portion of the rotation, it could be posited that the outboard flow at the lower portion of the rotation is impeded by the limited space available for expansion, while the open area at the upper part of the rotation is better suited to expanding the streamtube outwards.

The uncertainty bars plotted on Figure 4.21 (as well as the other span-wise angle plots presented) appear significantly larger than the error bars associated with the angle of

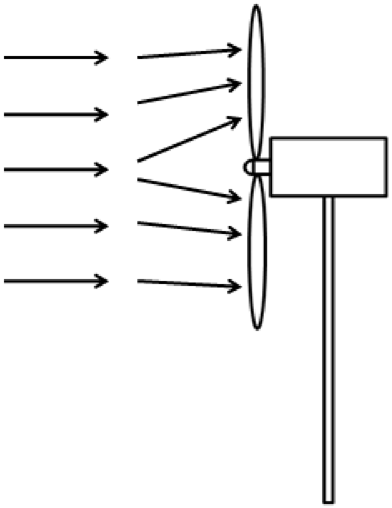

Figure 4.22: Diagram depicting a slight upward flow in the wind velocity in azimuthal positions of $\psi = 150°$ to $250°$

attack measurements presented in Section 4.1.2. While a portion of this is caused by a relatively larger bias error associated with the probe angle offset (± 0.2° versus ± 0.1°), the dominant source of uncertainty in the span-wise angle measurements is an increase in measurement variations. However, the measurements presented are consistently within ± 0.6° with a 95% confidence, and this is considered sufficient for the span-wise flow angle measurements.

Comparing the span-wise flow angle measurements at $r/R = 0.72$ to those at $r/R = 0.55$, the same trends in the data are observed. The span-wise flow angle increases with a decreasing tip speed ratio, indicating that the flow is oriented more and more towards the tip of the blade as the flow speed is increased. The same upward flow at azimuthal positions of approximately 150° to 250°is observed at all three tip speed ratios, though the magnitude of the increase is small compared to the relatively constant span-wise flow angles throughout the rotation. Of note is that the magnitude of the angles measured at $r/R = 0.72$ is several degrees less than those measured at $r/R = 0.55$. This decrease is likely due to the reduced impedance of the axial flow as the flow moves further away from the blunt body of the rotor hub and nacelle. That is, closer to the nacelle, the flow must move further outboard to circumvent the turbine body than the flow closer to the tip, resulting in larger span-wise flow angles near the root of the blade.

Span-wise flow angle measurements were also measured and plotted for blade rotations

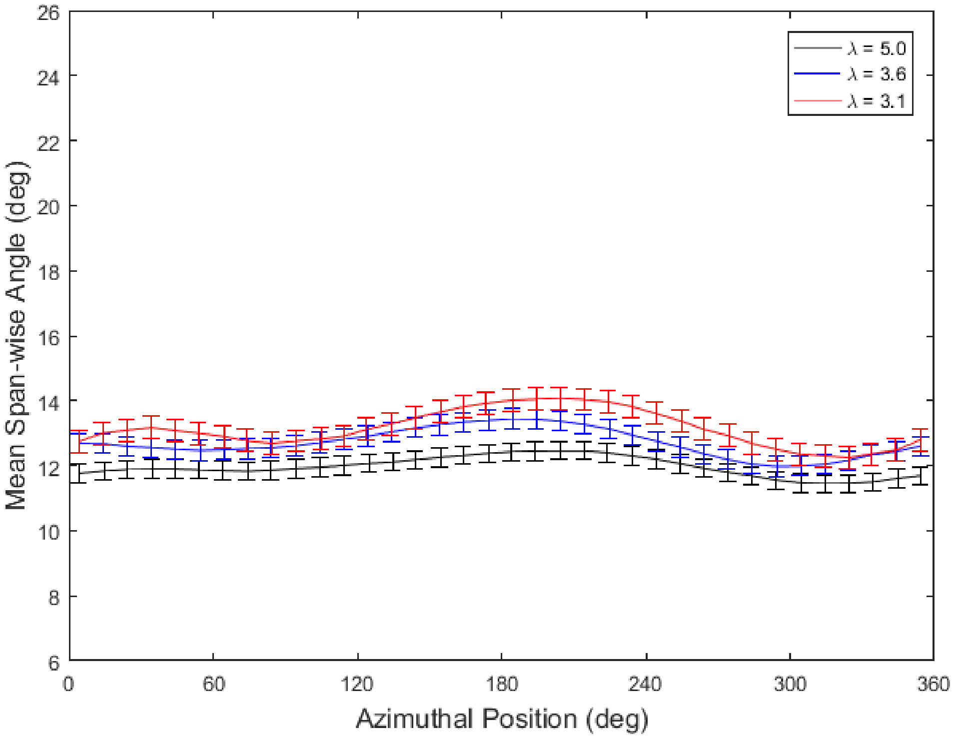

Figure 4.23: Measured span-wise angle distribution at $r/R = 0.72$, $\gamma = 0°$

in a non-axial flow. Results at $r/R = 0.55$ for turbine yaw positions of +15° and -15° are presented in Figures 4.24 and 4.25, respectively.

When the wind turbine is yawed, the span-wise flow angle oscillates significantly throughout the blade rotation, with the amplitude of the oscillation increasing with decreasing λ. When the turbine is yawed +15°, the span-wise flow angle reached a maximum value at approximately $\psi = 90°$ and a minimum at approximately $\psi = 270°$. The opposite occurred with the turbine yawed -15°. This distribution matches the variation expected when considering how the flow is passing over the wind turbine blade. When the turbine is yawed +15°and the blade is at $\psi = 90°$ (or the 9 o'clock position), the test blade is then oriented horizontally in space and pointed 15° downstream. A portion of the upstream flow is therefore travelling parallel to the blade towards the tip, adding to the flow expansion of Figure 2.5. When the blade is horizontal and pointed towards the upstream wind, as at $\psi = 270°$, the upstream flow speed is then travelling partially from the tip of the blade

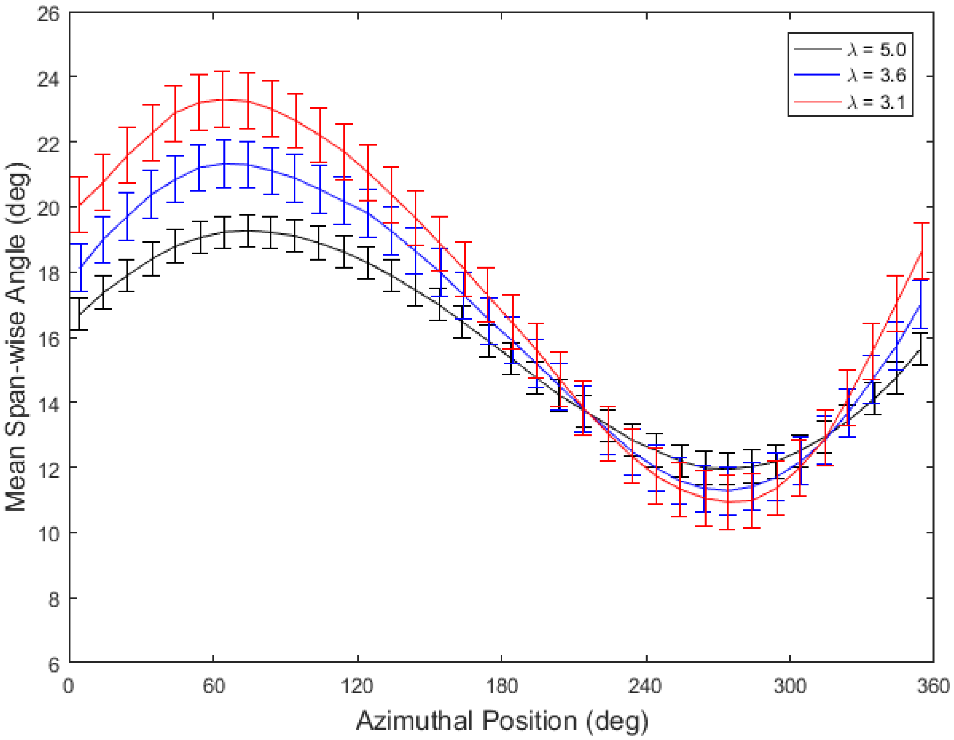

Figure 4.24: Measured span-wise angle distribution at $r/R = 0.55$, $\gamma = 15^\circ$

towards the hub, acting against the streamtube expansion and decreasing the span-wise flow angle. The same pattern is observed when the turbine is yawed -15°, with the only difference being the phase of the sine curve.

The span-wise flow angle measurements presented here are similar to those presented (called ”slip angle”) by Maeda and Kawabuchi [21] in Figure 2.13c. In axial flow, they measured an almost constant span-wise flow angle of approximately 13° throughout the full 360° rotation. However, when the wind turbine was yawed ±45°, the span-wise flow angle took the form of a sine wave as it did in Figures 4.24 and 4.25 for this study. Maximum and minimum values occurred at azimuthal positions of 90° and 270° when the blade was oriented horizontally, and the only difference observed between the positive and negative yaw cases was a 180° phase shift in the results, which matches the trends observed in the current data. A similar oscillation can be observed in the preliminary angle measurements presented by Moscardi and Johnson [22] using the same five-hole pressure probe and wind

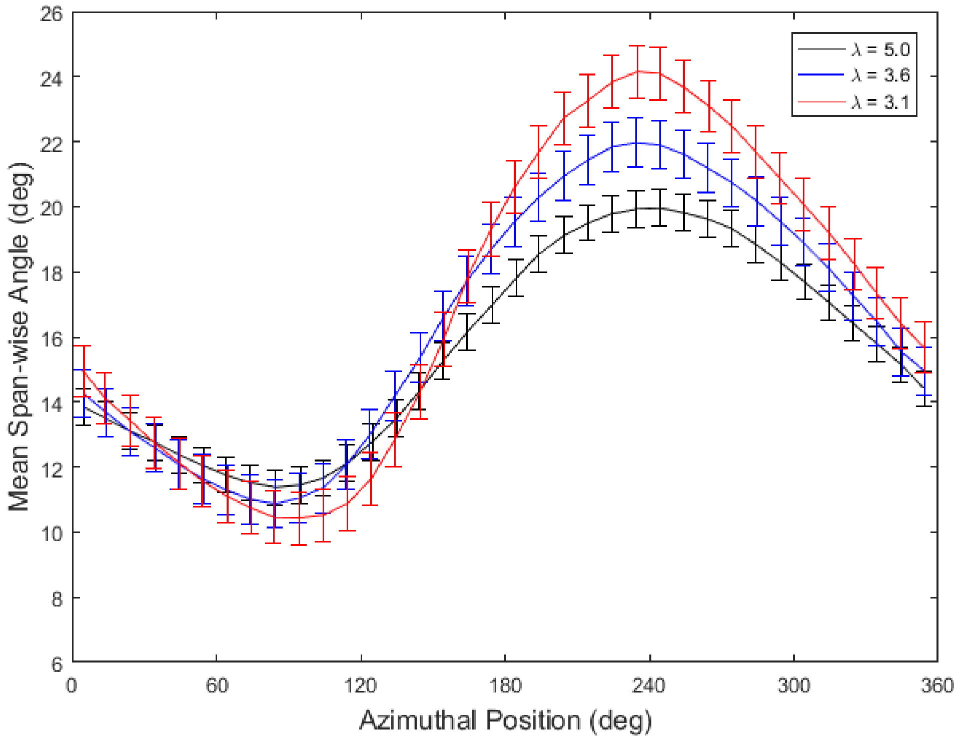

Figure 4.25: Measured span-wise angle distribution at $r/R = 0.55$, γ = -15°

turbine, though here it is presented as a variation in span-wise flow angle with time.

Examining the span-wise angle measurements at $r/R = 0.72$ during ±15°, the same trends observed at $r/R = 0.55$ are present. In Figures 4.26 and 4.27, the span-wise flow angle values oscillate with azimuthal position again, following the same distribution seen at $r/R = 0.55$. Similar to the cases observed during axial flow, the magnitude of the span-wise angles (and the amplitude of the oscillation) is decreased when the probe is closer to the tip as opposed to being closer to the root.

Something of note in Figures 4.24 through 4.27 is that the flow non-uniformity which has affected measurements between $\psi = 150°$ and 180° in most other configurations has not had a significant effect on span-wise flow angles in the same azimuthal range. However, as was observed in Figures 4.21 and 4.23, an increase of roughly 1 m/s in the axial direction does not result in significant changes to the span-wise flow angle. The effects of the flow speed variation caused by the flow non-uniformity are therefore insignificant relative to the flow speed variation the blade experiences naturally through yawed operation.

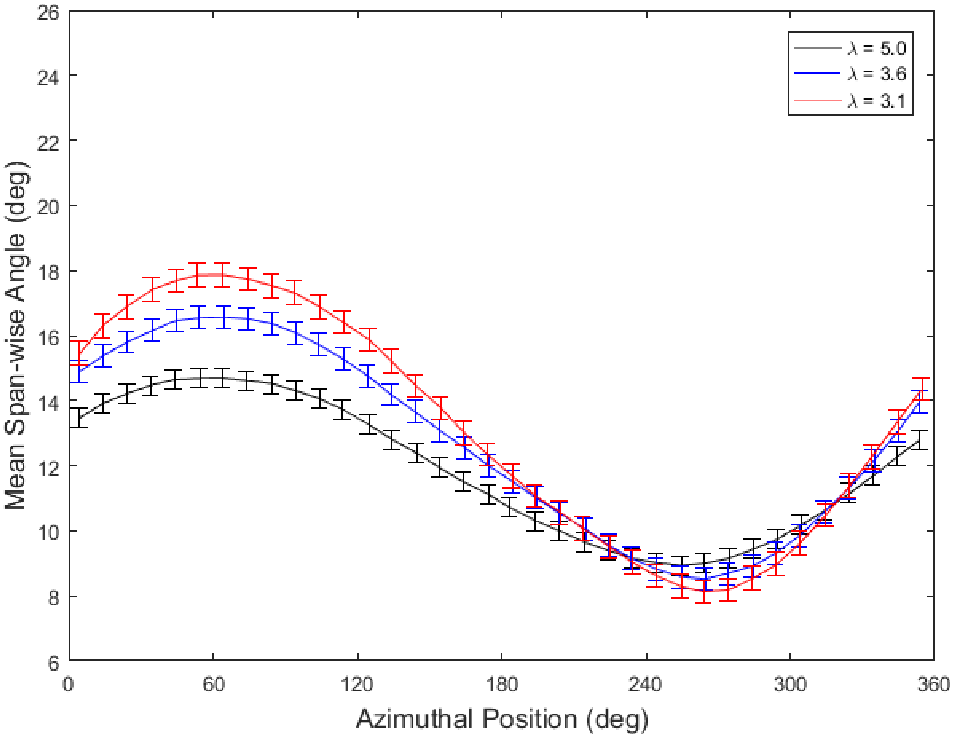

Figure 4.26: Measured span-wise angle distribution at $r/R = 0.72$, $\gamma = 15°$

The presentation of span-wise flow angle measurements here was done primarily for general interest, as the span-wise flow angle does not have a significant effect on the operation of the wind turbine blade or airfoil performance as the angle of attack does. However, as was discussed in Section 2.1.6, the span-wise flow interference can be an essential part of accurately predicting the interference functions when modelling the angle of attack distribution, as was done by Morote [13]. Having experimental measurements of the span-wise angle distribution may provide another route for validating theoretical α models or guiding the development of more accurate interference functions.

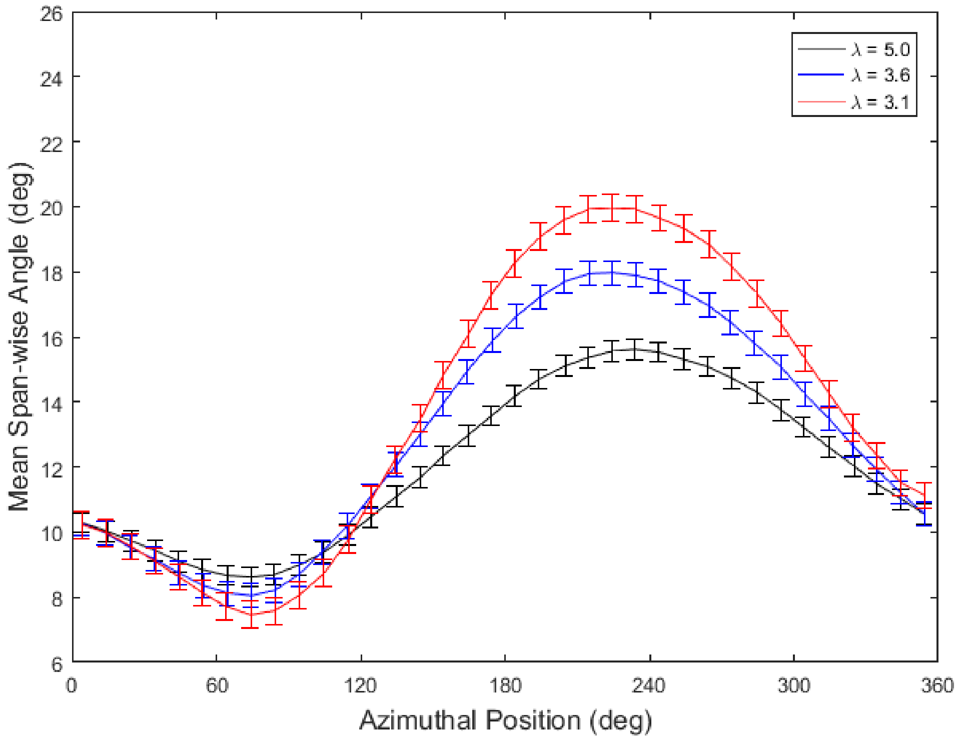

Figure 4.27: Measured span-wise angle distribution at r/R = 0.72, γ = -15°

4.1.6 Torque Measurements

The magnitude and orientation of flows over the rotating test blade were not the only variables measured during the five-hole pressure probe experiments. To quantify how the variations in angle of attack and span-wise flow angle may affect the power performance of the wind turbine, shaft torque measurements were also recorded as described in Section 3.2. Because the torque was recorded on the shaft, the radial location of the probe did not have any effect on the values measured. Therefore, the average torque distributions measured for testing at axial flow are presented in Figure 4.28. The torque required to rotate the wind turbine rotor at 200 rpm with no upstream flow is also plotted to provide a baseline for comparison.

The results presented in Figure 4.28 show that, during testing, the test turbine was always operating at a negative torque. This signifies that the rotation of the wind turbine rotor was always being driven by the electric motor, rather than the rotor driving the

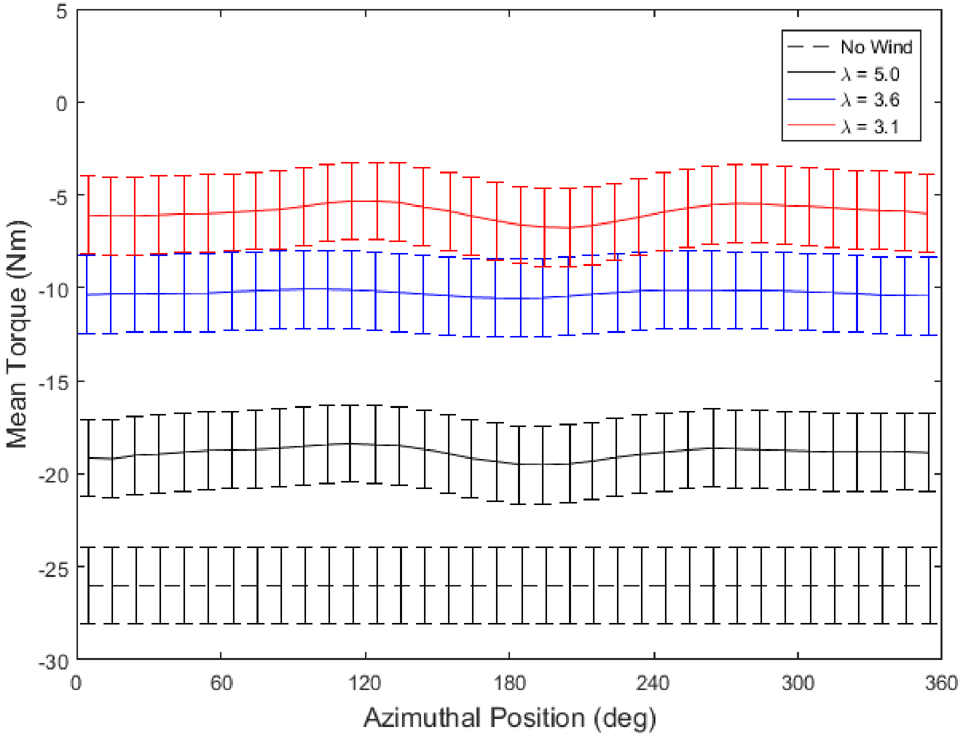

Figure 4.28: Measured shaft torque distribution at $\gamma = 0°$

generator as would be expected in a true wind turbine operation. The negative power output of the test turbine is reasonable however given that all of the testing was completed with only one test blade attached, while also rotating two extra weighted rods that offered nothing in terms of aerodynamic lift or torque generation.

When the turbine was rotating with no upstream wind, the rotor was measured to require approximately -26 Nm of torque to maintain a constant speed (*i.e.* overcome friction and drag forces). As the fans were turned on and wind generation began, the torque required to drive the turbine decreased, indicating that the single blade was generating some torque and decreasing the load on the motor. The increases in torque from the No Wind case to $\lambda = 5.0$, and again up to $\lambda = 3.6$ are significant, decreasing the required torque by as much as 15 Nm. However, the additional torque generated at $\lambda = 3.1$ is not as significant a change, indicating that, while the test blade is still generating more lift and torque, stall occurring on the blade at the greater angles of attack may also be starting to

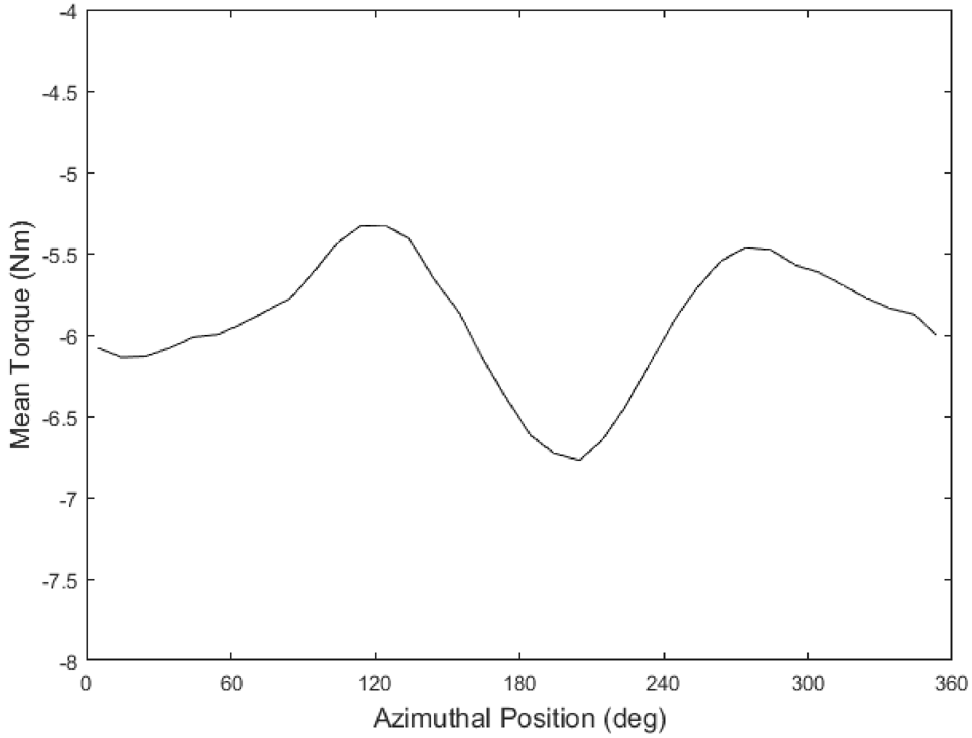

Figure 4.29: Measured shaft torque distribution at $\lambda = 3.1$, $\gamma = 0°$

affect the performance of the blade.

The shaft torque was essentially constant with azimuthal position for every tip speed ratio tested. This would indicate that, while the angle of attack was observed to increase in the flow non-uniformity around positions of $\psi = 150°$, this variation did not have any significiant effect on the torque generated by the test blade. This could be due to a dampening effect of the inertia of the test blade and weighted rods, which may average out any increased forces on the blade to a constant value. For more information concerning the relative inertia of the turbine rotor and aerodynamic forces, see Appendix F.

To more closely examine the variation in torque with azimuthal position, the torque generated at $\lambda = 3.1$ in axial flow was plotted and presented in Figure 4.29. Error bars were removed from the plot for clarity. When the resolution is increased, it can be seen that the azimuthal variation in the torque, while not significant, does follow a similar trend as observed with the angle of attack in Figure 4.3: the values increase at approximately ψ

= 100-150° and 325°. This would indicate that, while the variation is so small to as not be visible in Figure 4.29, increases in α are being reflected as increases in the torque. This is attributed to an increasing lift coefficient as described in Section 2.1.1. However, the approximately 4° change in α measured with the five-hole probe translates to a variation in shaft torque of less than 2 Nm. To find this value, the angular momentum of the turbine rotor was calculated, as well as the change in lift and drag forces on the blade resulting from an increase in α (see Appendix F for more details). This supports the idea of the shaft torque of the wind turbine rotor being dampened or averaged due to the inertia of the rotating blades. Similar results are observed when the turbine was yawed, which can be seen in Figure 4.30.

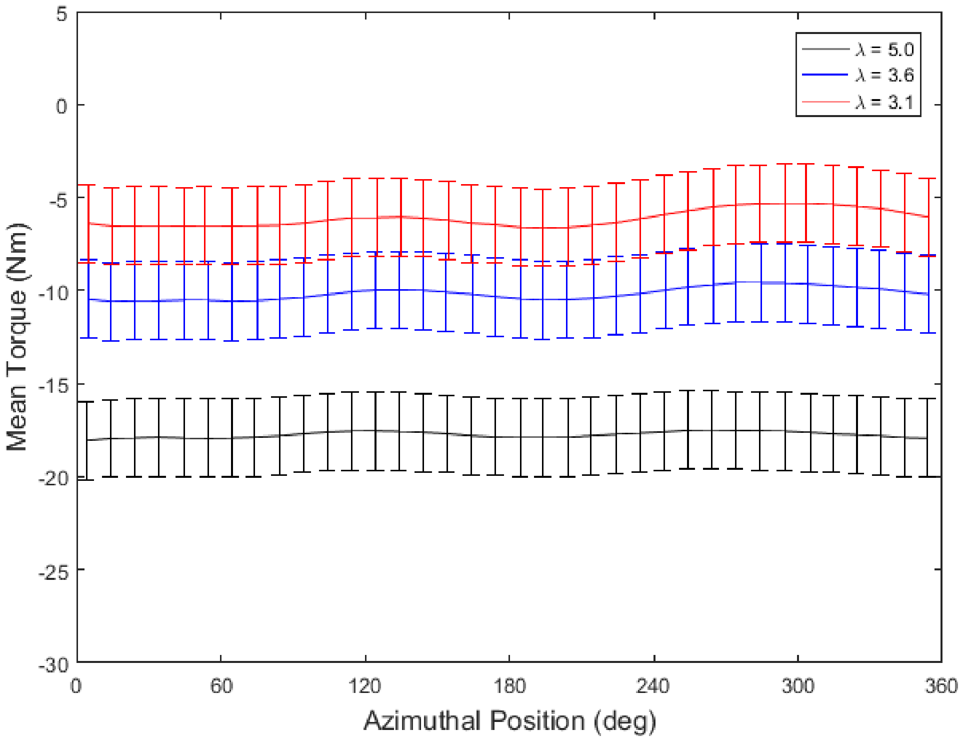

Figure 4.30: Measured shaft torque distribution at $\gamma = 15°$

When the turbine was yawed, the torque results measured were surprisingly similar to the results measured during axial flow. Despite significant changes in the angle of attack observed on the single test blade, the shaft torque plotted in Figure 4.30 shows no significant variation with azimuthal position. This may again be due to dampening caused by the masses of the wind turbine blade and weighted rods, or it may also be a reflection of the insignificant changes in torque on the single test blade with changes in angle of attack (see Appendix F). When the resolution is increased however, as in Figure 4.31 which presents the ±15° yaw data for torque at $\lambda = 3.1$, the minor variations in torque can be observed.

In Figure 4.31, it is shown that the azimuthal distribution of the measured torque when the turbine is yawed follows a distribution opposite to the span-wise flow angles plotted in Figure 4.24 and 4.25. That is to say that, at horizontal positions when the blade is oriented away from the wind, the torque measured was at the minimum value, and the maximum torque values were measured with the blade oriented towards the wind. These distributions do not agree with the distributions observed in the angle of attack, which is unexpected. It is posited that the increase in torque coincides with slight increases in α in the same azimuthal ranges, as presented in Figures 4.5 and 4.7. Any increase in α would result in a slight increase in lift and, as a result, an increase in torque. This may also show a slight delay between the increase in α and the subsequent increase in torque, which again may be due to the inertia of the rotor.

4.1.7 Five-Hole Probe Experimental Summary

The five-hole probe experiments described in this thesis resulted in successful measurements of the angle of attack and span-wise flow angle at the leading edge of the wind turbine blade as a function of the tip speed ratio, λ, the yaw-offset position, γ, and the radial location, r/R. Angle of attack trends matched the velocity relationships described in Section 2.1.1, as well as results presented by Maeda and Kawabuchi [21] and values calculated using models described by Burton *et al.* [2] and Morote [13]. These results indicate the potential for the innovative in-blade five-hole probe and DAQ system as an experimental tool for measuring the angle of attack and validating theoretical models for different blade designs.

A method described by Petersen *et al.* [30] was used to characterize the upstream flow using angle of attack measurements. While the calculated upstream flow speed was in close agreement with the expected values, the calculated axial induction factors did not match the values predicted using PROPID [9] or the values used to generate the accurate models presented. It was posited that this was due to a lack of lift and drag data for the wind turbine blade in the narrow range of Reynolds numbers tested.

Span-wise flow angle measurements showed an increase in magnitude with a decreasing λ, as well as an upward flow over the test-blade while the turbine was in operation. As the turbine was yawed, the span-wise flow angle was found to oscillate, reaching maximum and minimum values when the blade was oriented horizontally away and toward the wind,

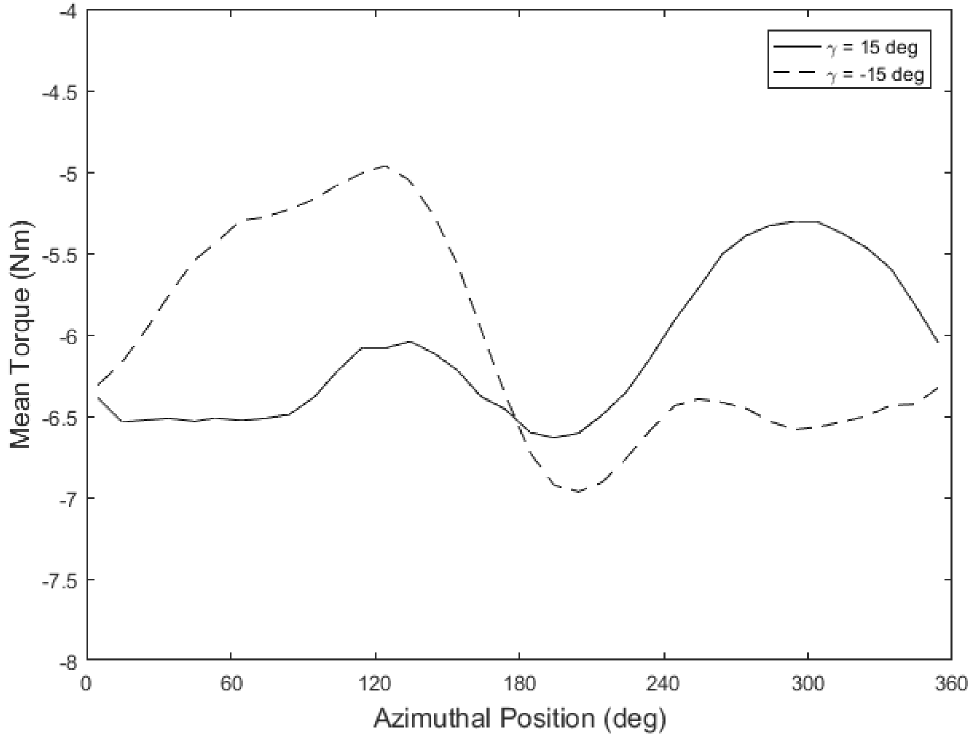

Figure 4.31: Measured shaft torque distribution at $\lambda = 3.1$, $\gamma = \pm 15°$

respectively. This was explained using the geometry of the flow and matches the spanwise flow interference described by Morote [13]. Despite the observed variations with yaw-offset, the measured shaft torque was shown to be relatively constant with azimuthal position throughout all tests, only increasing as the flow speed was increased.

4.2 Tuft Flow Visualization Results

While the variation in wind turbine blade angle of attack is of interest for several different reasons, one key issue associated with high angles of attack is flow separation and stall. To quantify the variation and distribution of stall over a wind turbine blade, tuft flow visualization experiments were conducted at the University of Waterloo Wind Generation Research Facility using the Wind Energy Group test turbine. The wind turbine blades from the five-hole experiments were replaced with three tapered and twisted blades described by Gertz [11]. Stall formation was observed as a function of the tip speed ratio, λ, the yaw angle, γ, the radial location, r/R, and the azimuthal position, ψ. Digital image processing was used to convert qualitative video to quantitative results, as described in Section 3.4.3.

In this section, stall fraction measurements made at the various test conditions will be presented. A comparison of angle of attack and stall fraction measurements made in the same range of tip speed ratios is also presented for context. The results of the modified algorithm described in Section 3.4.3 are then presented, including interpolated flow direction maps over the wind turbine blade, and histograms of tuft orientations at specific points of interest over the blade.

4.2.1 Stall Fraction Measurements

The original design of the Swytink-Binnema and Johnson [36] algorithm analyzed tuft flow visualization video to determine the stall fraction, ζ, in each frame, defined as the number of tufts indicating stall over the total amount of tufts recognized in the frame (see Section Section 2.3.2). This calculation was repeated in the modified version of the algorithm described in Section 3.4.3 using individualized stall criteria for every tuft [3]. Stall fraction results as a function of λ and ψ for experiments conducted at a 0° yaw are presented in Figure 4.32.

Stall fraction measurements in Figure 4.32 show that ζ is relatively constant with azimuthal position in axial flow, with some increased values occurring in the azimuthal range of 0° to 180°. Given that the stall formation on a wind turbine blade is directly related to the angle of attack over the blade, these results should be expected given the α measurements (made using a different blade) presented in Section 4.1.2, which also showed constant values throughout the blade rotation except for increased values in the $\psi = 50°$ to 150° range. Also similar to the α distributions, the measured stall fraction increases consistently with a decreasing λ (or increasing wind speed). The relative change in ζ also increases with each incremental decrease in λ, ranging from 20% stall to 65% stall. The increasing relative difference between ζ values will be discussed later in this section.

Comparing the stall fraction measurements from these experiments to measurements presented by Swytink-Binnema [38] on an outdoor wind turbine, a significant difference is observed. At the lowest wind speed tested, the average ζ measured on the test turbine blade was approximately 20%, whereas Swytink-Binnema measured a minimum of roughly 5% to 10% at a similar wind speed. At the maximum tip speed ratio of $\lambda = 3.2$ (which

---

[3] Presented at CANCAM 2015, June 1, 2015

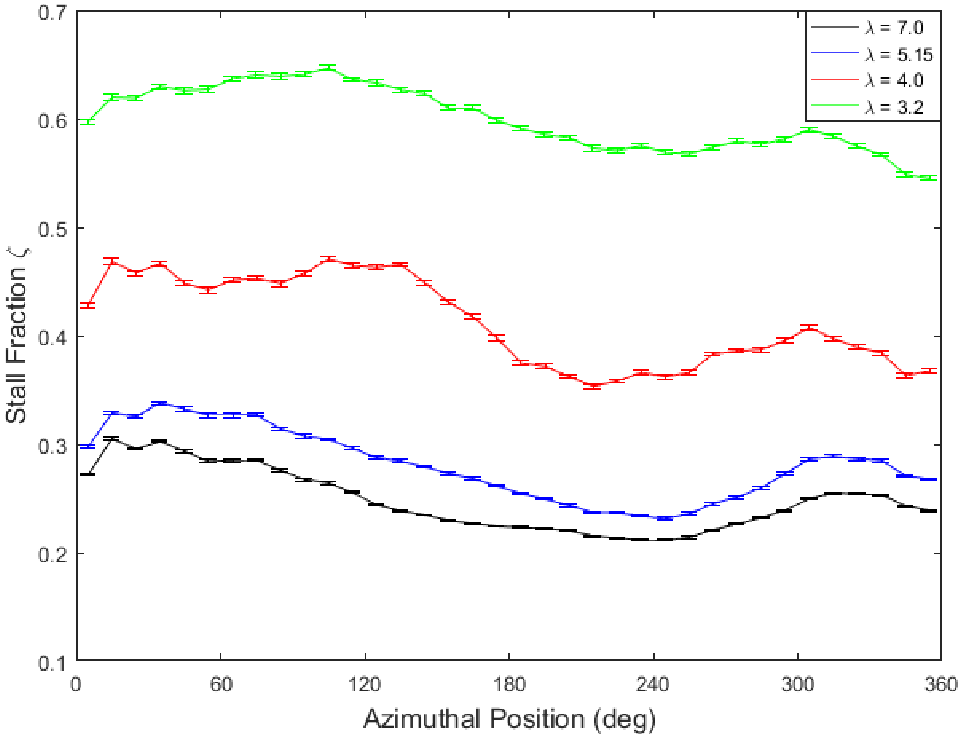

Figure 4.32: Measured stall fraction distribution at $\gamma = 0°$

corresponds to a U_∞ of 19.6 m/s for the Swytink-Binnema [38] plots), the stall fraction observed on the test turbine was 65%, compared to roughly 40% measured by Swytink-Binnema.

Trends measured here are therefore skewing towards a higher stall fraction than measured in the literature. However, it should be noted that the test turbine used here was significantly smaller, with more than half of the blade covered by tufts. In the results published by Swytink-Binnema [38], only the outer 40% of the blade was used in calculating the results. For the measurements presented here, approximately 60% of the blade was in the area of interest. Given the greater coverage, as well as the significantly shorter blade length used, the tuft coverage area is relatively much closer to the blade root. As was established in Section 4.1.2, the angle of attack increases significantly with a decreasing r/R, which would indicate that the angles of attack represented by the area of interest in the test case here were significantly higher than those in the area of interest for the

Swytink-Binnema [38] experiments. This explains the greater values of stall fraction ζ measured in these experiments. For example, in the $\lambda = 3.1$, $\gamma = 0°$ case, examining only the outer 40% of the blade reduces the average stall fraction from roughly 32% to 24%.

Reviewing the measured blade performance presented by Gertz [11] presented in Figure 3.16, the stall fraction measured here is in close agreement with the expected aerodynamic performance. The measured power coefficient was at a maximum value at approximately $\lambda = 7$, which corresponds to the lowest stall fraction measured. As the tip speed ratio is decreased to the design speed $\lambda = 5.15$, the performance decreased by roughly 5%, while the stall fraction presented in Figure 4.32 increased slightly. The changes in ζ and in C_p grow more significant as λ is decreased to 4.0 and 3.2. As stated in Section 3.4.1, the performance at $\lambda = 3.2$ is roughly one-third of the peak performance, showing significant stall over the wind turbine blade. This corresponds with the measured maximum ζ of roughly 60% which, while possibly overpredicted as discussed, reflects a significant increase in flow separation relative to the design condition.

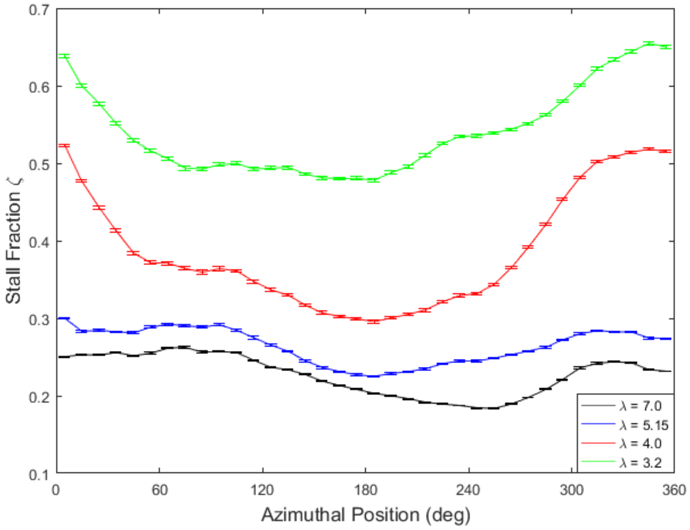

Figure 4.33: Measured stall fraction distribution at $\gamma = 15°$

As the five-hole probe measurements showed in the previous section, the angle of attack of the blade oscillates as the blade rotates when the wind turbine operates in a yawed case. This dependence is also recognizable in the stall fraction results when the turbine operates at a ±15°yaw-offset. ζ measurements at +15° and -15° yaw are presented in Figures 4.33 and 4.34, respectively.

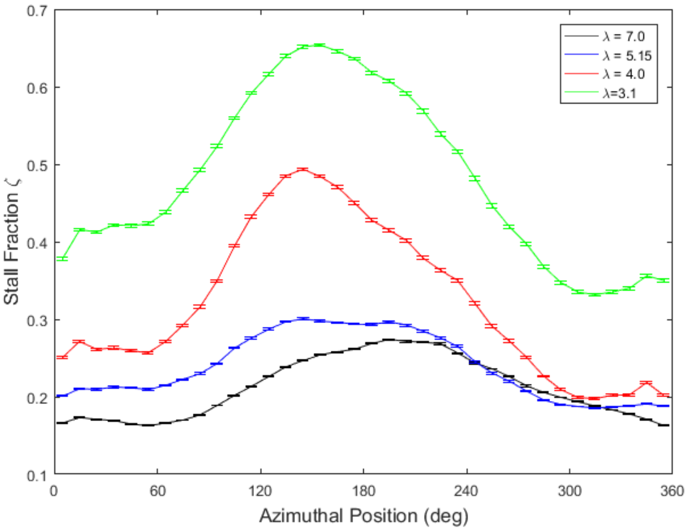

Figure 4.34: Measured stall fraction distribution at γ = -15°

Looking at Figure 4.33 first, the azimuthal variation in ζ is evident, with maximum values occurring near $\psi = 0°$ and minimum values occurring closer to $\psi = 180°$. This oscillation is most apparent at $\lambda = 4.0$ and 3.2 where the stall fraction has the greatest range, and it matches the oscillation in the angle of attack measured and plotted in Figures 4.8 and 4.5. Similar to the case with axial flow in Figure 4.32, the relative increase in stall increases with each decrease in λ. When the turbine is yawed the opposite direction, as in Figure 4.34, the stall fraction is seen to vary azimuthally in the same way as in Figure 4.33, but shifted by 180°.

The non-uniformity apparent in the α measurements in the previous section is present in the stall results shown here at $\lambda = 4.0$ and 3.2, characterized by the maximum ζ value at $\psi = 150°$. The change in the azimuthal distribution of ζ as a function of the yaw-offset is more apparent in Figure 4.35, which presents the stall fraction distribution measured at $\lambda = 4.0$ for yaw-offset positions of γ = -15°, 0°, and +15°.

The results of Figure 4.35 provide an example of the variation in stall fraction observed with variations in yaw-offset. $\lambda = 4.0$ was used here because it shows an extreme variation. At $\gamma = 0°$, the stall fraction is shown to vary within a 20% range with azimuthal position, with a peak at approximately $\psi = 120°$. As will be discussed in Section 4.2.2, these measurements closely match the $\gamma = 0°$ plots presented for the five-hole probe α measurements, indicating that the increased stall fraction at $\psi = 120°$ is likely caused by

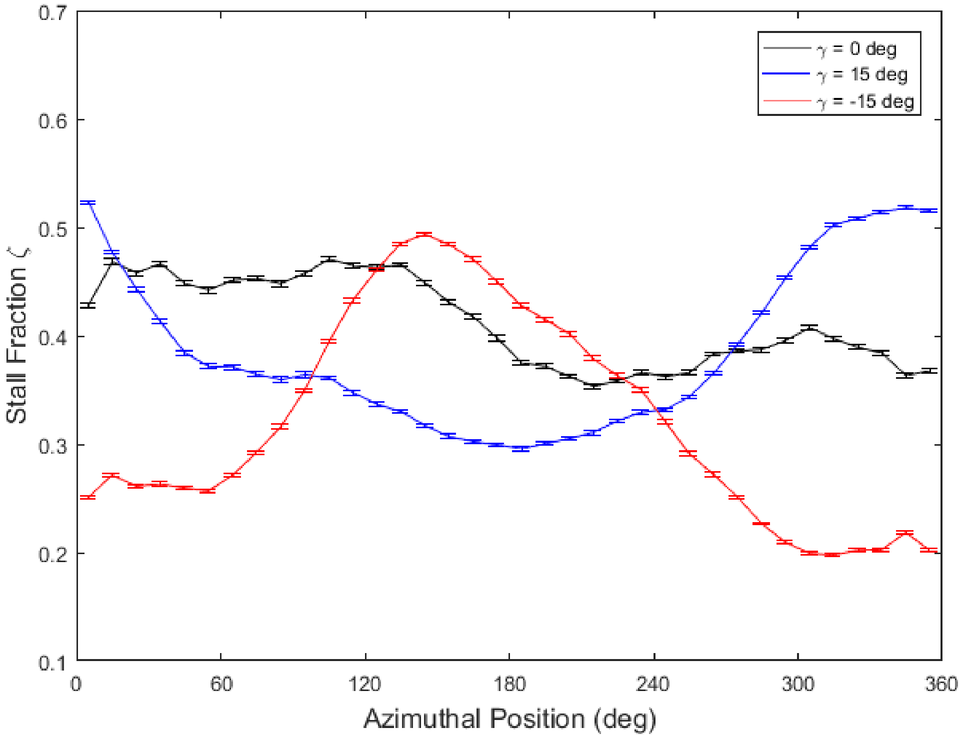

Figure 4.35: Variation in Stall Fraction distribution with yaw at $\lambda = 4.0$

the same flow non-uniformity.

When the test turbine is yawed 15°, the stall fraction begins to cycle once per revolution, with a maximum at $\psi = 0^\circ$ when the blade rotates away from the wind, and a minimum at approximately $\psi = 180^\circ$ when the blade rotates towards the wind. The opposite occurs at γ = -15°, which again corresponds to azimuthal variations in the angle of attack with the turbine in yawed conditions, as presented in Section 4.1.2. This demonstrates the close relationship between the angle of attack and stall over the blade described in Section 2.1.1.

Comparing the $\gamma = \pm 15^\circ$ plots with azimuthal position, it is observed that the two are separated by roughly $\zeta = 25\%$ at $\psi = 0^\circ$, but this gap is decreased to a change in ζ of roughly 15% near $\psi = 180^\circ$. This is unexpected in comparison to the angle of attack measurements presented in Section 4.1.2, in which the azimuthal variations between $\gamma = \pm 15^\circ$ were observed to be symmetric. It is unlikely that this skew reflects the reality of most wind turbines, but rather it is thought that it is caused by a combination of measurement errors and flow non-uniformities. These may include uncertainty in the azimuthal position bins resulting in slightly different data sorting between the three tests, or variations in video quality at $\psi = 180^\circ$, as deficiencies in lighting may result in lower tuft recognition and a bias towards higher ζ values.

The uncertainty in the stall fraction plots shown to this point only includes the precision uncertainty defined by Equation (B.2), which was consistently shown to be less than ±0.01. This indicates that the variation in the measured ζ fraction over the large number of samples was small relative to the number of samples. However, when the bias uncertainty was calculated using Equation (3.1), the results indicated that the bias uncertainty was on the same scale of magnitude as the stall fraction itself. This is because the bias uncertainty equation, defined by Swytink-Binnema and Johnson [36], accounts for the bias of the stall fraction equation to overpredict ζ when fewer tufts are recognized on the blade. For example, if 20 tufts are recognized as stalled out of a total 45 tufts, the stall fraction will be smaller compared to when 20 tufts indicate stall out of a total 30 tufts.

A side-effect of this bias is that, as the tip speed ratio decreases and the turbine blades vibrate more (due to the non-uniform flow field presented in Figure 4.19), the tuft video becomes less clear due to the exposure time of the camera. Less tufts are then recognized in the video, resulting in more significant over-estimations of the stall fraction. This effect is summarized in Table 4.5, which lists the average stall fraction and number of tufts recognized for each test configuration. While ζ would increase as λ decreased even with a constant value of n, the influence of the decreasing number of tufts recognized must be acknowledged. Note that because it is an average value, the numbers presented for n are not necessarily integers.

Table 4.5: Summary of average ζ values and corresponding number of tufts recognized (where $n_{max} = 45$

	$\gamma = 0°$		$\gamma = 15°$		$\gamma =$ -15°	
λ	ζ	n	ζ	n	ζ	n
7.00	0.24	35.7	0.23	32.5	0.26	36.6
5.15	0.27	33.5	0.27	30.0	0.19	34.9
4.00	0.37	28.8	0.51	22.0	0.20	24.7
3.20	0.54	27.5	0.65	24.2	0.35	25.5

Table 4.5 demonstrates a problem with the use of the stall fraction as an indication of stall formation over the blade. The stall fraction calculated depends on both the number of tufts recognized, as well as which tufts were recognized. For example, less tufts were recognized at $\gamma =$ -15°, but this resulted in a decreased ζ. This was likely due to tufts in the stalled region of the blade vibrating, not being recognized by the camera, and therefore skewing the stall fraction to lower values. In Section 4.2.3, the stall will be examined instead by looking at the average orientation of each individual tuft as a function of the azimuthal position. In this way, thousands of data points for each individual tuft will still be considered, but the fraction of tufts recognized in each individual frame becomes less significant. In this way, the uncertainty in the stall formation over the blade can be significantly reduced.

4.2.2 Comparison of Stall Fraction Results to α Measurements

In the previous section, the close relationship between α and stall development over the blade was discussed, with references to the theory presented in Section 2.1.1. However, it may be difficult to visualize the link between the two when they are presented in separate plots and sections of this thesis. For clarification, plots showing the azimuthal variation in both α and ζ measurements conducted are presented in this section. Values at $\lambda = 3.5$ and $\lambda = 3.2$ were used for the α and ζ measurements, respectively, as the two tip speed ratios were near enough to each other to be representative, while also providing the most significant azimuthal variations of the various λ values tested. Results at a yaw-offset of 0°, 15° and -15° are plotted in Figures 4.36, 4.37 and 4.38, respectively. Please note that these plots are only for the purpose of demonstrating the azimuthal trends, as α measurements presented are from $r/R = 0.55$ only, and from a different wind turbine blade. These plots cannot be used to estimate the critical angle of attack over the length of the blade.

Beginning with the axial results, some azimuthal variation is observable for both the stall fraction and the angle of attack. As was established in Section 4.1.2, the peak in α between $\psi = 100°$ and $150°$ can be attributed to a non-uniformity in the flow field. Overlaying the two variables shows that this non-uniformity influences the stall fraction as well, with ζ peaking at approximately $\psi = 100°$. As the blade rotates past the flow non-uniformity, the angle of attack decreases over the blade, which results in a diminished stall fraction. The shape of the curve for the two variables is nearly identical for azimuthal locations of $\psi = 100°$ to $360°$.

From $\psi = 0°$ to $100°$, ζ and α are both increasing, but the angle of attack increases significantly more throughout this period of rotation. The differences in this small portion of the rotation may be attributed to stall delay. At a rotational speed of 200 rpm, the wind turbine blade travels the 100° distance in less than 0.1 seconds. Therefore, while the angle of attack is varying quickly, the actual air flow over the blade may be experiencing a form of stall delay, in that the change in α is so rapid that the air flow does not have time to reattach and reduce the blade stall before α increases and the flow separates again. This form of hysteresis is not uncommon in cases of dynamic stall when a vortex is shed from the leading edge of the airfoil after a sudden change in α. Of course, it is important to note again that these measurements were conducted on two separate rotors at different points in time, and therefore any comparison between the two will involve some inherent uncertainty or error. The apparent agreement between results may be varied simply by changing the scale of the axes presented.

The same phenomenon is demonstrated when the test turbine is yawed 15°as in Figure 4.37. Here, the azimuthal variation of both ζ and α becomes more exaggerated. As the blade rotates towards and away from the upstream wind, α varies due to the changing velocity geometry, as discussed in Section 4.1.2 and Figure 4.6. The close agreement between the ζ and α curves presented here demonstrate that the stall development on the blade follows the same trends as α. As the angle of attack increases over the blade, a larger portion of the blade will surpass $\alpha_{critical}$, causing flow separation. As the blade rotates towards the wind and α decreases, it causes a similar decrease in stall over the blade.

However, while the angle of attack and stall fraction again follow similar trends throughout the blade rotation, their cycles are not perfectly matched. While the angle of attack value varies significantly from $\psi = 60°$ to $180°$, the stall fraction reaches a constant minimum between the same positions. However, between $\psi = 60°$ and $120°$, the both ζ and α are relatively constant. The sharp decrease in α only occurs over a total of 60° of rotation before both α and ζ begin rising steadily through the downward rotation of the blade. Assuming the same variation in α occurred during testing with the Gertz [11] blades, the constant ζ in this region could be attributed to a delay in the flow condition bridging the

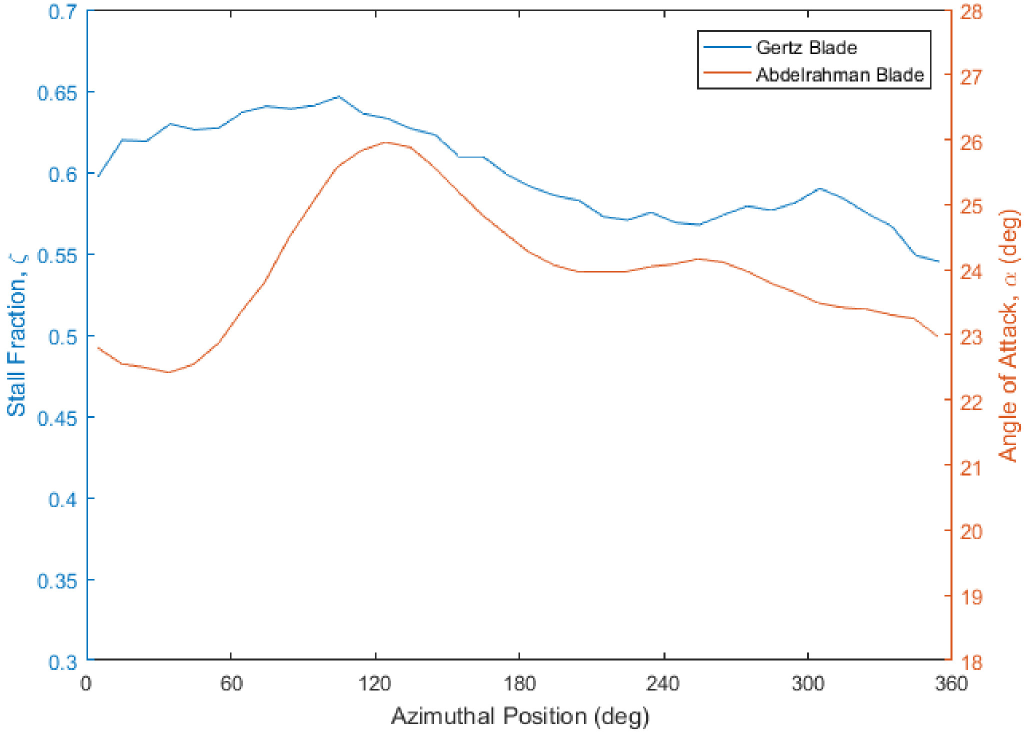

Figure 4.36: Comparison of azimuthal variation between measured α and ζ values at , $\gamma = 0°$, $\lambda = 3.5$ and 3.2, respectively, using Gertz [11] and Abdelrahman [10] blades.

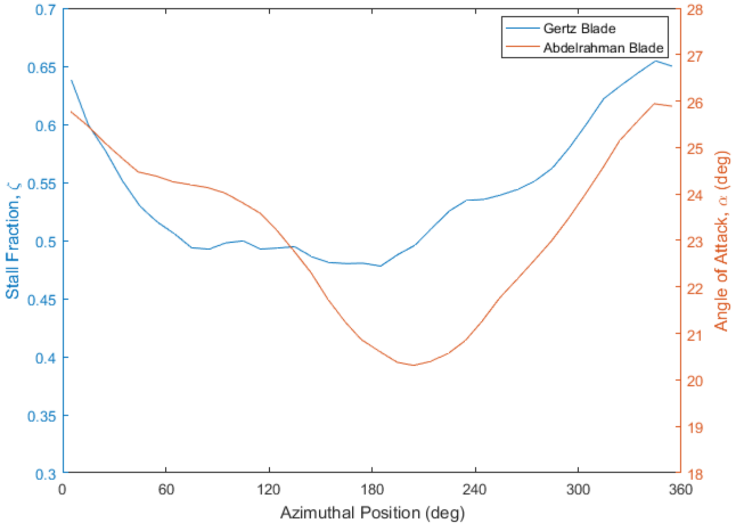

Figure 4.37: Comparison of azimuthal variation between measured α and ζ values at , γ = 15°, λ = 3.5 and 3.2, respectively, using Gertz [11] and Abdelrahman [10] blades

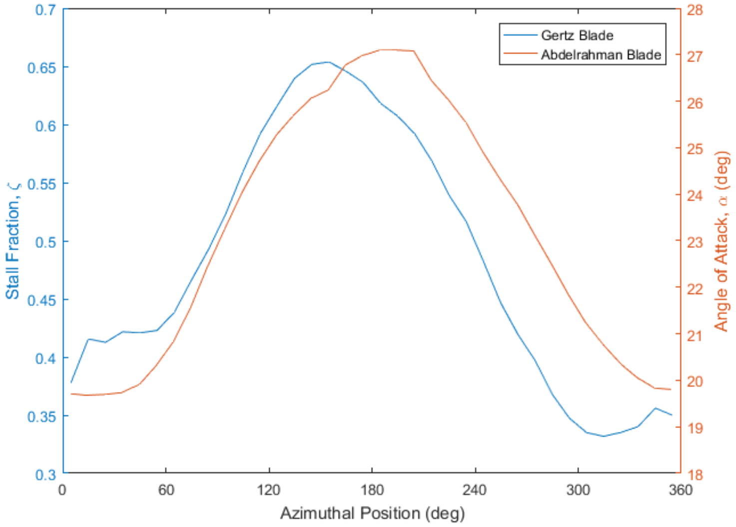

Figure 4.38: Comparison of azimuthal variation between measured α and ζ values at , γ = -15°, λ = 3.5 and 3.2, respectively, using Gertz [11] and Abdelrahman [10] blades

gap between a constant and rising α.

Angle of attack and stall fraction measurements at γ = -15° are presented in Figure 4.38. This plot follows the same overall trends as Figure 4.37; both α and ζ increase as the blade rotates away from the wind and decrease as the blade rotates towards the wind. However, unlike the other two cases presented, the two sets of measurements are in almost perfect agreement. This may due to a lack of measured disturbance during either set of tests, resulting in a case following the theoretical ideal. Results in Figure 4.38 appear to show that the average angle of attack of the Gertz [11] blade decreased earlier in the rotation than the α measured at a single radial location of the Abdelrahman [10] blade, resulting in the ζ curve leading α between ψ = 180° and 360°.

4.2.3 Tuft Interpolation Results

Using the method described in Section 3.4.3, the orientation of each tuft recognized in each frame was measured and logged for future analysis. Using this data, the average orientation of each tuft was calculated for the complete rotation, as well as throughout several azimuthal position bins for examining the variation in stall distribution. In both cases, MatLab [61] was used to generate a grid map between the tuft coordinates. Tuft orientations were then interpolated throughout the grid to generate a contour map of the average tuft orientation over the full blade surface within the tuft placement boundaries.

Averaged Results

Angle of attack measurements in axial flow conditions (as presented in Section 4.1.2) showed that α remained nearly constant with azimuthal position. Using this insight, stall distributions measured during axial flow were averaged throughout the full rotation and plotted as a function of the tip speed ratio only. Absolute values of tuft orientations were used when calculating the average to avoid erroneously calculating an average 0° tuft orientation for a tuft which was rapidly oscillating between extreme positive and negative values. As was established by the five-hole probe measurements, α increases with each decrement in λ, which would have a direct influence on the formation of stall over the blade. Tuft orientation maps at λ = 7.0, 5.15, 4.0 and 3.2 are presented in Figure 4.39.

In the tuft orientation maps presented, the direction of flow is assumed to be approximately from leading edge to trailing ledge, or left to right. Therefore, attached flow is typically judged to be tuft orientations of approximately 0°to 15°. In practice, such tuft

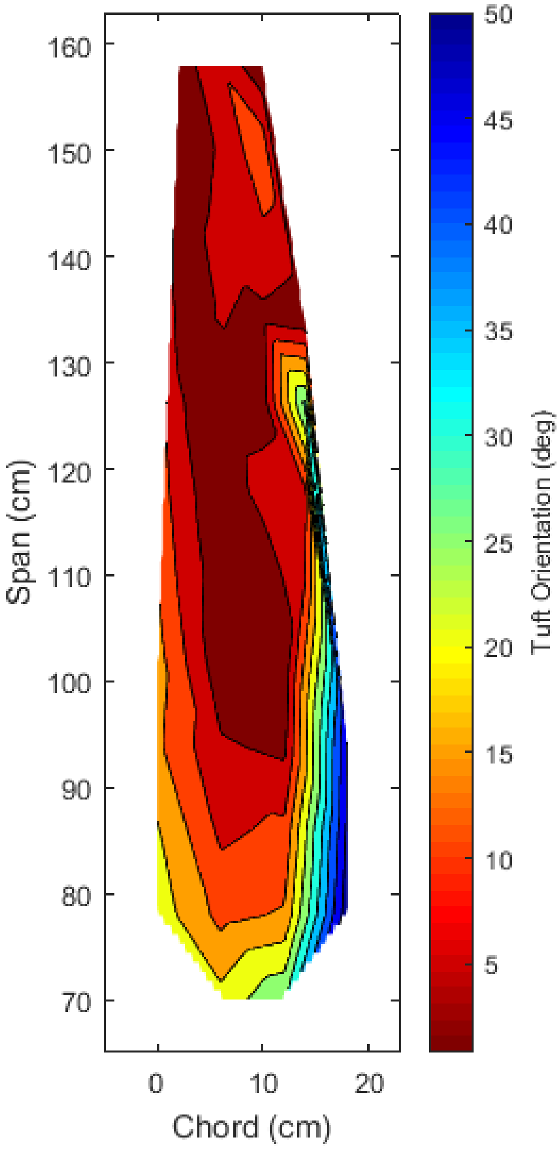
Span (cm)
160
150
140
130
120
110
100
90
80
70
0
10
20
Chord (cm)
50
45
40
35
30
25
20
15
10
5
Tuft Orientation (deg)

(a)

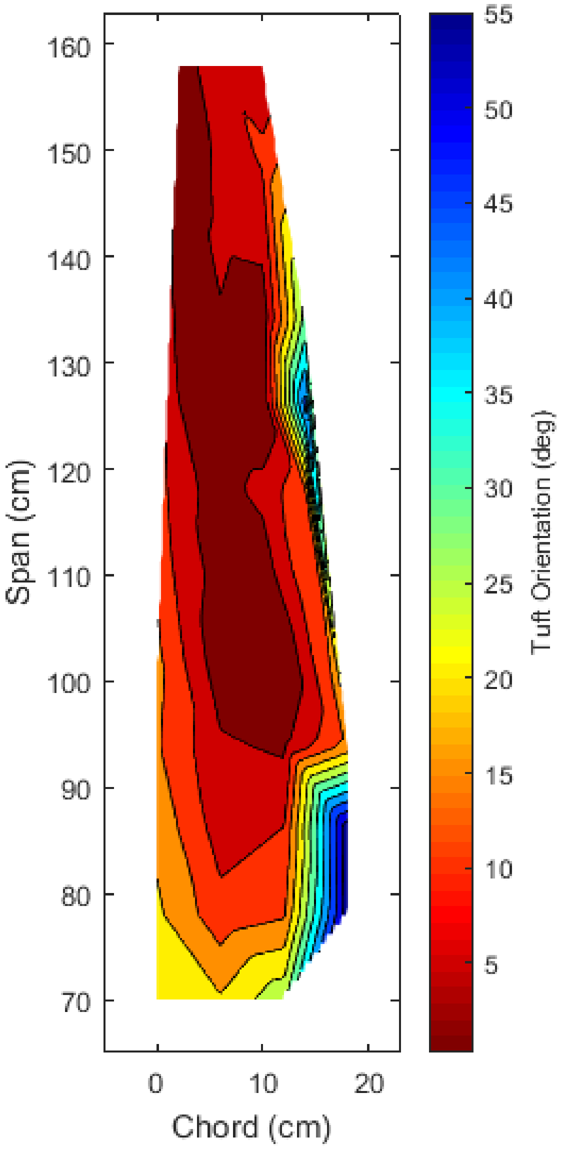
Span (cm)
160
150
140
130
120
110
100
90
80
70
0
10
20
Chord (cm)
55
50
45
40
35
30
25
20
15
10
5
Tuft Orientation (deg)

(b)

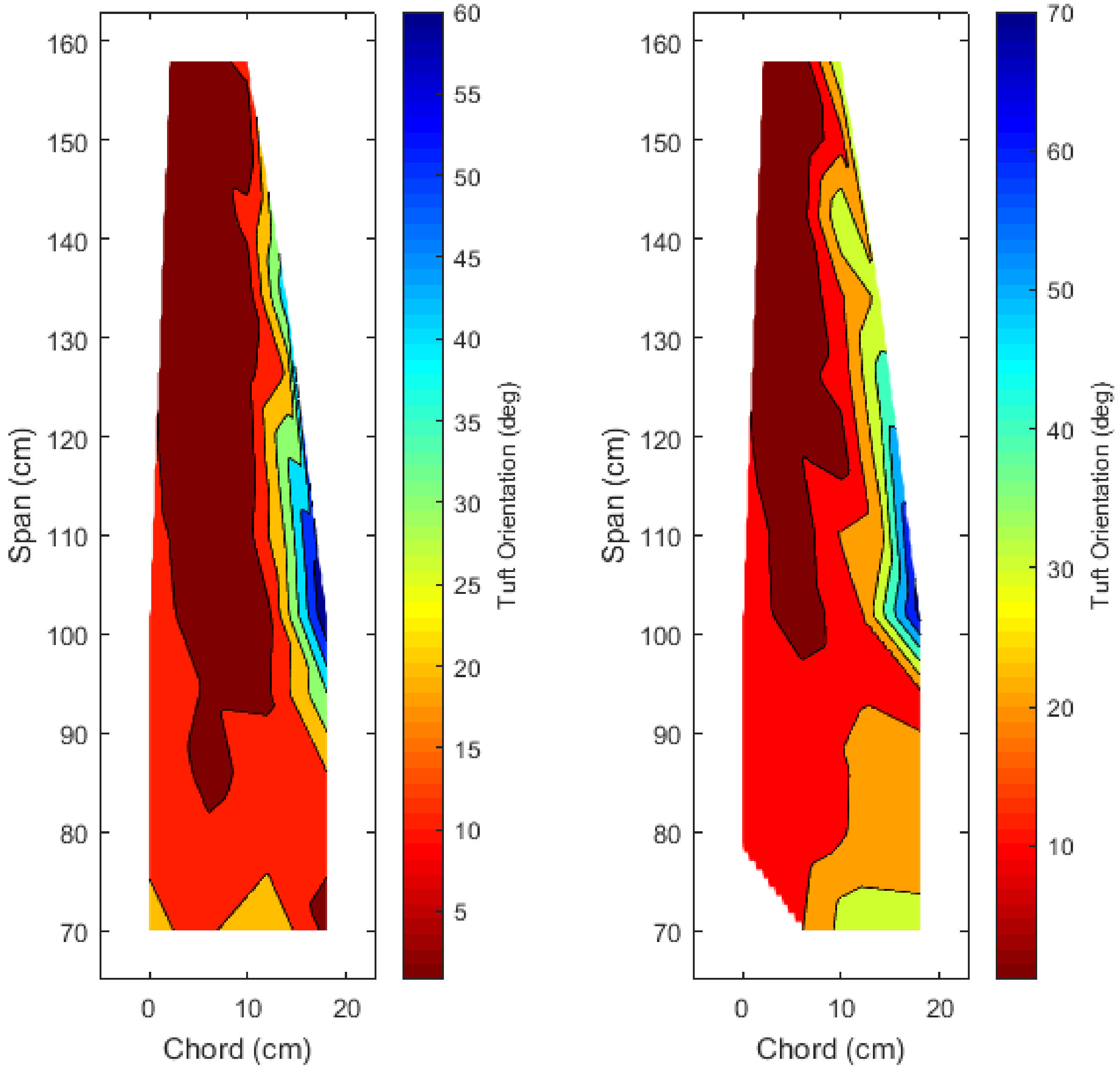

(c) (d)

Figure 4.39: Average Tuft Orientation Map at $\gamma = 0°$ at (a) $\lambda = 7.0$ (b) $\lambda = 5.15$ (c) $\lambda = 4.0$ (d) $\lambda = 3.2$. Flow is left to right. Attached tufts are judged to be those with a tuft orientation of 0° to 15°.

orientation maps provide a qualitative look at the flow direction over the blade and how it varies with λ, γ and ψ.

With this in mind, an examination of the tuft orientation maps in Figure 4.39 consistently show tufts aligned with the flow direction over the leading half of the blade. The trailing edge tends to have tufts oriented away from the flow direction (*e.g.* ±20-50°), which would indicate that the centrifugal forces or turbulence tend to dominate at the trailing edge. Such orientation is indicative of stall, and throughout the four plots, the distribution of tufts oriented away from the attached region of 0° to 15° tends to grow from the trailing edge as the wind speed increases and λ decreases.

Before examining the interpolated results presented in this section, it may be a helpful reminder to review the tuft layout over the blade presented in Figure 3.17. Tufts were placed approximately 4 to 6 cm apart in the chordwise direction and 8 cm in the spanwise direction. The tuft layout map may be helpful in understanding the placement of tufts within the interpolated map. The orientations of tufts on the blade were interpolated over 10,000 points, and the orientation of a single tuft may therefore have a significant influence on the interpolated map between that tuft and those surrounding it. An example of this can be seen at the trailing edge of the inboard blade section (chord, span) = (17 cm, 80 cm) in Figure 4.39b, where the extreme orientations of two tufts at the trailing edge resulted in a region labeled with tuft orientations indicating stall. In Figure 4.39c, 7 stalled tufts along the trailing edge of the blade from spans 80 cm to 136 cm result in a significant stalled region in the interpolated plot. Despite the large influence of limited tufts, it is posited that the linear interpolation of tuft orientations between tufts is a reasonable estimate of flow behaviour between the distinct points. The resolution of the flow orientation map could only be improved by increasing the density of the tufts placed on the blade surface, which would increase the risk of tufts becoming tangled or being recognized incorrectly by the algorithm. However, as will be discussed shortly, the uncertainty currently associated with the interpolated maps presented is considered acceptable.

At $\lambda = 7.0$, the tuft orientation map in Figure 4.39a shows some stall occurring at the trailing edge in the inboard region, but the majority of the blade surface is well within the 15° criteria for attached flow. As λ decreases, the stalled region remains close to the trailing edge, but it moves further outboard, as seen in Figures 4.39b and 4.39c. At the maximum flow speed in Figure 4.39d, the stalled region has expanded nearly halfway towards the leading edge and has also reached the trailing edge at the tip. This stall development is similar to that observed by Eggleston and Starcher [35] on the Enertech 21-5 and 44-50 wind turbines, which also used blades of a twisted and tapered design. Results observed by Swytink-Binnema and Johnson [36] were much the same when their algorithm was applied to measurements on a 30 kW wind turbine.

The variation of the stalled region over the blade can be related to angle of attack trends presented in Section 4.1.2. Firstly, as was discussed in Section 4.2.1, the area of the blade that is stalled grows with each decrease in λ and increase in wind speed, which corresponds to an increase in the angle of attack over the full length of the blade. However, unlike the stall fraction, the use of the interpolated tuft orientation map also shows where the stall is occurring. Beginning with $\lambda = 7$, the stalled region is shown to be primarily at the inboard and trailing edge regions, which correspond to areas with the largest angle of attack and turbulence, respectively. As the wind speed increases and the angle of attack over the blade increases, sections of the blade reach the critical angle of attack (and therefore stall) beginning with the inboard region, and the boundary between stalled and attached flow moves outwards towards the tip. The development of stall agrees with the angle of attack trends observed between $r/R = 0.38$, 0.55 and 0.72 presented in Section 4.1.2.

Comparing the results of the tuft orientation maps to the ζ estimations presented in Section 4.2.1, the effect of the bias inherent in the stall fraction definition is demonstrated. For example, at $\lambda = 3.2$ with a yaw-offset of $0°$, the average stall fraction was measured to be 54% (as presented in Table 4.5). However, in Figure 4.39d, it can be seen that the majority of the blade is actually experiencing attached flow according to the same tuft orientation criteria. The bias in the stall fraction is caused by calculating ζ for each individual frame, where the total number of tufts, n, measured in each frame can artificially increase the ζ if it is less than the total number of tufts. By measuring the average orientation of each individual tuft rather than the average fraction from each frame, the effect of n can be mitigated.

In three of the tuft maps presented, it should be noted that 1-2 tufts are missing at the lower portion of the tuft map (in Figures 4.39a, 4.39b and 4.39d specifically). This is caused by a tuft not being recognized by the algorithm throughout the full video analysis, and generally occurs closer to the camera where a tuft may not be completely in frame. However, the missing tufts can be used as a demonstration of the advantage of the use of a tuft orientation map for stall analysis rather than the stall fraction approach. When calculating the bias uncertainty in the calculated stall fraction, the number of tufts recognized was a key variable (as expressed in Equation (3.1)). This reflected the bias towards a higher stall fraction when fewer tufts were recognized. However, by using the average orientation of each individual tuft to generate a tuft orientation map, the only uncertainty of note is the precision uncertainty in the individual orientations.

To demonstrate the improved uncertainty, interpolated maps of the estimated precision uncertainty were created for the four plots presented in Figure 4.39. The uncertainty plots for $\gamma = 0°$ at $\lambda = 7.0$, 5.15, 4.0 and 3.2 are presented in Figure 4.40.

The uncertainty maps for the axial flow cases show that the uncertainty in the individual tuft orientations is consistently below ±8°, with the majority of points having an uncertainty of less than ±1°. Typically, tufts that correspond to a higher uncertainty value are those which were recognized in fewer frames or those which varied significantly in orientation throughout the tests, such as tufts closer inboard (as in Figure 4.40c) or tufts near the trailing edge (as in Figure 4.40d). Overall, the uncertainty maps shown here show that the modified algorithm has improved the understanding of the stall distribution and the associated uncertainty over the surface of the blade relative to results shown in Section 4.2.1.

Variation with Azimuthal Position

Given the minimal azimuthal variation in α measured in axial flow, the average tuft orientation throughout the full rotation is representative of test results in axial conditions. However when the wind turbine is yawed, the flow over the blade varies significantly, as previously demonstrated in the α measurements of Section 4.1.2. To view the effects of this oscillation on the tuft orientation maps, and ultimately the stall distribution, tuft data was sorted into 30° azimuthal position bins and averaged. The bins were bounded at -15° to +15°, 15° to 45°, etc. to ensure that example results could be averaged and plotted at the critical positions of $\psi = 0°$, 90°, 180° and 270°. The average tuft orientations at these azimuthal positions for test results measured at $\lambda = 3.2$ and $\gamma =$ -15° are plotted in Figure 4.41.

When examining the tuft orientation maps presented in Figure 4.41, it is helpful to reflect on the α measurements presented in Figures 4.9 and 4.7 for the same yaw angle. It was shown that, at $\gamma =$ -15°, the angle of attack is at a minimum when $\psi = 0°$(while the blade is in the 6 o'clock position rotating toward the wind) and at a maximum when $\psi = 180°$(while the blade is in the 12 o'clock position rotating away from the wind). The variation in α measured with the five-hole probe corresponds closely to the stall measurements presented here.

In Figure 4.41a at $\psi = 0°$(with the blade travelling towards the wind), α is at a minimum and the majority of the blade surface indicates tufts aligned with the flow, indicating limited stall. As the blade rotates towards 12 o'clock through Figures 4.41b and 4.41c and α increases, the region of stall identified at the inboard portion of the blade begins to increase. Finally, when α is at a maximum at $\psi = 180°$ in Figure 4.41c, the majority of the inboard region of the blade and trailing half appears to be stalled, with only the tip of the blade maintaining a completely attached flow. This is to be expected, as the increased angle of attack (especially in the inboard region) increases the probability of

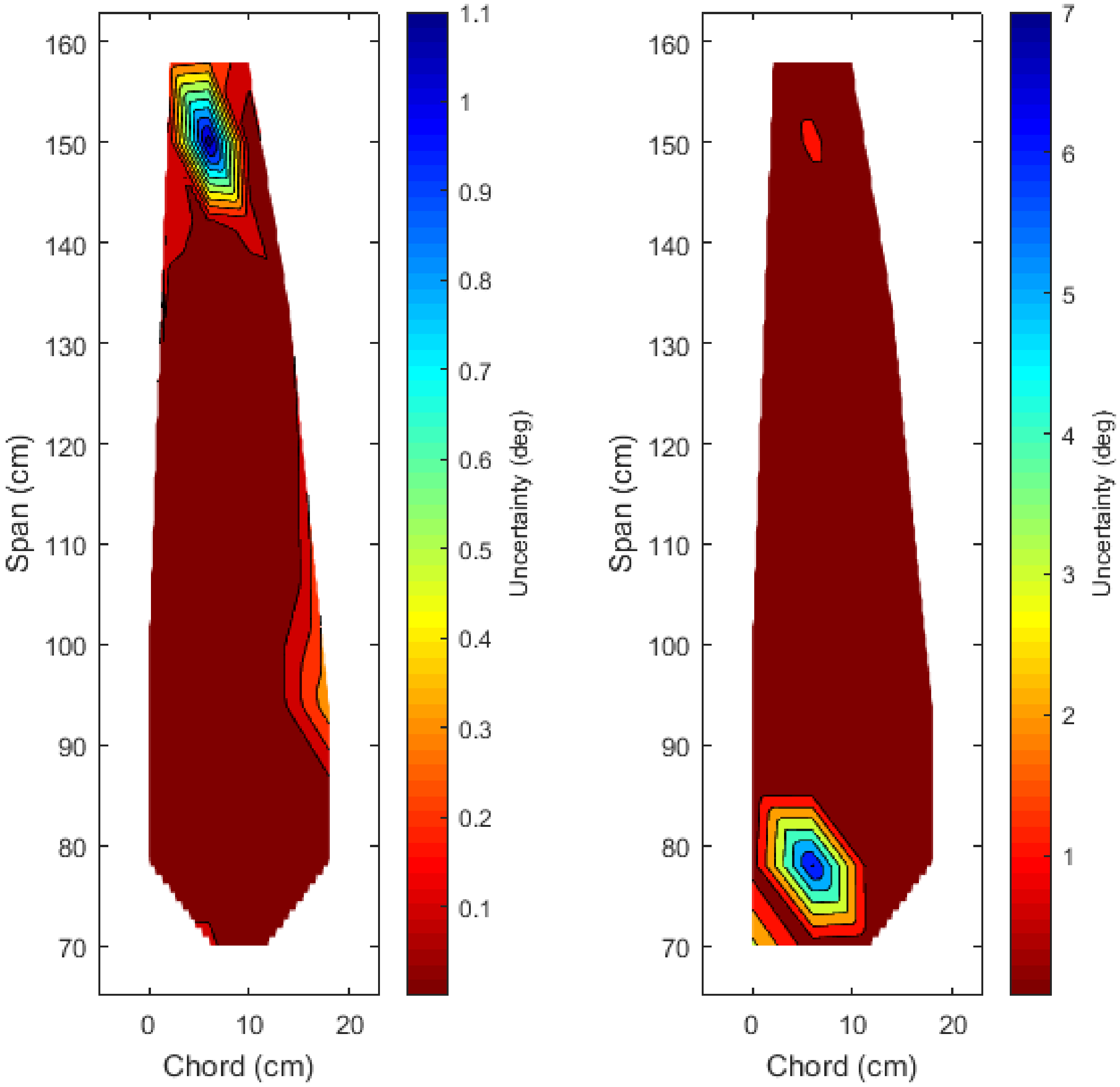
Span (cm)
160
150
140
130
120
110
100
90
80
70
0
10
20
Chord (cm)
1.1
1
0.9
0.8
0.7
0.6
0.5
0.4
0.3
0.2
0.1
Uncertainty (deg)
Span (cm)
160
150
140
130
120
110
100
90
80
70
0
10
20
Chord (cm)
7
6
5
4
3
2
1
Uncertainty (deg)

(a) (b)

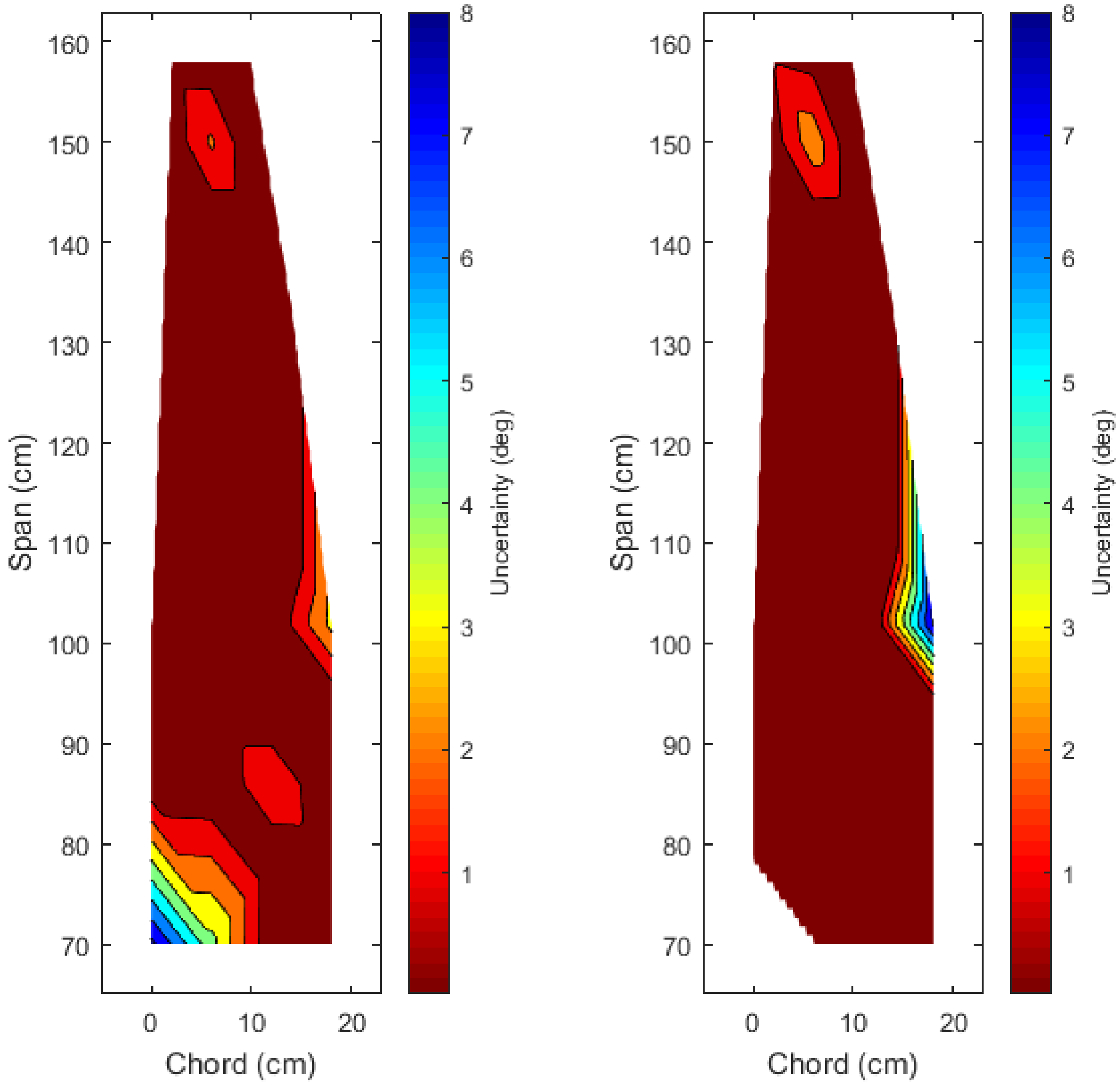

(c)

(d)

Figure 4.40: Orientation Uncertainty Map at $\gamma = 0°$ at (a) $\lambda = 7.0$ (b) $\lambda = 5.15$ (c) $\lambda = 4.0$ (d) $\lambda = 3.2$

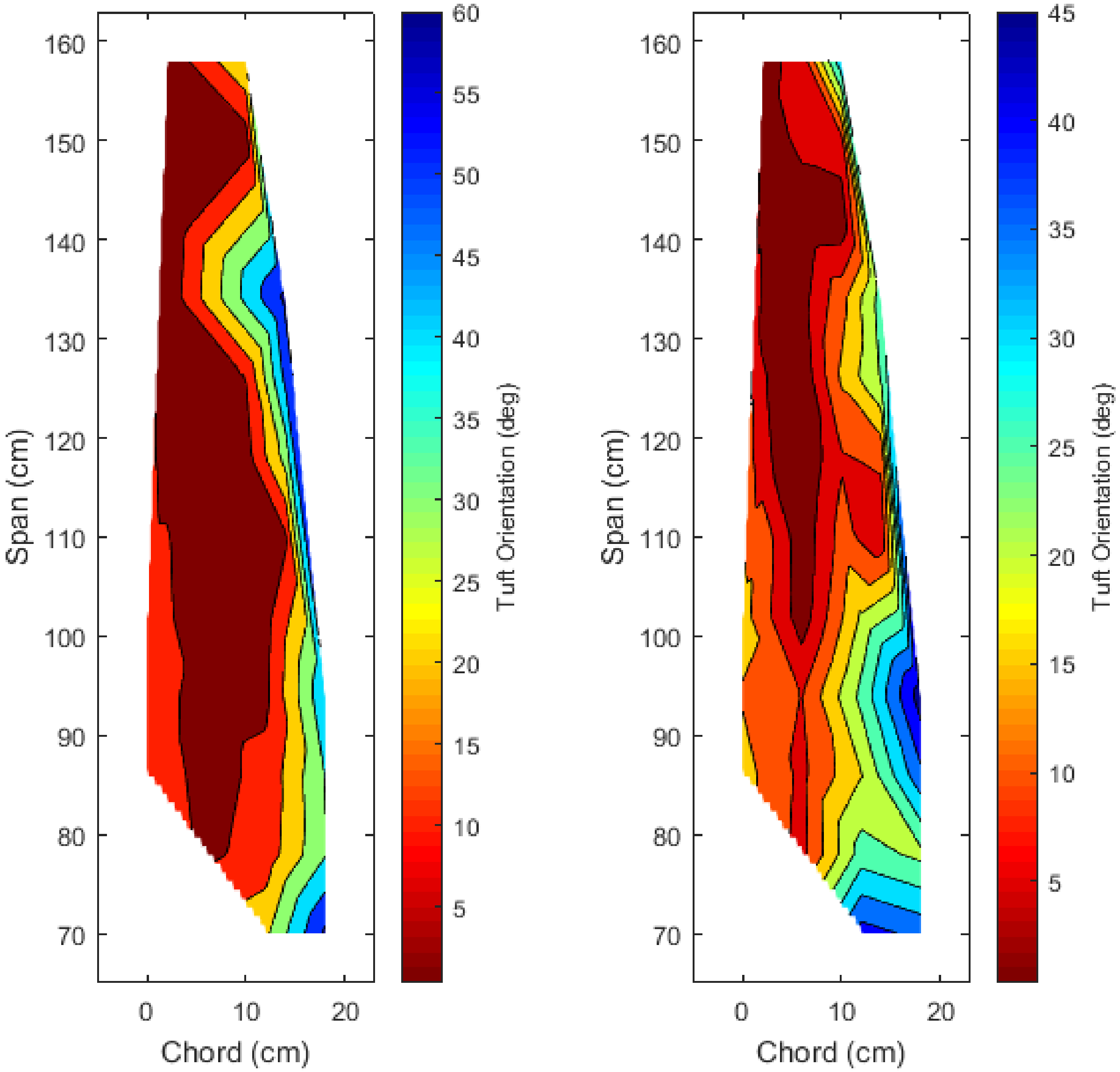

(a) $\psi = 0^{\circ}$

(b) $\psi = 90^{\circ}$

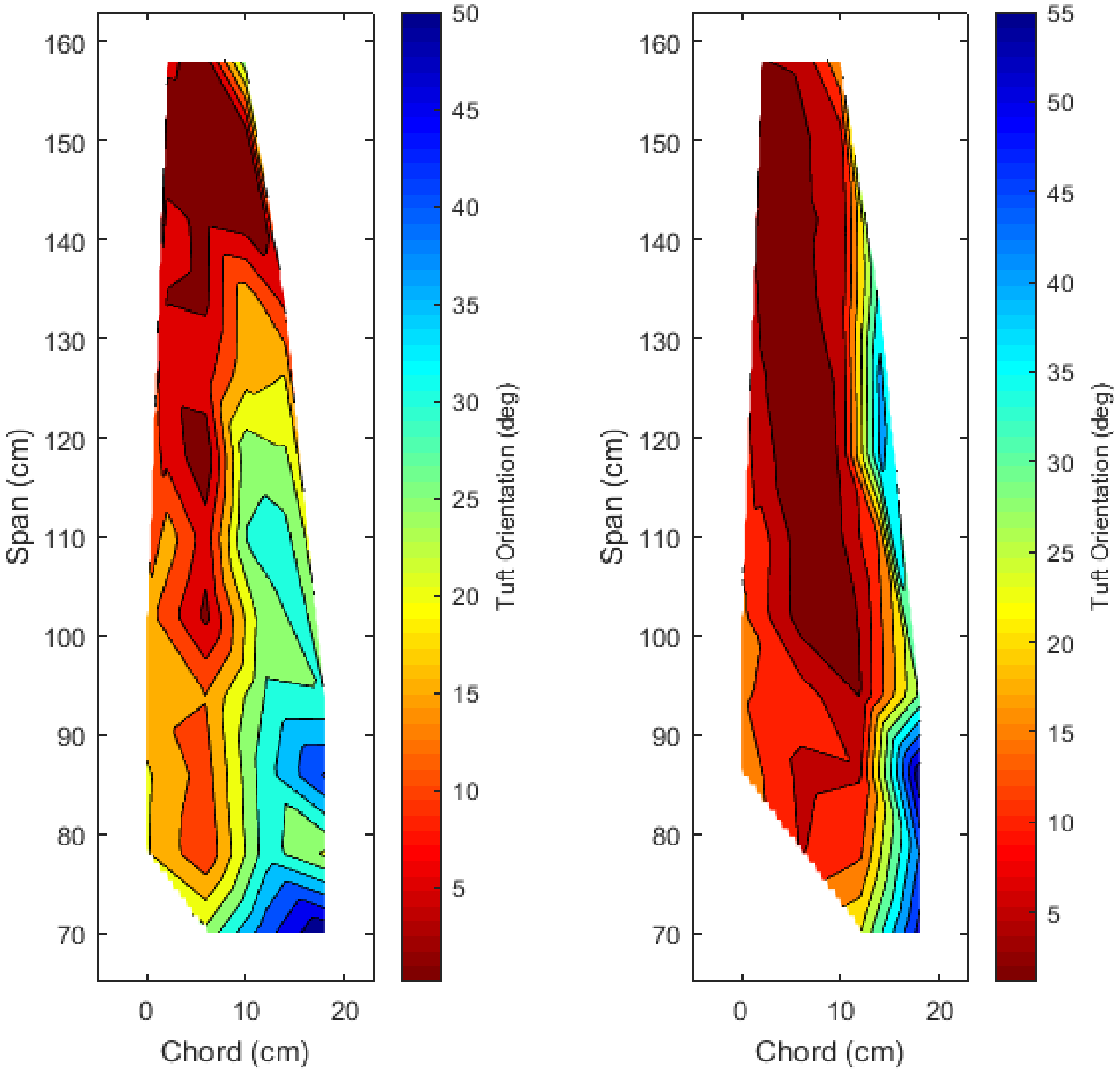

(c) ψ = 180°

(d) ψ = 270°

Figure 4.41: Average Tuft Orientation Map at λ = 3.2, γ = -15° for ψ = (a) 0°, (b) 90°, (c) 180°(d) 270°

surpassing the $\alpha_{critical}$ value described in Section 2.1.1, resulting in flow separation. By ψ = 270°, most of the tufts on the blade have returned to an aligned orientation, indicating that α has descended below the critical value.

The results plotted in Figures 4.39 through 4.41 are only a fraction of the possible plot configurations that could be generated using the individualized tuft orientation data measured during the tuft flow visualization experiments. Plots generated for the λ = 3.2, γ = -15° case are provided in Appendix H. These tuft orientation maps demonstrate the potential of the digital image processing method of analyzing tuft flow visualization data and, by extension, flow over a rotating wind turbine blade. Mapping the average flow orientation over the blade, whether over the full rotation or at specific azimuthal positions, provides an informative look at the blade-air interaction at different conditions that would not be possible without the developed digital image processing algorithm discussed in Sections 2.3.2 and 3.4.3. The results also demonstrate the successful implementation of advantages inherent in the Vey *et al.* [39] algorithm to the Swytink-Binnema and Johnson [36] algorithm.

4.2.4 Individual Tuft Results

While the average tuft orientation maps presented in the previous section are a key advantage of the modified algorithm, another benefit of logging individual tuft orientations throughout each test is the ability to look at the behaviour of specific tufts of interest throughout the test. For example, comparing tufts that are known to be in the attached or stalled regions of the flow could provide more insight into the flow behaviour in those areas. The behaviour of individual tufts is examined here through the use of histograms depicting the distribution of orientations measured for specific tufts throughout specific tests, as well as a plot of tuft orientation over time. Similar techniques were implemented by Vey *et al.* [39] for tuft orientations measured at a single azimuthal location. For clarity, a map of the tuft layout (in the same orientation as the tuft interpolation results) is presented in Figure 4.42 with the tufts of interest labeled.

Histograms depicting the behaviour of tufts # 9 and #42 in the attached and stalled regions of the blade during the λ = 3.2, γ = 0° test are presented in Figure 4.43. These tufts were selected specifically because they demonstrate the two extremes of the flow orientations that were measured at γ = 0°. Tuft #9, located near the leading edge of the outboard half of the blade, was measured to have a nearly constant orientation of 5° to 10° throughout the full test. This is a clear example of a tuft indicating attached flow, as it is nearly in line with the assumed flow direction of 0°, and it shows no influence of separation,

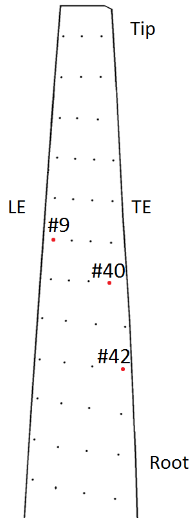

Figure 4.42: Map of tuft layout over the test blade with tufts #9, #40 and #42 labeled. See Figure 3.17

such as large variations due to turbulence. This is to be expected at this location, as α is likely to be below $\alpha_{critical}$ at this blade location, as demonstrated in the previous sections.

Tuft #42, located at the trailing edge of the inboard half of the blade, is shown to have experienced a very different flow in Figure 4.43b. The histogram plotted shows that the trailing edge tuft was not oriented with the flow direction of 0° at any point throughout the test. Rather, the tuft seems to have cycled between being oriented either inboard or outboard at angles of 270° and 90° respectively. This bimodality is similar to tuft results presented by Vey *et al.* [39], and is representative of a turbulent and separated flow state. Essentially, the tuft orientation is being controlled by turbulent flow structures and its own centrifugal inertia pulling the tuft outboard, rather than a steady flow passing over the blade.

Tuft #40 was chosen arbitrarily to demonstrate the rapid oscillation of a tuft in separated flow. Figure 4.44 presents the orientation of the tuft as a function of time for 10 seconds of data (or roughly 33 revolutions). During operation, air flow separated from the airfoil before reaching tuft #40, which left it in a low pressure, turbulent wake. The tuft then oscillated between being oriented towards the tip of the blade (*i.e.* being dominated by its outward momentum) and being oriented towards the root. It is likely that the tuft was oriented towards the root of the blade when caught by vortices travelling across the airfoil.

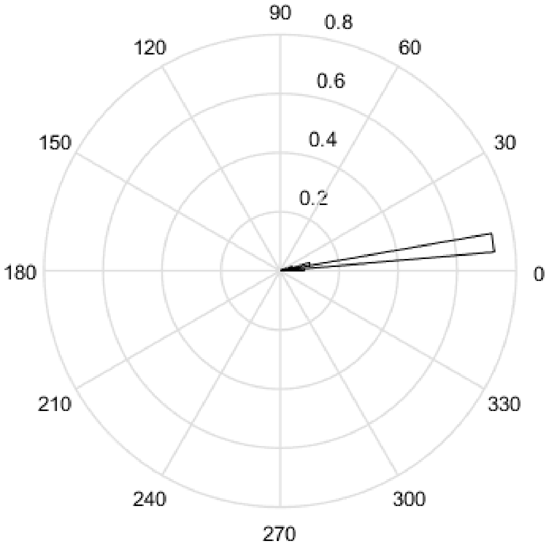

(a) Histogram of Tuft #9

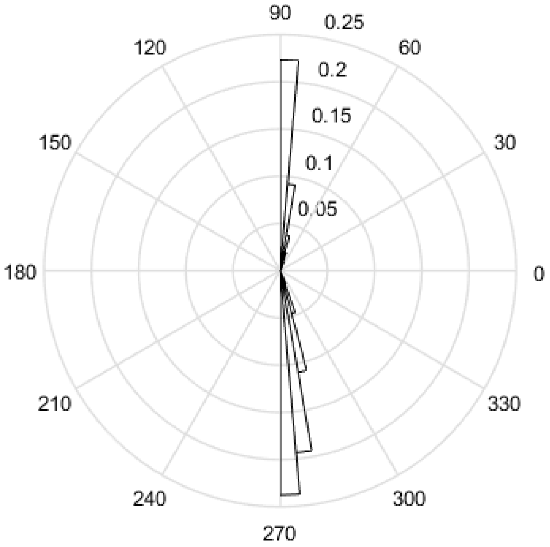

(b) Histogram of Tuft #42

Figure 4.43: Histogram of Measured Tuft Orientations for $\lambda = 3.2$, $\gamma = 0^\circ$

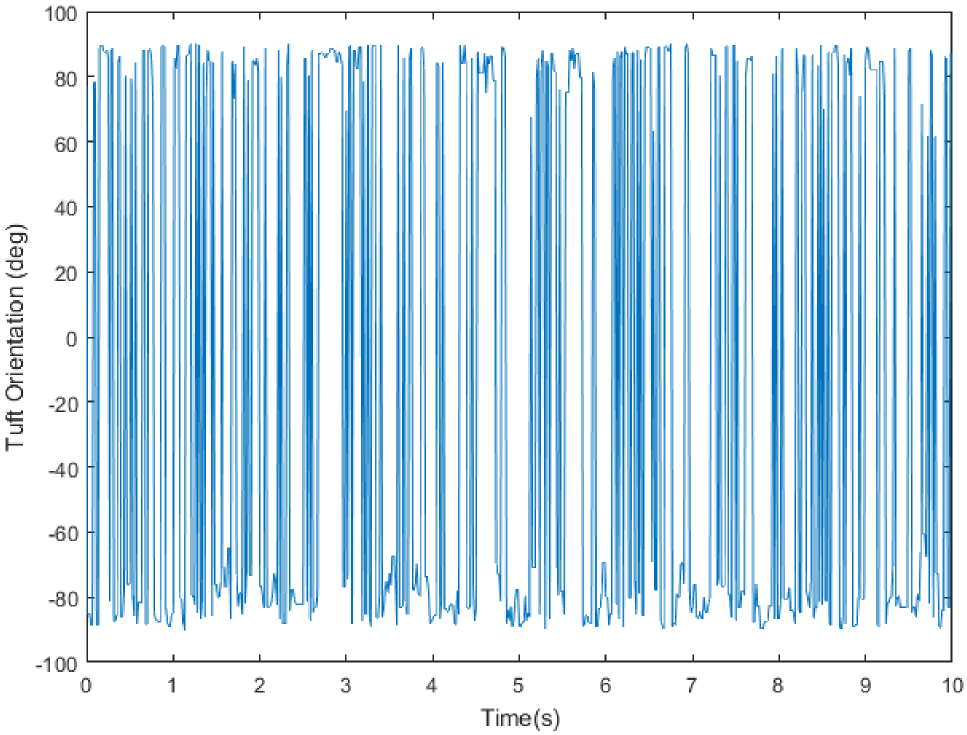

Figure 4.44: Tuft 40 orientation versus time for 10 seconds of data at $\lambda = 3.2$, $\gamma =$ -15°

The results plotted in Figure 4.43 show tufts which are clearly within attached or stalled flow regions. However, when the wind turbine is yawed, a number of tufts on the blade would likely oscillate between indicating attached and stalled flow, as was demonstrated in Figure 4.41. Tuft #42 was located at the trailing edge of the blade less than half way out of the tufted portion, in a region which varied between attached and stalled flow while rotating in yawed conditions. Figure 4.45 presents a histogram of the tuft orientation variations throughout a test at $\lambda = 3.2$, $\gamma =$ -15°.

The large variation plotted in the Figure 4.45 includes tuft orientations of ±90°, indicating that the tuft was in a separated flow region, similar to the histogram plotted in Figure 4.43. However, Figure 4.45 also shows that the tuft was oriented with the flow direction, 0°, which indicates that the tuft was within an attached flow region as well. The inclusion of stalled and attached flow positions indicates that the flow over this section of the blade repeatedly attaches and separates to the blade as it oscillates through high-and low-α conditions throughout its rotation. This may be due to dynamic stall occurring with rapid changes in the angle of attack, resulting in stall delay. As the angle of attack increases beyond the critical value, it is possible for the flow to remain attached up to greater values of α than would be possible in steady flow conditions. This may explain why up to 30% of the flow experienced by tuft #40 was attached despite operating with a consistently high α at $\lambda = 3.2$.

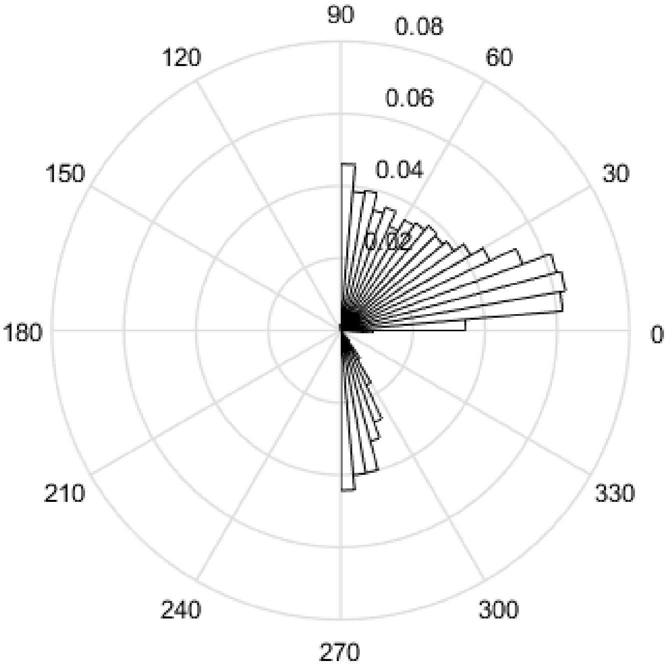

Figure 4.45: Histogram of Measured Tuft Orientations for Tuft #40 at $\lambda = 3.2$, γ = -15°

Viewing individual tuft data, whether through histograms or through time history plots, can provide a closer look at the flow behaviour at specific points on the blade. The plots here provide evidence of the potential of this method, and how it complements the use of the interpolated tuft orientation maps for determining how the airflow over the blade is behaving in a variety of different conditions.

4.2.5 Tuft Flow Visualization Experimental Summary

The tuft flow visualization experiments described in this thesis built on the measurements and trends observed in the five-hole probe experiments, as well as other work in the literature. The result was a series of successful measurements of the stall development and distribution over the surface of a rotating wind turbine blade as a function of the tip speed ratio, λ, the yaw-offset position, γ, and the azimuthal location, ψ. Stall fraction measurements and trends matched expectations made based on theory presented in Section 2.1.1, as well as results presented by Swytink-Binnema and Johnson [36] and α measurements presented in Section 4.1.2. These results demonstrate the close relationship between the angle of attack and the flow separation or attachment over the blade surface.

The algorithm presented by Swytink-Binnema and Johnson [36] was expanded to include functionality introduced by Vey *et al.* [39], including the logging of individual tuft orientations, the development of a tuft orientation map, and the ability to look at the behaviour of specific tufts. Tuft orientation maps showed that stall on the blade typically formed beginning at the trailing edge and inboard region, where α was shown to be largest. When the wind turbine was yawed, the tuft orientation maps were used to distinguish how the flow over the blade varied with azimuthal location, aiding in the identification of blade regions which may oscillate between attached and separated flow. Perhaps most significantly, plots of the uncertainty associated with the individual tuft orientations showed an increased accuracy in comparison to the stall fraction method, which could be biased towards greater stall values when fewer tufts were recognized in a frame.

Chapter 5

Conclusions and Recommendations

5.1 Summary of Project Objectives

As the number of installed wind turbines grows, developments in wind turbine measurements and modeling are required to accurately assess and improve the performance of wind turbine blades. To address this problem, this thesis was split into two focus areas: the measurement and modelling of the wind turbine blade angle of attack using a five-hole probe and an innovative in-blade data acquisition system; and the expansion of a digital image processing algorithm for analyzing tuft flow visualization experiments. Both of these goals were achieved successfully. Angle of attack and span-wise angle measurements were obtained as a function of the azimuthal position, tip speed ratio, yaw-offset angle and radial position, and these results were compared to models presented in the literature. Tuft flow visualization experiments were also conducted as a function of the same variables, and results were successfully processed using individualized tuft recognition to generate maps of instantaneous flow direction and separation over the blade. A brief summary and recommendations related to both projects experimental methods and results are presented in the following sections.

5.2 Summary of Results

5.2.1 Five-Hole Probe Results

The five-hole probe and in-blade data acquisition system were used to successfully measure the angle of attack, span-wise flow angle and upstream wind speed. In axial flow conditions, the angle of attack was observed to be relatively constant with azimuthal position. As the tip speed ratio was decreased (*i.e.* wind speed increased), the angle of attack increased by as much as 10° in the r/R 0.72 and 0.55 cases. Comparing the measurements taken at different radial locations, the angle of attack was observed to increase significantly as the probe was moved closer to the root of the blade. Both of these findings show that there is a measurable relationship between α, λ and r/R.

When the turbine was yawed ±15°, a significant azimuthal variation in the angle of attack was measured. From peak-to-peak, the angle of attack was shown to vary by as much as 7°. It was posited that the variation in α with azimuthal position is due to the cyclical change in wind velocity direction relative to the airfoil. That is, as the airfoil rotates into the wind, α decreases, and as the airfoil rotates away from the wind, α increases.

Angle of attack measurements were also compared to theoretical models to provide validation cases. Measurements in axial and yawed cases showed similar results to models both in azimuthal variation and in magnitude. Results showed that the models varied from each other by less than 1°, and tended to slightly overpredict and underpredict the measured angle of attack at different tip speed ratios. In general, the agreement between the measured and calculated values indicates that the models are accurate in predicting the observable variation in α as a function of γ, λ and r/R.

The five-hole probe measurements were also used to characterize the upstream flow speed and the axial induction factor of the turbine. While the calculated upstream flow speeds were in close agreement with wind speeds corresponding to the set fan frequencies, the axial induction factors calculated were more than 100% off of values predicted. It was posited that this disagreement was caused by limited lift and drag data available for the blade in the limited range of Reynolds numbers tested.

The span-wise flow angle measurements again showed trends consistent with the theory, as well as indicating a slight upward flow in the facility. In axial conditions, the span-wise angle was shown to be relatively constant with azimuthal position and tip speed ratio. However, it did vary with radial location, with measured values of approximately 16° at $r/R = 0.55$ and 13° at $r/R = 0.72$. This indicates that wind flow closer to the rotor is diverted further outboard to pass the obstruction of the turbine. When the turbine was yawed, the span-wise angle was shown to vary by as much as 10° throughout the blade rotation, indicating that the upstream flow repeatedly oscillates between traveling towards the root and tip of the blade.

Finally, the measurements of shaft torque throughout the five-hole probe experiments were presented. While the shaft torque was found to increase as α increased, rapid changes in the angle of attack were shown to have little influence on the torque measured. Torque values in both axial and yawed cases were shown to vary by less than 2° during blade rotation, which is less than the experimental uncertainty associated with the measurements. This was thought to be due to the significant inertia of the wind turbine rotor compared to the brief increases in force on the blade throughout the rotation, in combination with the limited sensitivity of the torque sensor on such a small scale.

5.2.2 Tuft Flow Visualization Results

The Swytink-Binnema and Johnson image processing algorithm was successfully expanded to include individualized tuft stall criteria, as well as the generation of contour maps of flow angles over the blade using measured tuft data. Experiments were conducted to generate new stall video to analyze, as well as to compare to angle of attack measurements. In axial conditions, the measured stall fraction was found to be relatively constant with azimuthal position, similar to the α measurements made with the five-hole probe. However, as the tip speed ratio was decreased, the stall fraction increased significantly, from approximately 25% at $\lambda = 7.0$ to 60% at $\lambda = 3.2$.

As the turbine was yawed, the stall fraction was observed to vary cyclically with azimuthal position similar to angle of attack measurements made in the previous experiments. ζ was shown to vary by as much as 25% at $\lambda = 3.2$ and γ = -15°. The oscillations matched trends observed in α measured with the five-hole probe. That is, as the blade rotated towards the wind and α decreases, ζ also decreased, and vice versa. The results indicate that variations in λ and γ can have significant effects on the stall formation over wind turbine blades. Variations associated with yaw can be especially concerning given the implications associated with cyclical loading and fatigue of the wind turbine blades.

Tuft orientation maps showed that stall over the wind turbine blade tended to form at the trailing edge of the blade first and expand outboard and towards the leading edge as the tip speed ratio decreased. The tuft orientation maps also showed that the flow was consistently oriented slightly outboard, with the angle increasing towards the blade root. This indicates that the flow angle is greater closer to the obstruction of the turbine nacelle and rotor.

Examining the variations in the contour maps with azimuthal position for measurements made in yaw conditions demonstrated the stall formation to a greater extent as the angle of attack fluctuated between maximum and minimum values throughout the rotation. As the blade rotated towards the wind and α was decreased, the interpolated map showed that most of the flow over the blade was oriented along the chordline. However, as the blade rotated away from the wind, the flow angle map becomes much more varied, reaching flow angles as high as 30° halfway along the chord. This is in agreement with the stall fraction results, and indicates that the amount of stall over the blade cycles significantly during yawed operation.

Flow behaviour over the wind turbine blade was also examined at specific points on the blade surface by focusing on individual tufts. Several histograms for tufts in different flow regimes were presented, which demonstrated the flow behaviour at attached and separated flow regions. In attached regions, the histograms showed tuft behaviour to be essentially constant, with orientations focused at approximately 0° (*e.g.* in line with the wind direction, or attached). In contrast, tufts in the stalled regions of the blade showed significant variation in orientation, oscillating between outboard and inboard orientations, or between stalled and attached flow.

5.3 Recommendations

Throughout the experiments, several issues with the experimental set-up were recognized which should be addressed in future studies for improving the quality of measured data. Here, recommendations related to the five-hole probe and tuft flow visualization experiments will be discussed.

5.3.1 Five-Hole Probe Recommendations

While the five-hole pressure probe measurements presented in Section 4 were successful, several issues were identified in the methods and results which should be addressed should further five-hole probe measurements be conducted. The following recommendations would improve the experimental results for the test configurations presented in this thesis.

- Remove the non-uniformity in the upstream flow field, whether through modification of the relative fan frequencies, the physical fan layout, or the screen density in the plenum of the facility. The non-uniformity could also be characterized using an array of 5-hole pressure probes to measure the flow velocity and direction. The non-uniformity in the flow was observed in all measured results, and limits the comparison which can be done to theoretical models.

- Conduct simultaneous wind velocity measurements upstream and directly downstream of the wind turbine rotor to better estimate the axial induction factor along the wind turbine blade span at different wind speeds.
- Replace the current torque sensor with a sensor of more appropriate capacity. The current sensor has a capacity of 200 Nm, yet was only used to measure a maximum torque of less than 30 Nm. It is expected that, if a more sensitive torque sensor with a narrower capacity were used, azimuthal variations in torque would be better reflected in the data.
- To conduct experiments where flow angle measurements are triggered at specific azimuthal locations, the in-blade DAQ system should be replaced with a more sophisticated, shielded circuit board. The current Uno [53] based design is appropriate for a prototype, but loose connections and little shielding resulted in significant noise interference when triggering measurements.
- To investigate the effect of the angle of attack on stall development more directly, five-hole probe measurements and stall measurements should be conducted simultaneously on the same blade. This could either be done by distributing tufts over the Abdelrahman [10] blades, or by designing a new twisted and tapered 3D printed blade which could also house the in-blade DAQ system.

5.3.2 Tuft Flow Visualization Recommendations

Tuft flow visualization experiments were successfully conducted, and the resulting video was analyzed using the modified digital image processing algorithm. Recommendations for improving the quality of the tuft flow visualization results are as follows.

- Use a higher quality camera designed specifically for research purposes. While it may be considered a risk to attach a more expensive camera to a rotating wind turbine blade, the decreased exposure time would increase the amount of tufts recognized in each frame, improving the data analysis.
- Use a camera with a higher resolution internal clock to allow for synchronization between the video data and azimuthal position data recorded by LabView [56]. This

could also be resolved by developing a LabView [56] VI which could communicate with the camera directly.

- Increase the density of tufts attached to the wind turbine blade. Care must be taken to avoid overlapping tufts in the video, but increasing the tuft density would improve the resolution of the interpolated flow maps.

Chapter 6

Bibliography

Bibliography

[1] CanWEA. *Canada's Current Installed Capacity.* [Online]. 2016. [Accessed: July 9, 2016]. Available: canwea.ca/wp-content/uploads/2016/02/Canada-Current-Installed-Capacity_e.pdf

[2] T. Burton, N. Jenkins, D. Sharpe, E. Bossanyi, *Wind Energy Handbook*, 2nd ed., West Sussex, United Kingdom: John Wiley & Sons Ltd., 2011.

[3] D. Wood, *Small Wind Turbines: Analysis, Design and Application.* Ch. 1, pp. 1-25. London, England: Springer-Verlag, 2011.

[4] Wind Power Monthly. *The 10 Biggest Turbines in the World*. [Online]. July 1, 2016. [Accessed: July 10, 2016]. Available: windpowermonthly.com/10-biggest-turbines

[5] S. Moreau, M. Roger, J. Christophe. *Flow Features and Self-Noise of Airfoils Near Stall or in Stall.* 30th AIAA Aeroacoustics Conference. Miami, Florida, AIAA, May 2009.

[6] W. Haans, T. Sant, G. van Kuik, G. van Bussel. *Stall in Yawed Flow Conditions: A Correlation of Blade Element Momentum Predictions with Experiments* 44th AIAA Aerospace Sciences Meeting and Exhibit, (Reno, Nevada), AIAA, 2006.

[7] T. Burton, N. Jenkins, D. Sharpe, E. Bossanyi, *Wind Energy Handbook* 2nd ed., Ch. 3, pp. 120-136. West Sussex, United Kingdom: John Wiley & Sons Ltd., 2011.

[8] T. Burton, N. Jenkins, D. Sharpe, E. Bossanyi, *Wind Energy Handbook* 2nd ed., Ch. 3, pp. 39-66. West Sussex, United Kingdom: John Wiley & Sons Ltd., 2011.

[9] UIUC Applied Aerodynamics Group: Department of Aerospace Engineering. *PROPID for Horizontal Axis Wind Turbine Design*. [Online]. 2016. [Accessed: March 22, 2016]. Available: http://m-selig.ae.illinois.edu/propid.html.

[10] A.H. Abdelrahman, *Development of a Wind Turbine Test Rig and Rotor for Trailing Edge Flap Investigation*. Master's thesis, University of Waterloo, Waterloo, Canada. 2014.

[11] D. Gertz, D.A. Johnson, N. Swytink-Binnema, *An Evaluation Testbed for Wind Turbine Blade Tip Designs - Windlet Results*. Wind Engineering. 2012. Vol. 36, No. 4, pp. 389-410.

[12] T. Burton, N. Jenkins, D. Sharpe, E. Bossanyi, *Wind Energy Handbook* 2nd ed., Ch. 4, pp. 137-155. West Sussex, United Kingdom: John Wiley & Sons Ltd., 2011.

[13] J. Morote, *Angle of Attack Distribution on Wind Turbines in Yawed Flow*. Wind Energ. 2015. DOI: 10.1002/we.1859.

[14] S. Tavoularis, *Measurement in Fluid Mechanics*. Cambridge, UK: Cambridge University Press, 2005.

[15] A. Choudhry, M. Arjomandi, R. Kelso, *Horizontal Axis Wind Turbine Dynamic Stall Predictions Based on Wind Speed and Direction Variability*. Proc IMechE Part A: J Power and Energy. 2013. 227(3) pp. 338-351. DOI: 10.1177/0957650912470941

[16] M.M. Hand, D.A. Simms, L.J. Fingersh, D.W. Jager, J.R. Cotrell, S. Schreck, S.M. Larwood, *Unsteady Aerodynamics Experiment Phase VI: Wind Tunnel Test Configurations and Available Data Campaigns*. National Renewable Energy Laboratory. December 2001. Technical Report TP-500-29955.

[17] C.P. Butterfield, W.P. Musial, D.A. Simms, *Combined Experiment Phase I: Final Report*. National Renewable Energy Laboratory. October 1992. Technical Report TP-257-4655.

[18] J.G. Schepers, R.P.J.O.M. van Rooij, *Analysis of aerodynamic measurements on a model wind turbine placed in the NASA-Ames tunnel*. Energy Research Centre of the Netherlands. 2008. Technical Report ECN-E–08-052.

[19] C.P. Butterfield, *Three-Dimensional Airfoil Performance Measurements on a Rotating Wing*. Solar Energy Research Institute. 1989. Technical Report SERI/TP-217-3505.

[20] W.Z. Shen, M.O.L. Hansen, J.N. Sørensen, *Determination of the Angle of Attack on Rotor Blades*. Wind Energ. 2009. Vol 12, pp. 91-98. DOI: 10.1002/we.277.

[21] T. Maeda, H. Kawabuchi, *Surface Pressure Measurement on a Rotating Blade Field Horizontal Axis Wind Turbine in Yawed Condition.* JSME Int. J. 2005. Series B, Vol. 48, No. 1.

[22] A. Moscardi, D.A. Johnson, *A Compact In-blade Five Hole Pressure Probe for Local Inflow Study on a Horizontal Axis Wind Turbine.* Wind Energ. November 2015.

[23] A. Moscardi, Five Hole Pressure Probe for Local Inflow Study on a Horizontal Axis Wind Turbine. Master's Thesis, University of Waterloo, Canada and Politecnio di Milano, Italy. 2014.

[24] G.L. Morrison, M.T. Schobeiri, K.R. Pappu, *Five Hole Pressure Probe Analysis Technique.* Flow Measurement and Instrumentation. 1998. 9:153-158.

[25] T.J. Dudzinsky, L.N. Krause. *Flow Direction Measurement with Fixed-Position Probes.* NASA Lewis Research Center. 1969. Technical Report NASA-TM-X-1904.

[26] L.J. Fingersh, M.C. Robinson. *Wind Tunnel Calibration of 5-Hole Pressure Probes for Application to Wind Turbines.* National Renewable Energy Laboratory. 1997. Technical Report NRE/CP-500-22134.

[27] R.W. Gallington, *Measurement of Very Large Flow Angles with Non-Nulling Seven-Hole Probes.* USAFA. 1980. Technical Report USAFA-TR-80-17.

[28] A.R. Paul, R.R. Upadhyay, A. Jain, *A Novel Calibration Algorithm for Five-Hole Pressure Probe.* International Journal of Engineering, Science and Technology. 2011. 3(2):89-95.

[29] G.G. Zilliac. *Modelling, Calibration, and Error Analysis of Seven-Hole Pressure Probes.* Experiments in Fluids. 1993. Vol. 14, pp. 104-120.

[30] M.M. Petersen, T.J. Larsen, H.A. Madsen, G.C. Larsen, N. Toldborg. *Turbulent Wind Field Characterization and Re-generation Based on Pitot Tube Measurements Mounted on a Wind Turbine.* 33rd Wind Energy Symposium. 2015. Kissimmee, United States.

[31] H.A. Madsen, C. Bak, M. Døssing, R. Mikkelsen, S. Øye, *Validation and Modification of the Blade Element Momentum Theory Based on Comparisons with Actuator Disc Simulations.* Wind Energy. 2010. Vol. 13, No. 4, pp. 373-389.

[32] H.A. Madsen, C. Bak, U.P. Schmidt, M. Gaunaa, P. Fuglsang, J. Romblad, N.A. Olesen, P. enevoldsen, J. Laursen, L. Jensen, *The DAN-AERO MW Experiments: Final Report.* Danmarks Tekniske Universitet, Risø Nationallaboratoriet for Bæredygtig Energi, 2010.

[33] S. Tavoularis, *Measurement in Fluid Mechanics.* New York, NY: Cambridge University Press, 2005, p. 222.

[34] W. Merzkirch, *Techniques of Flow Visualization.* AGARDograph. 1987. AGARD-302: 6-7.

[35] D. Eggleston, K. Starcher. *A Comparative Study of the Aerodynamics of Several Wind Turbines Using Tuft Flow Visualization.* Journal of Solar Energy Engineering. 1990. Vol. 112, pp. 301-309.

[36] N. Swytink-Binnema, D.A. Johnson. *Digital Tuft Analysis of Stall on Operational Wind Turbines.* Wind Energy. 2016. Vol. 19, No. 4, pp. 703-715, DOI: 10.1002/we.1860.

[37] GoPro. *How to Update Your HD Hero2.* [Online]. 2016. [Accessed: March 28, 2016] Available: https://gopro.com/update/hdhero2.

[38] N. Swytink-Binnema. *Digital Tuft Flow Visualization of Wind Turbine Blade Stall.* Master's thesis, University of Waterloo, Waterloo, Canada. 2014.

[39] S. Vey, H.M. Lang, C.N. Nayeri, C.O. Paschereit, G. Pechlivanoglou. *Extracting Quantitative Data from Tuft Flow Visualizations on Utility Scale Wind Turbines.* Journal of Physics: Conference Series. 2014. Vol. 524, DOI: 10.1088/1742-6596/524/1/012011.

[40] S. Tavoularis, *Measurement in Fluid Mechanics.* Cambridge, UK: Cambridge University Press, 2005. pp. 45-50.

[41] D.A. Johnson, A. Abdelrahman, D. Gertz, *Experimental Indirect Determination of Wind Turbine Performance and Blade Element Theory Parameters in Controlled Conditions.* Wind Engineering. 2012. Vol. 36, No. 6, pp. 717-738.

[42] C.B. Devaud, J. Weisinger, D.A. Johnson, E.J. Weckman, *Experimental and Numerical Characterization of the Flowfield in the Large-Scale UW Live Fire Research Facility.* Int. J. Numer. Meth. Fluids. 2009. Vol. 60, pp. 539-564.

[43] B. Gaunt, *Power Generation and Blade Flow Measurements of a Full-Scale Wind Turbine.* Master's thesis, University of Waterloo, Waterloo, Canada. 2009.

[44] C. Best, *Measurement of Fuel Regression Rate of a Pool Fire in Crosswind With and Without a Large Downwind Blocking Object*. Master's thesis, University of Waterloo, Waterloo, Canada. 2010.

[45] Marathon Electric, *Motor Model Details* [Online]. 2016. [Accessed March 22, 2016]. Available: http://www.marathonelectric.com/MMPS/details.jps?item=184THTL17038.

[46] Emerson Electric Co., *Unidrive SP Panel Mount - High Performance Universal AC Drive Range.* [Online]. 2016. [Accessed March 22, 2016]. Available: http://www.emersonindustrial.com/en-US/controltechniques/products/acdrives/unidrivesppanelmount/Pages/default.aspx.

[47] Nord Drivesystems. *NordBlock.1 Series Gearmotors and Speed Reducers.* [Online]. 2014. [Accessed March 22, 2016]. Available: https://www.nord.com/cms/media/documents/bw/g1013_us.pdf.

[48] Futek Advanced Sensor Technology Inc. *Rotary Torque Sensor - Non Contact Shaft to Shaft with Encoder.* [Online]. 2016. [Accessed March 22, 2016]. Available: http://www.futek.com/product.aspx?t=torque&m=trs605.

[49] D.M. Somers, *The S833, S834, and S835 Airfoils.* National Renewable Energy Laboratory. August 2005. Subcontract Report SR-500-36340.

[50] T. Gallant, D.A. Johnson, *In-blade angle of attack measurement and comparison with models.* Journal of Physics Conference Series. 2016. *In Press.*

[51] Honeywell. *truStability Board Mount Pressure Sensors: HSC Series - High Accuracy.* [Online]. 2011. [Accessed July, 2014]. Available: http://www.mouser.com/ds/2/187/HSC%20Analog-221530.pdf.

[52] Rascal Micro. *Precision Voltage Shield.* [Online]. 2016. [Accessed: March 23, 2016]. Available: https://store.rascalmicro.com/products/precision-voltage-shield.

[53] Arduino. *Arduino UNO and Genuino UNO.* [Online]. 2016. [Accessed: March 23, 2016]. Available: https://www.arduino.cc/en/Main/ArduinoBoardUno.

[54] Campbell Scientific. *CSAT3 3-D Sonic Anemometer.* [Online]. 2016. [Accessed: March 29, 2016]. Available: https://www.campbellsci.ca/csat3.

[55] FairChild Semiconductor. *H21A1 / H21A2 / H21A3 Phototransistor Optical Interrupter Switch.* [Online]. 2001. [Accessed: March 29, 2016]. Available: http://www.robotstorehk.com/h21a1.pdf.

[56] National Instruments. *LabVIEW System Design Software*. [Online]. 2016. [Accessed: July 26, 2016]. Available: www.ni.com/labview/.

[57] D.M. Somers. *The S833, S834, and S835 Airfoils*. National Renewable Energy Laboratory. August 2005. Technical Report NREL/SR-500-36340.

[58] GoPro. *How to Update Your Hero3*. [Online]. 2016. [Accessed: March 30, 2016] Available: https://gopro.com/update/hero3.

[59] J. Weisinger, *Characterization of the University of Waterloo Live Fire Research Facility Wind Generation System*. Master's thesis, University of Waterloo, Waterloo, Canada. 2004.

[60] Airfoil Tools. *NREL's S833 Airfoil (s833-nr)*. [Online]. 2016. [Accessed: June 15, 2016] Available: http://airfoiltools.com/airfoil/details?airfoil=s833-nr.

[61] Mathworks, Inc. *MATLAB*. [Online]. 2016. [Accessed: June 29, 2016]. Available: www.mathworks.com/products/matlab/.

Appendices

Appendix A

Arduino Uno Sketch

```
#include <SPI.h>

#define RESOLUTION 16

#define SCALE_FACTOR 0.000152587890625

//pins for shield
#define BUSY 3
#define RESET 4
#define START_CONVERSION 5
#define SHcs 10

#define TOTAL_RAW_BYTES RESOLUTION

int bytesToRead = TOTAL_RAW_BYTES;
byte raw[TOTAL_RAW_BYTES];
signed long parsed[8];
int i;
int v = 0;
int c;

void setup() {

  pinMode(BUSY, INPUT);
```

```
  pinMode(RESET, OUTPUT);
  pinMode(START_CONVERSION, OUTPUT);
  pinMode(SHcs,OUTPUT);

  SPI.begin();
  Serial.begin(115200);

  digitalWrite(START_CONVERSION, HIGH);
  digitalWrite(SHcs, HIGH);
  digitalWrite(RESET, HIGH);
  delay(1);
  digitalWrite(RESET, LOW);
}

void loop() {
    Serial.print(v);
    Serial.print(",");
    v = v + 1;
    Serial.print(millis());
    Serial.print(",");
    reading();
    delay(40);
}

void parseRawBytes() {
  int i;
      parsed[0] = (raw[0] << 8) + (raw[1] >> 0);
      parsed[1] = (raw[2] << 8) + (raw[3] >> 0);
      parsed[2] = (raw[4] << 8) + (raw[5] >> 0);
      parsed[3] = (raw[6] << 8) + (raw[7] >> 0);
      parsed[4] = (raw[8] << 8) + (raw[9] >> 0);
      parsed[5] = (raw[10] << 8) + (raw[11] >> 0);
      parsed[6] = (raw[12] << 8) + (raw[13] >> 0);
      parsed[7] = (raw[14] << 8) + (raw[15] >> 0);
  for(i=0; i<8; i++) {
    parsed[i] = fixSignBit(parsed[i]);
  }
}
```

```
long fixSignBit(long reading) {
      if(reading & 0x8000) { // if reading is < 0
      //(stored as two's complement)
        return reading | 0xFFFF0000; // set bits 31-16
      } else {
        return reading;
      }
}

void reading(){
  digitalWrite(START_CONVERSION, LOW);
  delayMicroseconds(10);
  digitalWrite(START_CONVERSION, HIGH);
  while (digitalRead(BUSY) == HIGH) {
  }
  digitalWrite(SHcs, LOW);
  while (bytesToRead > 0) {
    raw[TOTAL_RAW_BYTES - bytesToRead] = SPI.transfer(0x00);
    bytesToRead--;
  }
  digitalWrite(SHcs, HIGH);
  bytesToRead = TOTAL_RAW_BYTES;
  parseRawBytes();

  Serial.print((float)parsed[1] * SCALE_FACTOR * 1000, 5);
  Serial.print(",");
  Serial.print((float)parsed[2] * SCALE_FACTOR * 1000, 5);
  Serial.print(",");
  Serial.print((float)parsed[3] * SCALE_FACTOR * 1000, 5);
  Serial.print(",");
  Serial.print((float)parsed[4] * SCALE_FACTOR * 1000, 5);
  Serial.print(",");
  Serial.print((float)parsed[5] * SCALE_FACTOR * 1000, 5);
  Serial.print(",");
  Serial.println((float)parsed[6] * SCALE_FACTOR * 1000, 5);
}
```

Appendix B

Review of Experimental Uncertainty

A key part of interpreting experimental results is estimating the uncertainty associated with the measurements. In this section, a brief overview of experimental uncertainty will be presented to provide context to the uncertainty analysis presented in Section 3.5.

The basis for any uncertainty analysis is that the true error in the measurement cannot be known. By definition, experimental uncertainty is an estimate of how much error there is in a measurement [40]. Generally, uncertainty is divided into two categories: bias uncertainty and precision uncertainty. Bias uncertainty is caused by fixed or systematic errors in the instrumentation or method [40]. For example, a temperature probe which always reads 5% too high would be considered to have a bias uncertainty of 5% of the reading. In contrast, the precision uncertainty is made up of random errors in the measurement, either due to noise in the equipment or the signal being measured [40]. When these two uncertainties are evaluated to the same level of confidence, they can be combined using the root-sum-square method to find the total uncertainty, as shown in equation (B.1).

$$u_{tot} = \sqrt{b^2 + p^2} \tag{B.1}$$

Similarly, independent bias or precision errors can be combined using the root-sum-square method. Bias uncertainties are typically evaluated separately and then combined, while the estimate of precision uncertainty is largely based on a statistical analysis of the variation in the measured data. For a sample size greater than 30, the precision uncertainty can be calculated using equation (B.2):

$$p = \frac{2\sigma}{N_{samp}} \tag{B.2}$$

where σ is the standard deviation of the measurements and N_{samp} is the number of samples.

Finally, when a derived property is dependent on calculations involving more than one variable with uncertainty, the uncertainty of the independent variables must be propagated through the equation to determine the uncertainty associated with the dependent variable. If this relationship is in the form $y = f(x_1, x_2, ..., x_n)$, then the propagated uncertainty is calculated using equation (B.3).

$$u_y = \sqrt{\left(\frac{\delta y}{\delta x_1} u_1\right)^2 + \left(\frac{\delta y}{\delta x_2} u_2\right)^2 + ... + \left(\frac{\delta y}{\delta x_n} u_n\right)^2} \tag{B.3}$$

Appendix C

Uncertainty Calculations

C.1 Torque Uncertainty

To calculate the bias uncertainty associated with the torque sensor, $u_{b,torque}$, as presented in 3.5.2, the characteristics of the Futek [48] rotary torque sensor are required. The relevant values are summarized in Table C.1 as percentages of the total 200 Nm capacity. Summing these values using the Root-Sum-Square method [14] gives the total bias uncertainty for the torque measurements, as shown in (C.1). The calculation shows that the only significant contributer to the bias error is the uncertainty associated with the zero balance.

Table C.1: Summary of Futek [48] torque sensor characteristics.

Characteristic	% of Total Capacity	Actual Value
Zero Balance	1%	2 Nm
Nonlinearity	0.02%	0.04 Nm
Nonrepeatability	0.02%	0.04 Nm
Hysteresis	0.01%	0.02 Nm

$$u_{b,torque} = \sqrt{2^2 + 0.04^2 + 0.04^2 + 0.01^2} = 2.00Nm \tag{C.1}$$

C.2 Five Hole Probe Uncertainty

The Honeywell Board Mount Pressure Transducers [51] used on the pressure transducer board had a specificied accuracy of ± 0.25% FSS BFSL or 1%, a resolution of 0.03% FSS, and an orientation sensitivity of ±0.15% FSS. Given the full-scale value of 1245.87 Pa, these values were combined using the root-sum-square method [14] to reveal a bias uncertainty of ±3.65 Pa associated with the pressure transducer measurements. The bias uncertainty was then combined with the precision uncertainty for each pressure transducer, calculated using Equation (B.2), to determine the total uncertainty in the raw pressure measurements.

The estimated pressure uncertainties were then used to determine the uncertainty in the corresponding pressure coefficients, described in Table 2.1 [28]. This was done by propagating the uncertainty in each of the five transducers through the equations, using equation (B.3). As an example, the coefficient uncertainty equations derived when probe 5 reads the maximum pressure are provided in equations (C.2) through (C.5):

$$u_{\bar{p}} = \sqrt{4(\frac{1}{4}\bar{u}_p)^2} \tag{C.2}$$

$$u_D = \sqrt{(u_{\bar{p}})^2 + (\bar{u}_p)^2} \tag{C.3}$$

$$u_{Cp\alpha} = \sqrt{2(\frac{1}{D}\bar{u}_p)^2 + (\frac{P_3 - P_1}{D^2}4u_D)^2} \tag{C.4}$$

$$u_{Cp\beta} = \sqrt{2(\frac{1}{D}\bar{u}_p)^2 + (\frac{P_2 - P_4}{D^2}4u_D)^2} \tag{C.5}$$

where $u_{\bar{p}}$ is the uncertainty in the mean pressure given in Table 2.1, u_D is the uncertainty in D, and $\bar{u}_P$ is the mean of the pressure uncertainties for all points. This was a simplification made based on the assumption that the pressure uncertainties are relatively similar in magnitude given the pressures measured.

The uncertainty in the pressure coefficients was related to the uncertainty in the pitch and span-wise angles relative to the probe by direct comparison with the calibration data. Given that the majority of the coefficients used in this study were calculated using pressure zone 5, the average change in $C_{p,\alpha}$ and $C_{p,\beta}$ corresponding to a 5° change in the pitch relative to the probe was calculated for all orientations conducted within zone 5. The variation in calibration data for the other four pressure zones was similar enough to zone 5 that this was considered an appropriate simplification for the uncertainty analysis. This resulted in an estimated $\Delta C_{p,\alpha} = 0.128/\ ^{\circ}$pitch and $\Delta C_{p,\beta} = 0.0387/\ ^{\circ}$pitch.

Having estimated the variation in pressure coefficients per degree pitch, the uncertainties calculated for the pitch and span coefficients were converted to uncertainties in the pitch and spanwise angles relative to the blade ($u_{\alpha p}$ and $u_{\beta p}$, respectively) via a direct conversion. Uncertainties in the pitch and span wise angles relative to the blade were then calculated by propagating values relative to the probe through equation (2.34) for α reported by NREL [16]. The equation expressing the uncertainty propagation is provided in Equation (C.6).

$$u_{\alpha} = \sqrt{(\frac{\delta\alpha}{\delta\alpha_p})^2 u_{\alpha p}^2 + (\frac{\delta\alpha}{\delta\beta_p})^2 u_{\beta p}^2 + (\frac{\delta\alpha}{\delta\epsilon})^2 u_{\epsilon}^2 + (\frac{\delta\alpha}{\delta\gamma})^2 u_{\gamma}^2} \tag{C.6}$$

Given the length of the partial derivative equations required for equation (C.6), they have been omitted here. However, an example calculation was conducted for $r/R = 0.55$, $\lambda = 5.0$, $\gamma = 0^{\circ}$ which found that the equation works out to:

$$u_{\alpha} = \sqrt{8.64\mathrm{E}-7 + 7.18\mathrm{E}-9 + 5.28\mathrm{E}-8 + 3.37\mathrm{E}-6} = 0.0021\mathrm{rad} = 0.11^{\circ} \tag{C.7}$$

Reviewing the individual components which combine to give the complete u_{α} in relation to equation (C.6), it is found that the most significant uncertainty is related to u_{γ}, which is the uncertainty related to the orientation of the probe relative to the blade. This uncertainty in the probe offset was calculated to be $u_{\gamma} = 0.1052^{\circ}$ after 20 measurements of the probe offset were made using a digital protractor. Given the similarity between u_{α} and u_{γ}, it is evident that error associated with the probe offset is the primary source of uncertainty in the measurements. However, an uncertainty in the angle of attack measurement of $\pm 0.1^{\circ}$ is considered sufficient.

A similar analysis was conducted again for the uncertainty associated with the spanwise flow measurement. The uncertainty in the probe span-wise offset ($u_{\epsilon} = 0.2^{\circ}$) was found to be the most significant source of error, resulting in u_{β} values of approximately 0.6° for the same test case. Because the span-wise angle is not the focus of this study, this uncertainty was also deemed sufficient for these measurements.

The uncertainty method derived here was implemented in all analysis of the five-hole probe measurements. Error bars presented on plots of the results therefore represent the results of this analysis.

Appendix D

Pressure Transducer Calibration Equations

The following equations represent the best linear fit for the pressure transducer calibration curves presented in Section 3.3.4

$$V1 = 1.7246(P_1) + 2526.9 \tag{D.1}$$

$$V2 = 1.8066(P_2) + 2493.8 \tag{D.2}$$

$$V3 = 1.8032(P_3) + 2493.1 \tag{D.3}$$

$$V4 = 1.7504(P_4) + 2477.7 \tag{D.4}$$

$$V5 = 1.728(P_5) + 2475.4 \tag{D.5}$$

Appendix E

Angle of Attack Yaw Results

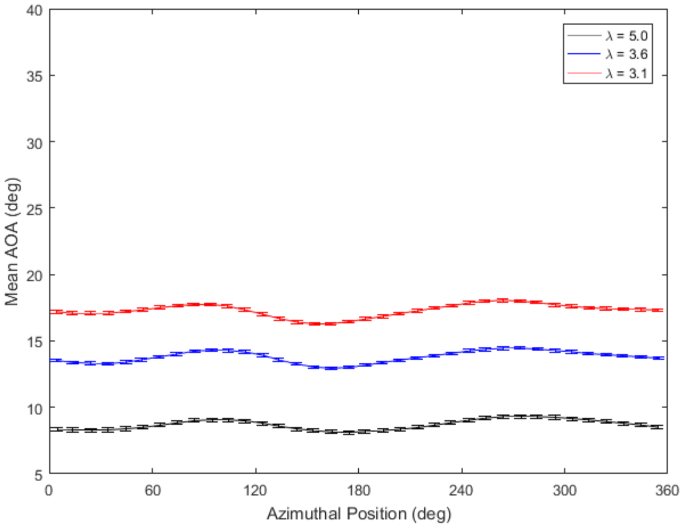

Figure E.1: Measured α distribution at $r/R = 0.72$, $\gamma = 5^{\circ}$

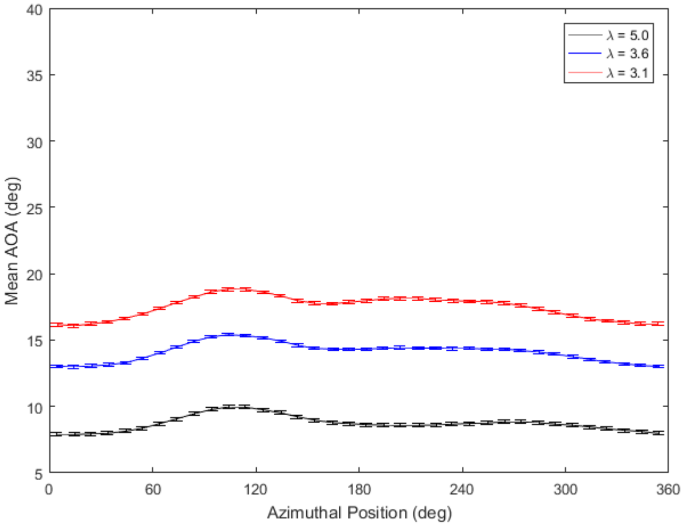

Figure E.2: Measured α distribution at $r/R = 0.72$, γ = -5°

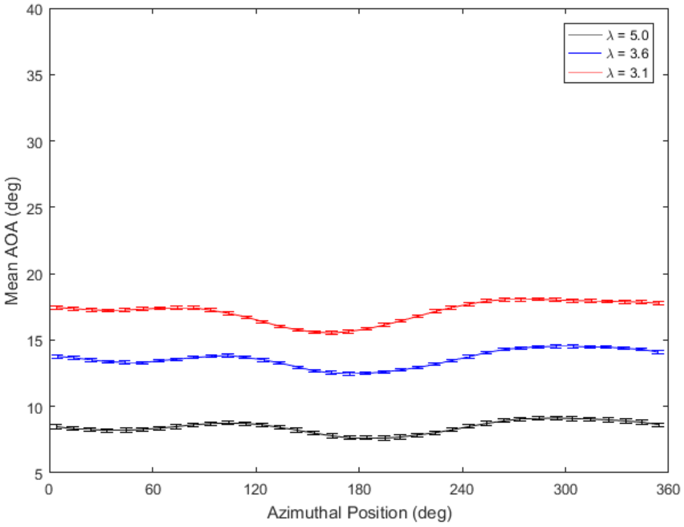

Figure E.3: Measured α distribution at $r/R = 0.72$, γ = 10°

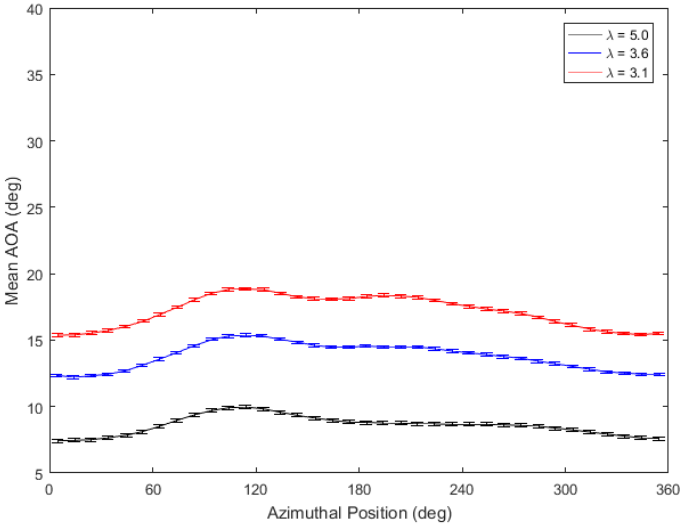

Figure E.4: Measured α distribution at $r/R = 0.72$, γ = -10°

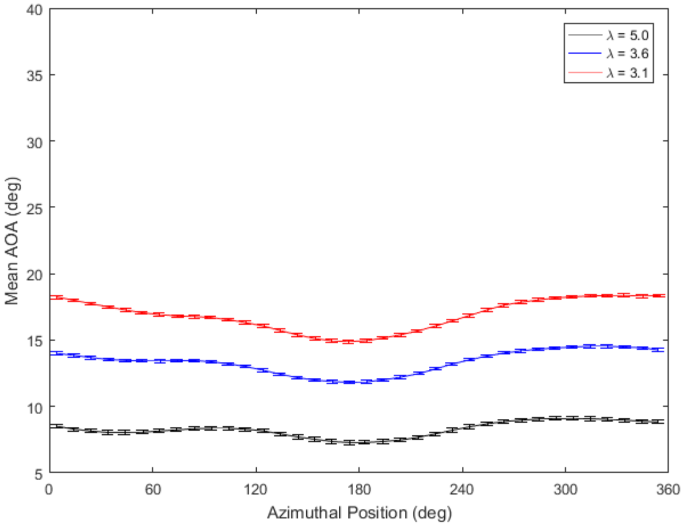

Figure E.5: Measured α distribution at $r/R = 0.72$, γ = 15°

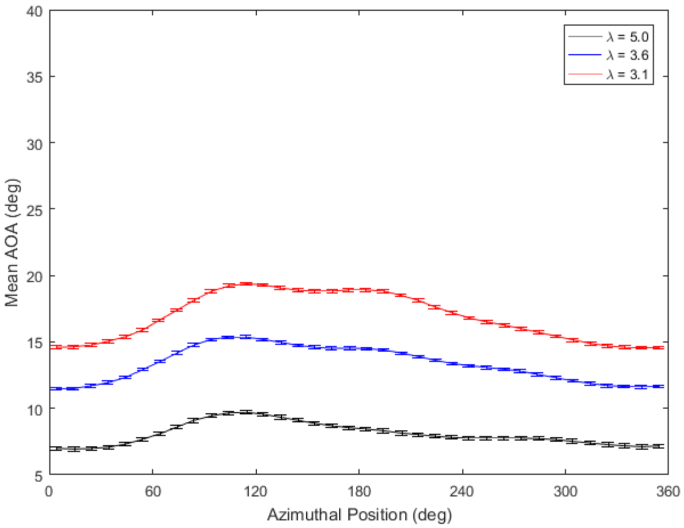

Figure E.6: Measured α distribution at $r/R = 0.72$, $\gamma =$ -15°

Appendix F

Span-wise Flow Angle Results

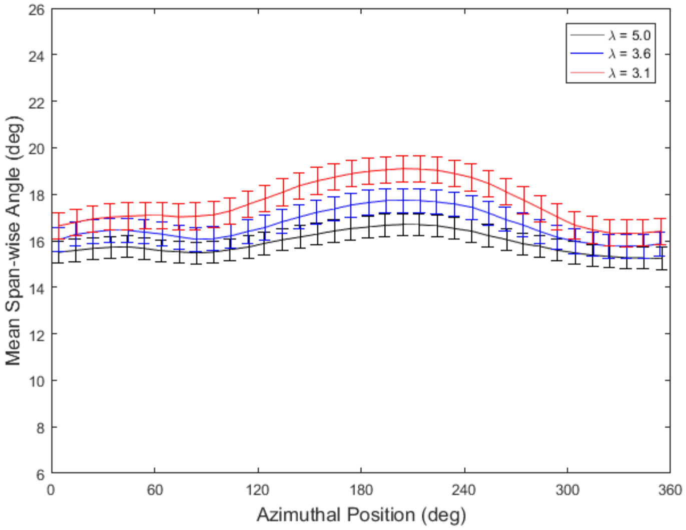

Figure F.1: Span-wise flow angle measured at $r/R = 0.55$, $\gamma = 0°$

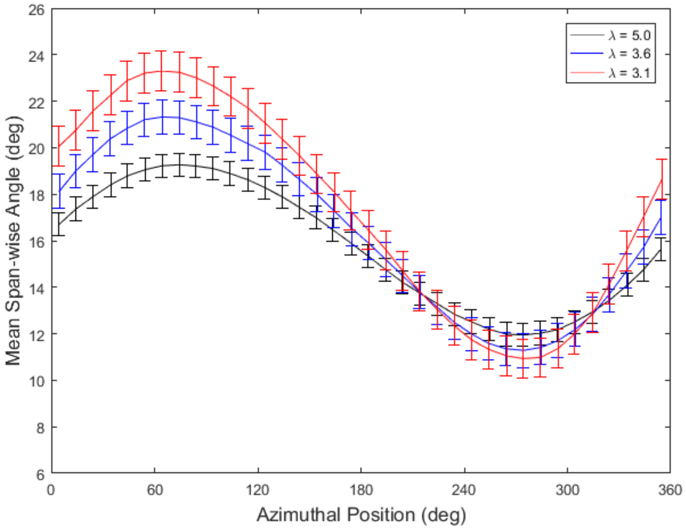

Figure F.2: Span-wise flow angle measured at $r/R = 0.55$, $\gamma = 15°$

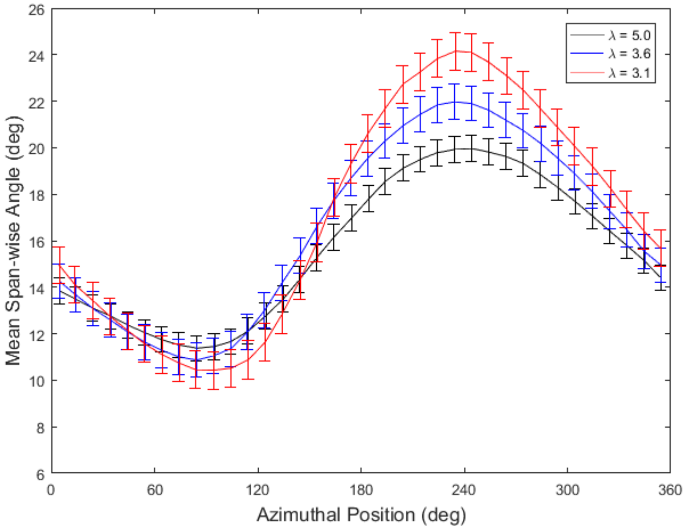

Figure F.3: Span-wise flow angle measured at $r/R = 0.55$, γ = -15°

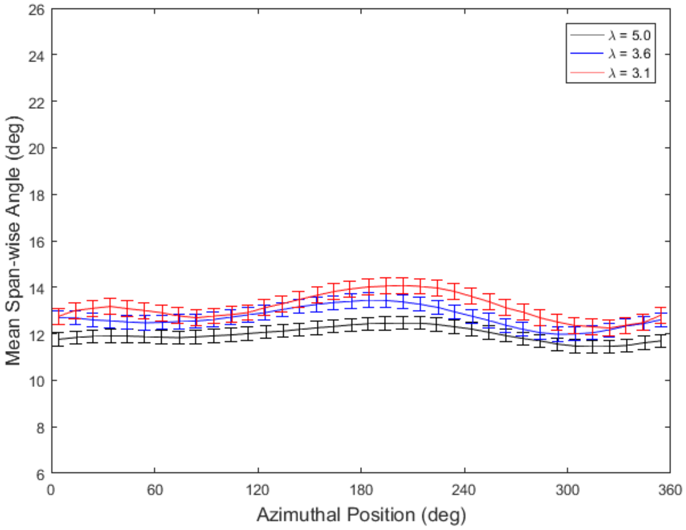

Figure F.4: Span-wise flow angle measured at $r/R = 0.72$, $\gamma = 0^\circ$

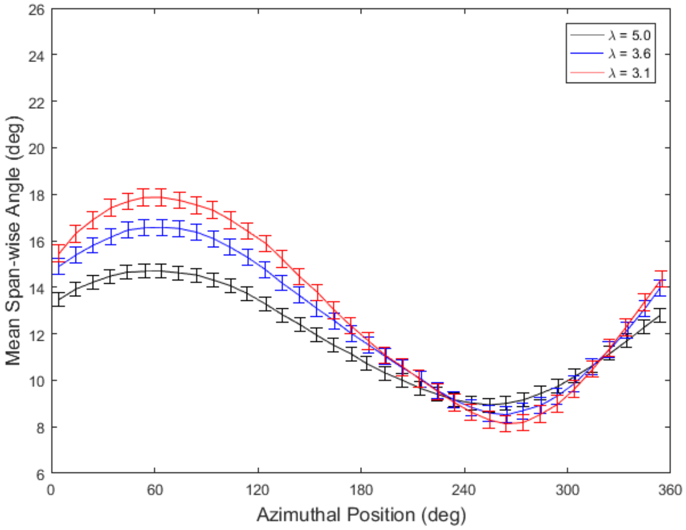

Figure F.5: Span-wise flow angle measured at $r/R = 0.72$, $\gamma = 15^\circ$

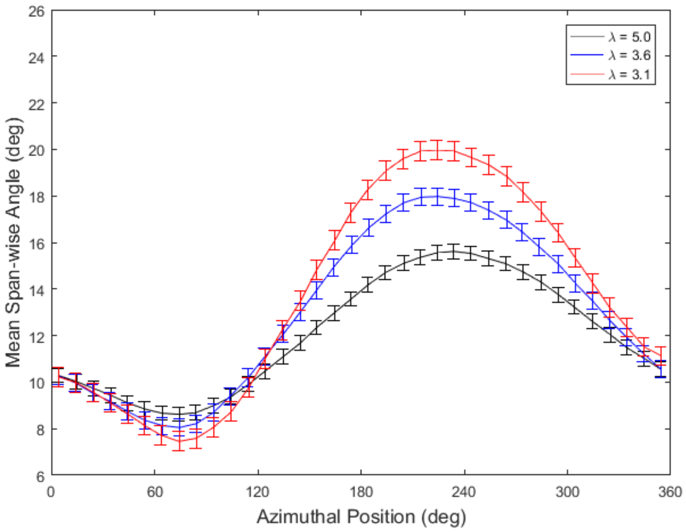

Figure F.6: Span-wise flow angle measured at $r/R = 0.72$, γ = -15°

Appendix G

Angular Momentum Calculations

The azimuthal variation in torque presented in Figures 4.28, 4.29 and 4.30 was found to be consistently negligible relative to the uncertainty in the measurements. It was posited that the lack of variation in torque despite varying α values was related either to the small scale change in torque, or due to the torque being dampened or smoothed out by the angular momentum of the rotor. In this Appendix, a demonstrative calculation of the variation in torque generated is provided and compared to the angular momentum of the turbine rotor.

First, the angular momentum of the wind turbine rotor must be determined. The angular momentum is defined as:

$$L = I\omega = mr^2\omega \tag{G.1}$$

where L is the angular momentum, I is the moment of inertia, m is the point mass of the rotor and r is the local radius of the point mass. From Abdelrahman [10], the mass of each wind turbine blade is 4.967 kg. If it is assumed that the center of mass is halfway along the blade span, and it is known that the rotor rotates at 200 rpm, the angular momentum can be calculated as follows:

$$L = (4.967\text{ kg} * 3\text{ blades})(0.5 * 1.7\text{ m})^2(20.94\text{ rad/s}) = 225.5\text{ kgm}^2/\text{s} \tag{G.2}$$

From Newton's second law, the total torque acting on the wind turbine rotor could be defined as a change in angular momentum over time. This relationship is expressed in (G.3). Therefore, to determine the relative impact of a change in torque on the angular momentum of the wind turbine rotor, the theoretical change in torque for a given change in α could be multiplied by a length of time to determine the corresponding change in momentum. Note that this is purely a demonstrative calculation to show the scale of the values concerned, and does not represent true or measured values.

$$\int T dt = I\omega \tag{G.3}$$

To estimate the theoretical change in momentum that could be expected from an increased angle of attack over a portion of the rotation, several assumptions were made. First, if was assumed that the increased angle of attack increases the torque on the blade over half of the rotation, which at a rotational rate of 200 rpm meant that the increased force occurred over a period of 0.15 seconds. Next, the torque was calculated by estimating the tangential force acting on the blade at the three radii represented by the five-hole pressure probe measurements. This was done using geometry defined in Figure 2.6 via Equation (G.4):

$$F_{tan} = F_L \sin\phi - F_D \cos\phi \tag{G.4}$$

where

$$\delta F_L = \frac{1}{2}\rho W^2 c C_L \delta r \tag{G.5}$$

$$\delta F_D = \frac{1}{2}\rho W^2 c C_D \delta r \tag{G.6}$$

A summary of the calculations is provided in Table G.1. For the calculation, three sections of the blade were used: $r/R = 0.25$ to 0.45, 0.45 to 0.65, and 0.65 to 0.85. This was done to maintain a constant δr of 0.2 for the calculations. This was considered sufficient for a demonstrative calculation to determine the relative scale of the torque increase, but cannot be considered completely accurate given the omission of the root and tip sections. Lift and drag coefficients were determined using lift and drag curves for the S833 airfoil [57] for angles of attack reported in section 4.1.2. Note that, for this test blade, $\phi = \alpha + 6°$.

Summing the torque values presented in Table G.1 results in an estimated 20.6 Nm of torque generated at lower angles of attack and 15.4 Nm generated at the higher range of α values. The difference of approximately 5 Nm multiplied by the Δt of 0.15 seconds results in a total change in angular momentum of 0.75 kg m^2/s, which is significantly less than

Table G.1: Calculation of Theoretical Torque Generated

r/R	α	C_L	C_D	W	F_L	F_D	F_{tan}	Torque
Low α								
0.38	30°	0.0	0.3	16.9 m/s	0.00 N	3.12 N	-1.83 N	-1.18 Nm
0.55	23°	0.9	0.2	22.1 m/s	15.96 N	3.55 N	6.02 N	5.63 Nm
0.72	17°	1.3	0.1	27.6 m/s	35.91 N	2.21 N	13.17 N	16.12 Nm
High α								
0.38	34°	-0.2	0.3	16.9 m/s	-2.08 N	3.64 N	-3.67 N	-2.37 Nm
0.55	27°	0.8	0.2	22.1 m/s	14.19 N	4.08 N	5.50 N	5.15 Nm
0.72	21°	1.0	0.2	27.6 m/s	27.62 N	4.97 N	10.28 N	12.59 Nm

the total angular momentum of 225 kg m^2/s. It is posited that, because of this insignficant change, the torque sensor mounted to the wind turbine shaft does not see a significant change in torque despite an increased force on the blade.

Appendix H

Interpolated Flow Angle Maps

The following figures present interpolated flow angle maps for the $\lambda = 3.2$, $\gamma =$ -15° case.

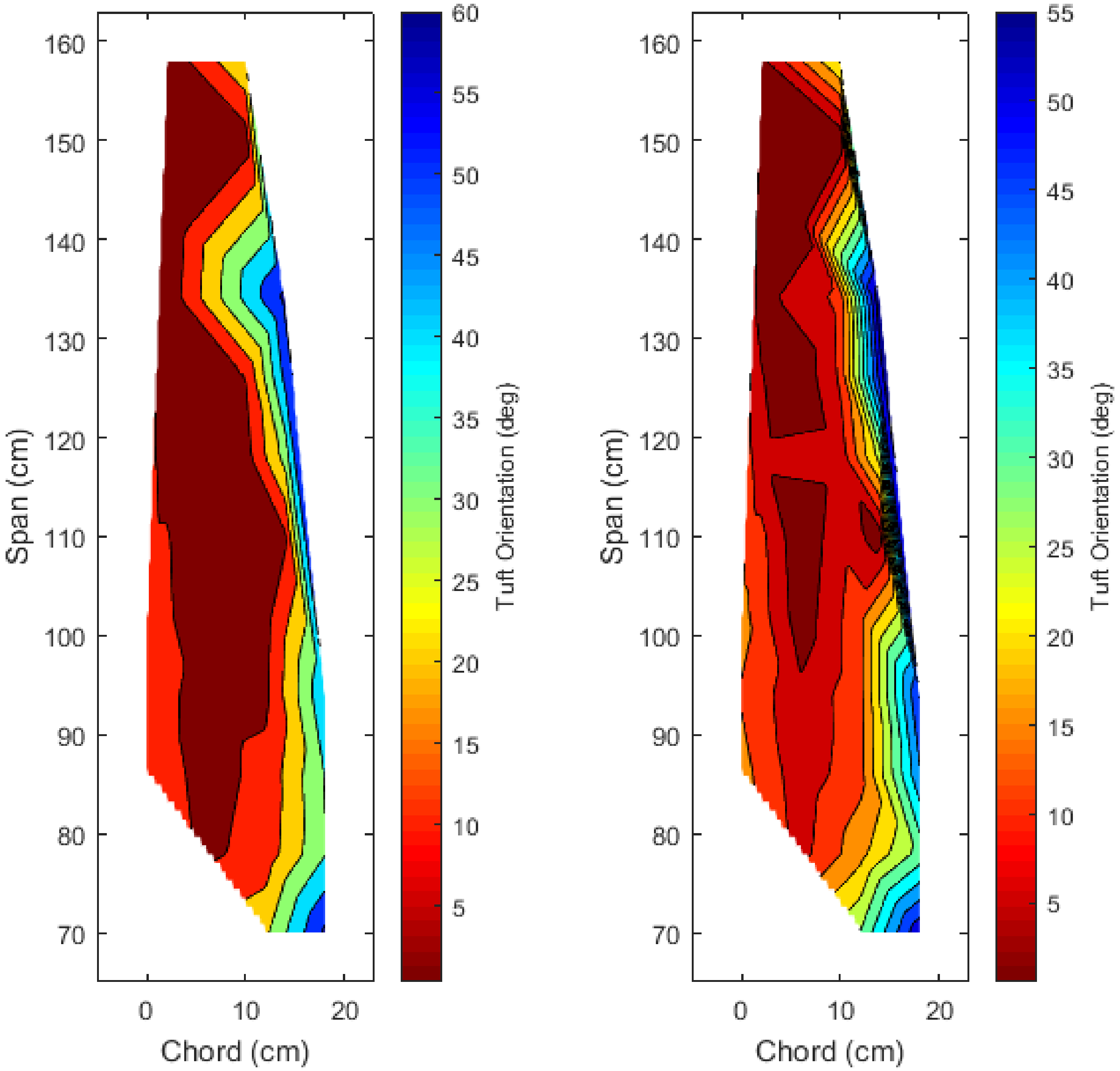

(a) $\psi = 0^{\circ}$

(b) $\psi = 30^{\circ}$

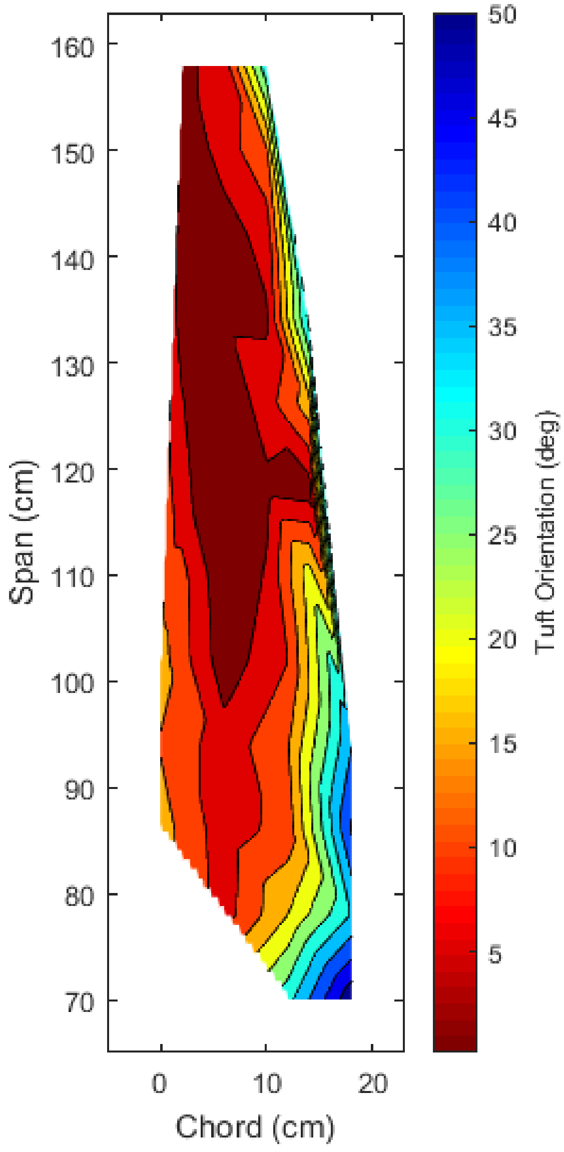

(c) $\psi = 60°$

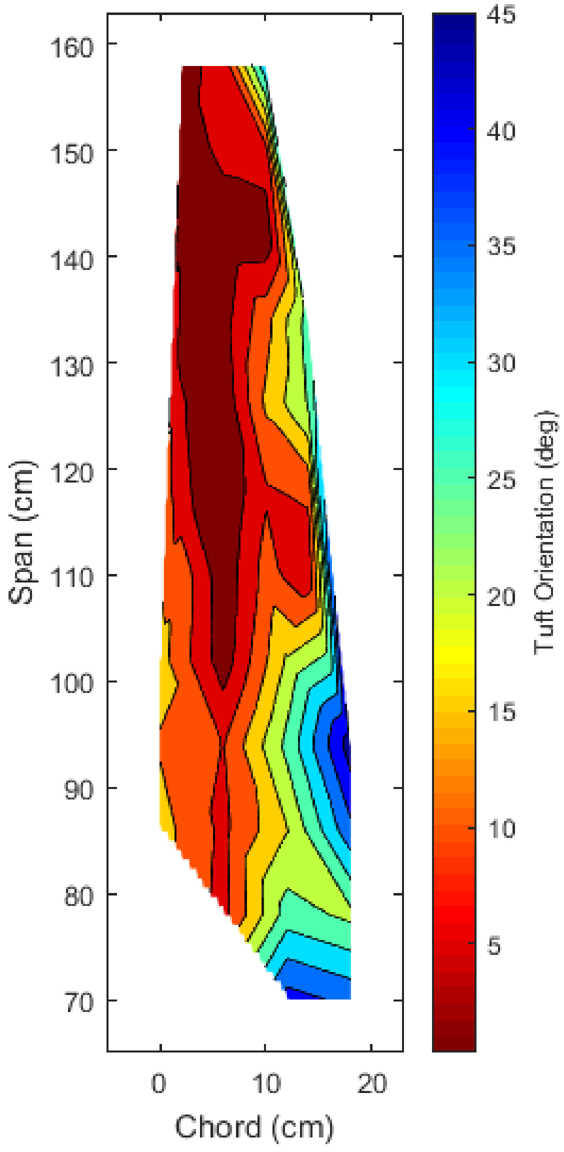

(d) $\psi = 90°$

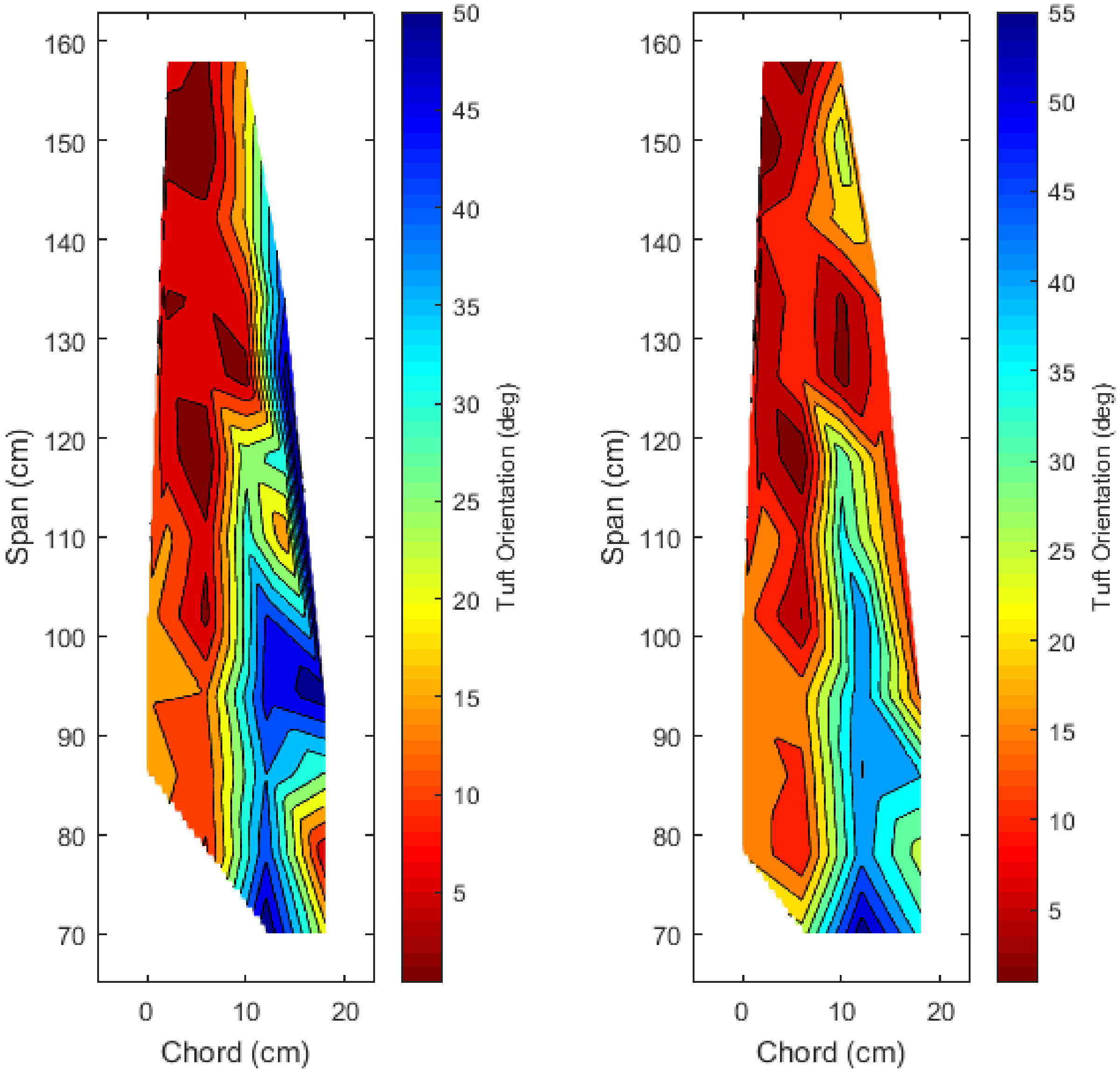

(e) $\psi = 120°$

(f) $\psi = 150°$

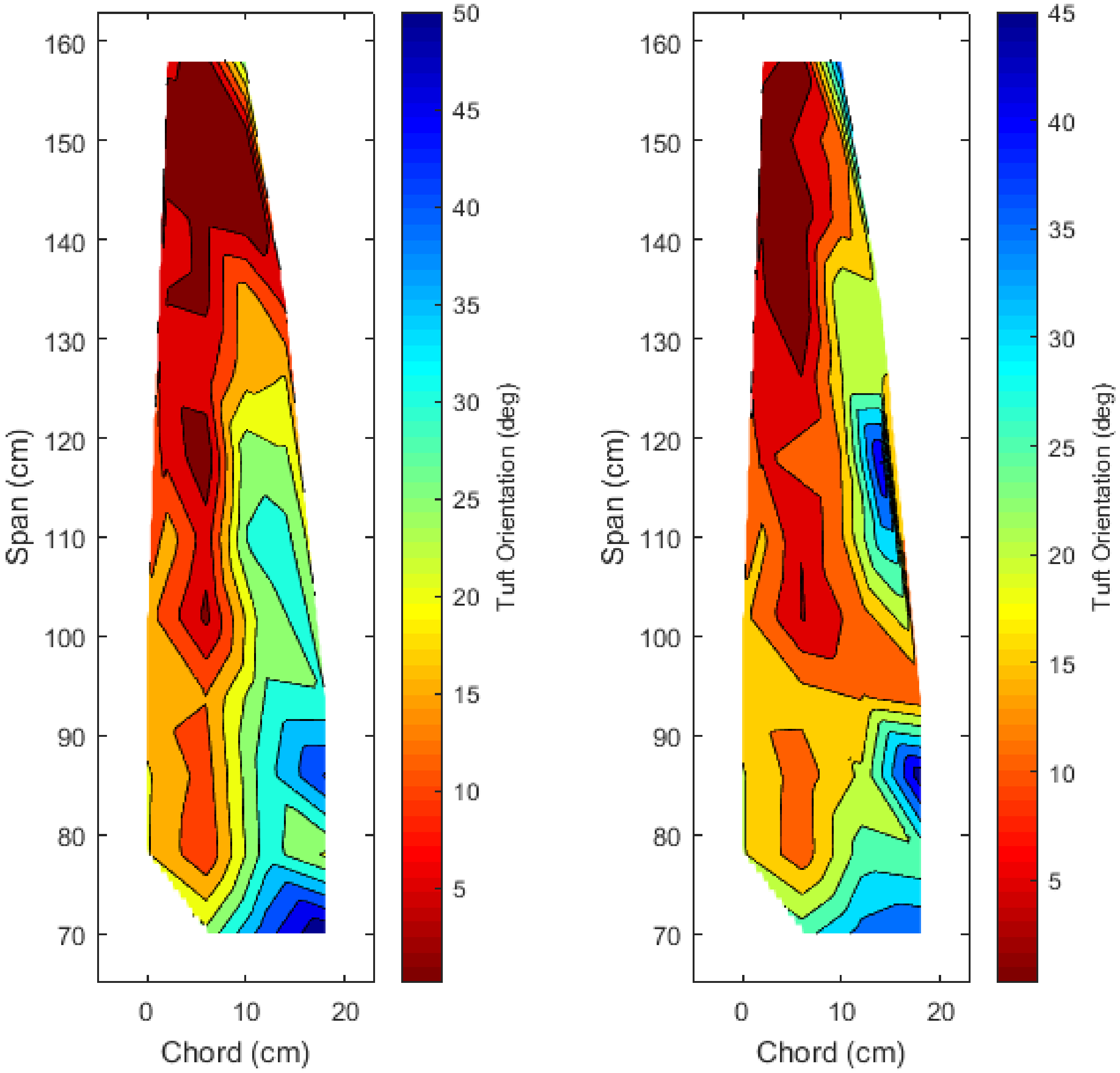

(g) $\psi = 180°$

(h) $\psi = 210°$

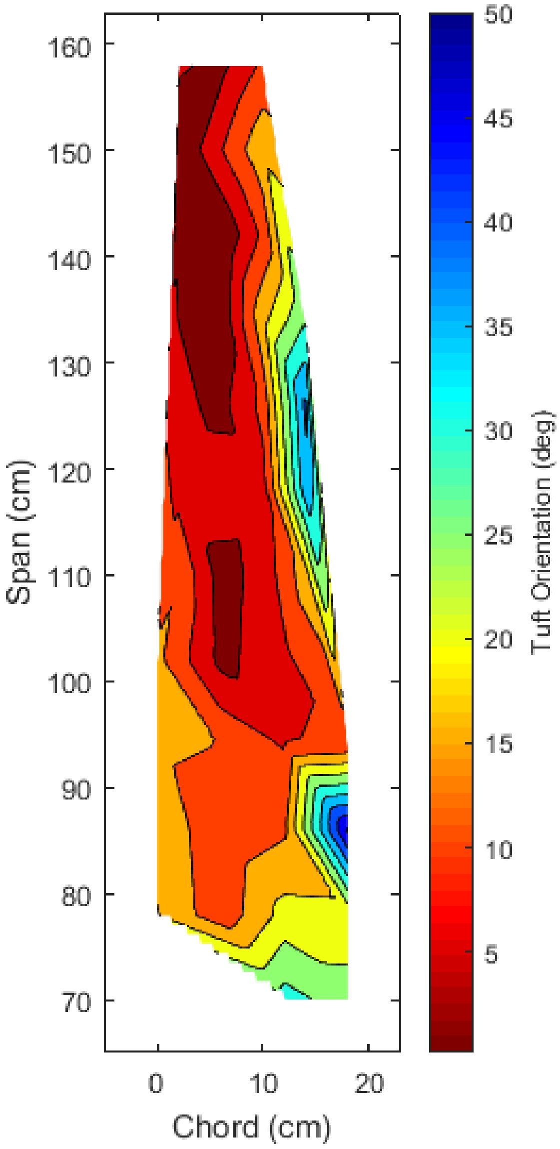

(i) $\psi = 240°$

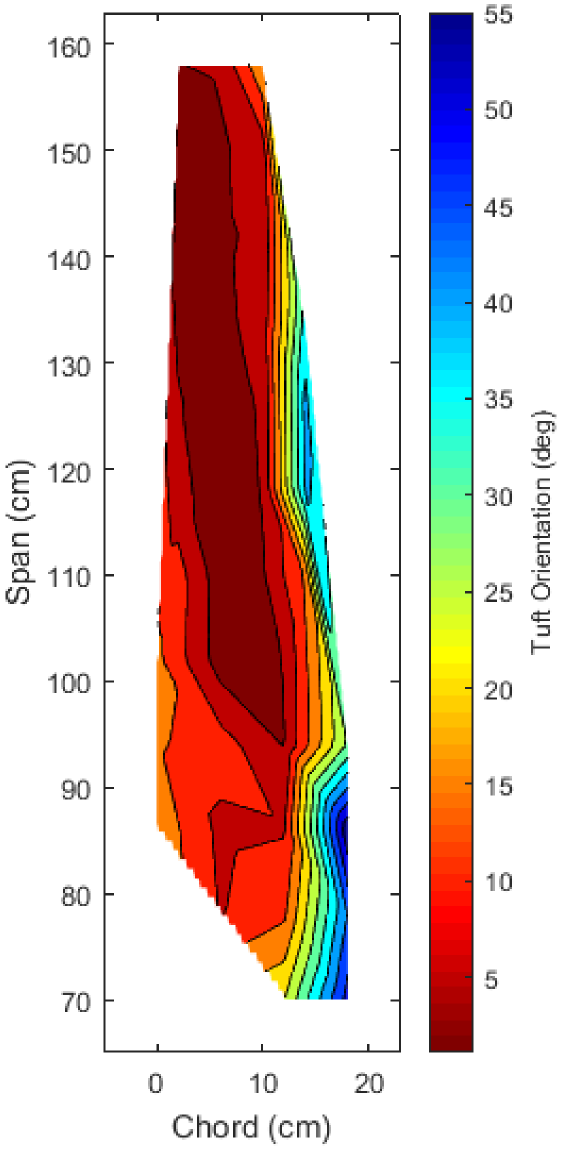

(j) $\psi = 270°$

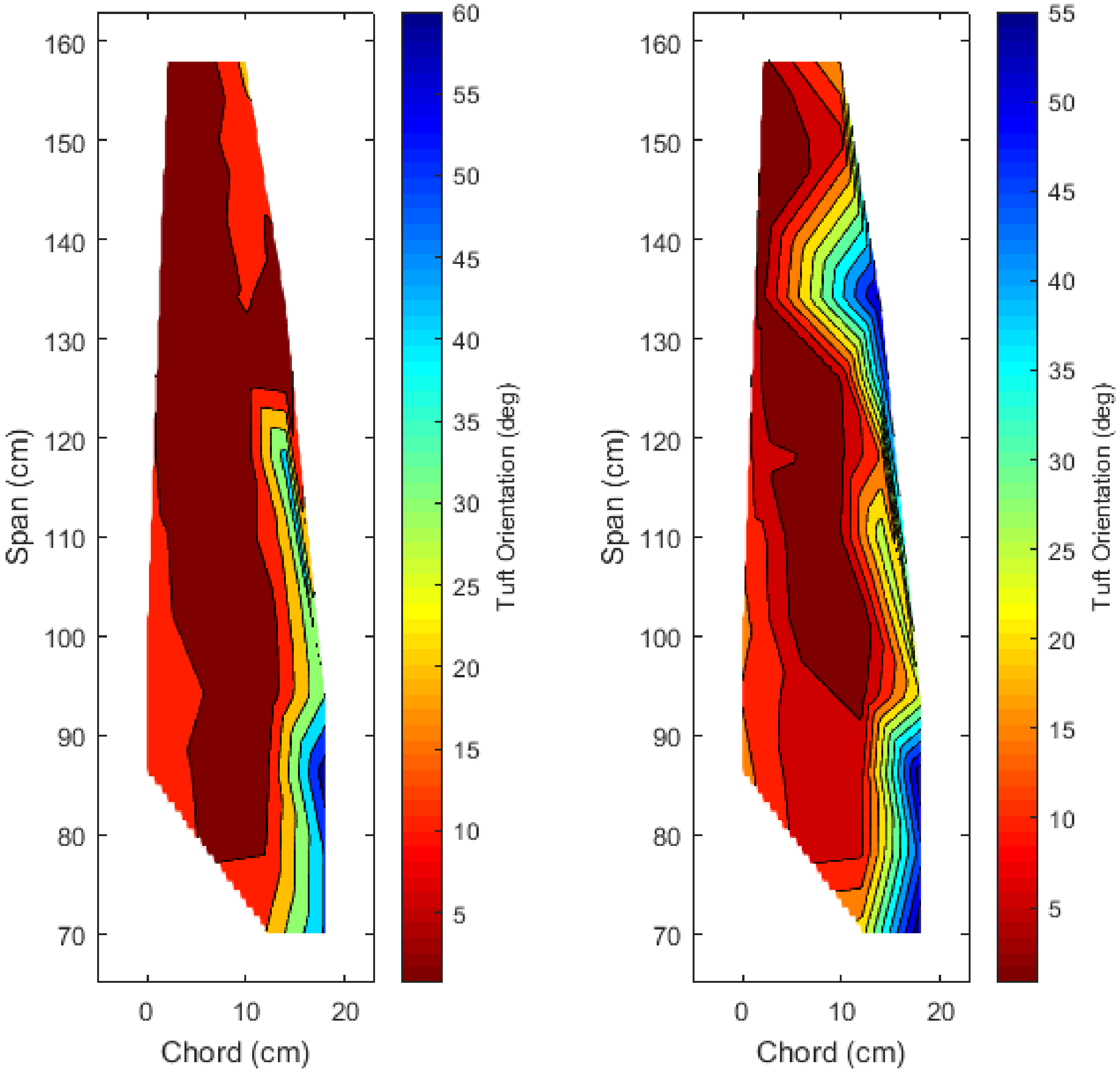

(k) $\psi = 300°$

(l) $\psi = 330°$

Figure H.1: Average Tuft Orientation Maps for $\lambda = 3.2$, $\gamma = \text{-}15°$